# Investigating Per-Flight Criteria for the Application of Idle and Fixed-FPA Descents towards the IAF

## Use Case for Amsterdam Airport Schiphol

L.M.M. Blom

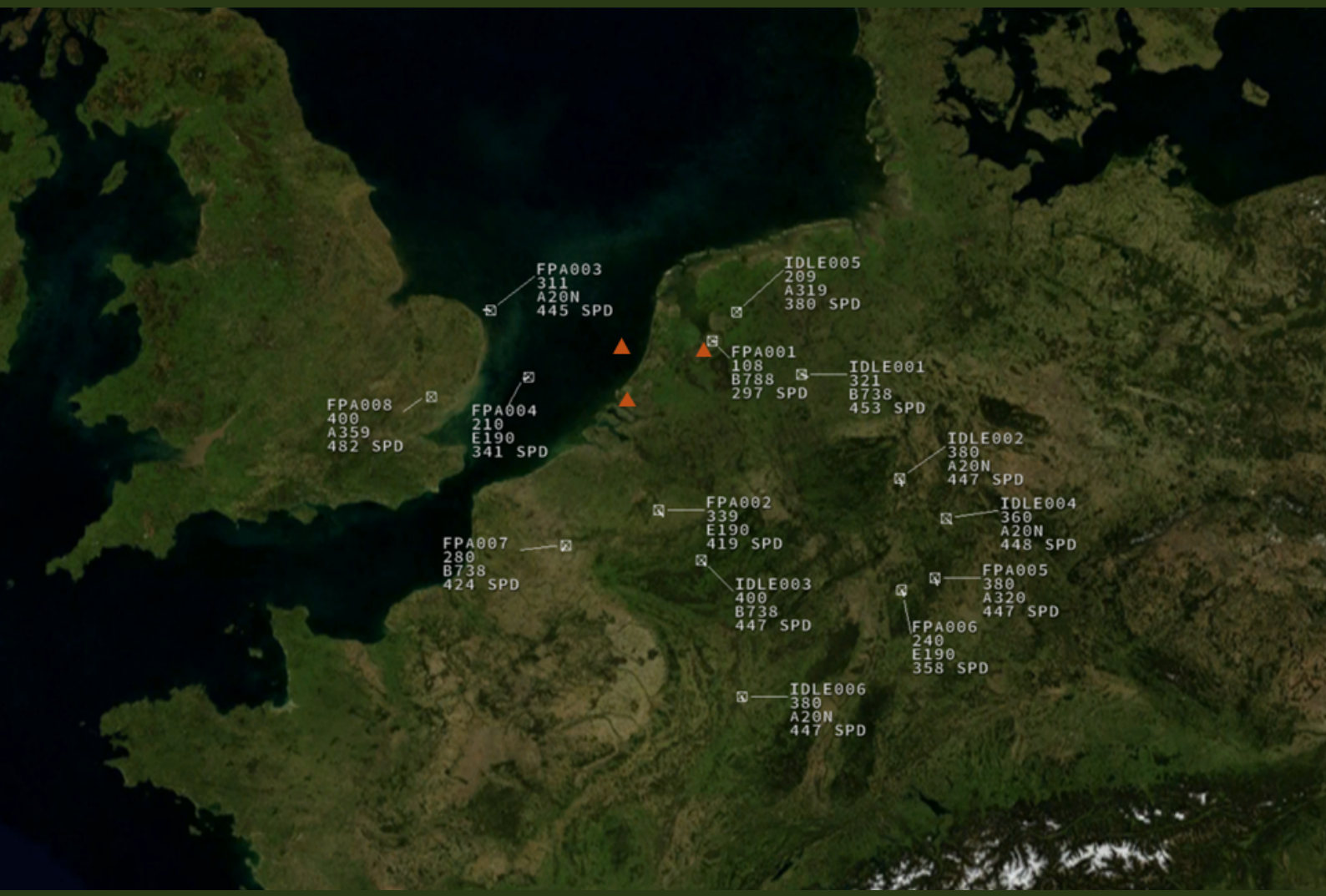


TU Delft
knowledge & development centre
Mainport Schiphol
LVNL

# Investigating Per-Flight Criteria for the Application of Idle and Fixed-FPA Descents towards the IAF

## Use Case for Amsterdam Airport Schiphol

MSc Thesis Report

by

L.M.M. Blom

to obtain the degree of Master of Science at the Delft University of Technology
to be defended publicly on December 8, 2025 at 13:30

| | |
|---|---|
| Student number: | 4996747 |
| Project duration: | March 2025 - December 2025 |
| Place: | Faculty of Aerospace Engineering, Delft |

*Thesis committee*:

| | | |
|---|---|---|
| Chair: | Dr.ir. E. van Kampen | TU Delft |
| Supervisors: | Dr.ir. J. Ellerbroek | TU Delft |
| | Dhr. F. Dijkstra | KDC Mainport Schiphol |
| External examiner: | Dr.ir. M.F.M. Hoogreef | TU Delft |

Cover: Own work, via BlueSky

An electronic version of this thesis is available at `https://repository.tudelft.nl/`.

Faculty of Aerospace Engineering · Delft University of Technology

# Preface

With the completion of this thesis work, my time as a student at TU Delft comes to an end. It has been a challenging yet rewarding journey, through which I have discovered and developed my interest in aviation. During this time, I have met great people with whom I could share my ideas, problems, and achievements. Before I started this thesis work, I completed an internship at LVNL iLabs. I am grateful that my time at LVNL was extended after this internship, allowing me to work on this interesting topic as part of the KDC Centre of Excellence. I am proud of the result and happy to present the work in this thesis report.

I would like to thank the people who have contributed to this work in any way. Firstly, I would like to thank Ferdinand Dijkstra, my supervisor at LVNL, for providing this thesis topic and for guiding me along the way. Your enthusiasm made our brainstorming sessions very enjoyable. I would like to thank Joost Ellerbroek, my supervisor at TU Delft, for providing valuable feedback and for challenging me with new insights. Additionally, I would like to thank my fellow students at LVNL for the interesting discussions and the enjoyable times in the office.

Thank you to my family, for supporting me throughout this journey. Especially to my mother, Desiree, and my sister, Selina, for always showing interest and for motivating me. With you, I could unwind and recharge to take on the challenges that lay ahead. Thank you to my friends, for all the memories we have made over the years and for showing interest in me and my work. Lastly, thank you to my boyfriend, Tim, for supporting me and offering a listening ear whenever needed. Your unique perspective helped me get ideas to solve problems and improve my work.

*Lisa Blom*
*Delft, November 2025*

# Table of Contents

# List of Figures

# List of Tables

# Nomenclature

| | |
|---|---|
| **ACARS** | Aircraft Communications, Addressing and Reporting System |
| **ACC** | Area Control Centre |
| **ADS-B** | Automatic Dependent Surveillance - Broadcast |
| **ADS-C** | Automatic Dependent Surveillance - Contract |
| **ANSP** | Air Navigation Service Provider |
| **APP** | Approach Control |
| **ASI** | Airspeed Indicator |
| **AT** | Along-Track |
| **ATC** | Air Traffic Control |
| **ATCO** | Air Traffic Controller |
| **ATM** | Air Traffic Management |
| **ATS** | Air Traffic Services |
| **BADA** | Base of Aircraft Data |
| **CAS** | Calibrated Airspeed |
| **CD** | Continuous Descent |
| **CDA** | Continuous Descent Approach |
| **CDO** | Continuous Descent Operations |
| **CET** | Central European Time |
| **CI** | Cost Index |
| **COP** | Coordination Point |
| **CPA** | Closest Point of Approach |
| **CPU** | Central Processing Unit |
| **CSV** | Comma-Separated Values |
| **CTA** | Control Area |
| **CTR** | Control Zone |
| **EAS** | Equivalent Airspeed |
| **ECMWF** | European Centre for Medium-Range Weather Forecasts |
| **EHAM** | ICAO code Schiphol Airport |
| **EPP** | Extended Projected Profile |
| **EPS** | Ensemble Prediction System |
| **ETA** | Estimated Time of Arrival |
| **FAF** | Final Approach Fix |
| **FIR** | Flight Information Region |
| **FL** | Flight Level |
| **FMC** | Flight Management Computer |
| **FMS** | Flight Management System |
| **FPA** | Flight Path Angle |
| **GND** | Ground Control |
| **GNSS** | Global Navigation Satellite Systems |
| **GRIB** | Gridded Binary |
| **GS** | Ground Speed |
| **IAF** | Initial Approach Fix |
| **IAS** | Indicated Airspeed |
| **ICAO** | International Civil Aviation Organization |
| **IFR** | Instrument Flight Rules |
| **iLabs** | Innovation Labs |
| **ILS** | Instrument Landing System |
| **ISA** | International Standard Atmosphere |
| **JST** | Japan Standard Time |
| **KCAS** | Calibrated Airspeed in Knots |
| **KNMI** | Koninklijk Nederlands Meteorologisch Instituut (Royal Netherlands Meteorological Institute) |
| **KPI** | Key Performance Indicator |

| | |
|---|---|
| **LoS** | Loss of Separation |
| **LT** | Local Time |
| **LVNL** | Luchtverkeersleiding Nederland (Air Traffic Control The Netherlands) |
| **M** | Mach Number |
| **MCP** | Mode Control Panel |
| **MTCD** | Medium-Term Conflict Detection |
| **MUAC** | Maastricht Upper Area Control Centre |
| **PBN** | Performance-Based Navigation |
| **PC** | Probability of Conflict |
| **PCE** | Polynomial Chaos Expansions |
| **PD** | Profile Descent |
| **PTM** | Probabilistic Transformation Method |
| **PZ** | Protected Zone |
| **RECAT** | Wake Turbulence Re-Categorisation |
| **RMSD** | Root Mean Square Deviation |
| **RMSIE** | Root Mean Square Interpolation Error |
| **RNP** | Required Navigation Performance |
| **RTA** | Required Time of Arrival |
| **RUC** | Rapid Update Cycle |
| **STAR** | Standard Arrival Route |
| **SES** | Single European Sky |
| **SESAR** | Single European Sky ATM Research |
| **SOE** | Speed on Elevator |
| **TAS** | True Airspeed |
| **TBO** | Trajectory-Based Operations |
| **TDWT** | Tailored Descents Wind Tool |
| **TEMO** | Time and Energy Managed Operations |
| **TMA** | Terminal Manoeuvring Area |
| **TOD** | Top of Descent |
| **TP** | Trajectory Predictor |
| **TWR** | Tower |
| **UAC** | Upper Area Control Centre |
| **UTA** | Upper Control Area |
| **V** | Vertical |
| **VNAV** | Vertical Navigation |

# Part A

## Scientific Article

# Investigating Per-Flight Criteria for the Application of Idle and Fixed-FPA Descents towards the IAF

L.M.M. Blom
Supervised by Dr.ir. J. Ellerbroek[1] and Dhr. F. Dijkstra[2]

*Control & Operations, Faculty of Aerospace Engineering*
Delft University of Technology, Delft, The Netherlands

[1]*Faculty of Aerospace Engineering, Delft University of Technology*
[2]*KDC Mainport Schiphol*

**Traffic flows are highly dynamic. Traffic densities vary locally throughout the day, indicating potential for idle descents outside of night hours. Alternatively, fixed-FPA descents can be flown with lower uncertainty. This paper presents the development of novel per-flight criteria for executing idle and fixed-FPA descents from cruise to the Initial Approach Fix (IAF), using associated trajectory uncertainties. The influence of the criteria on the number of successful idle descents is assessed throughout a 24-hour operation. Trajectory uncertainty models were identified from simulations under various wind conditions. Using conflict probabilities, nominal aircraft spacing, and IAF arrival times, descent criteria sets were developed. The number of successful idle descents was evaluated for various reference scenarios with execution restrictions in time frames, developed criteria sets, and trajectory uncertainties. The results show conditional inverse relationships between the trajectory uncertainty, reference scenario, and criteria strictness, and the number of successful idle descents. Scenarios with stricter time restrictions contain fewer successful idle descents. This also holds for stricter criteria, provided that aircraft spacing does not conceal the effect of the different criteria. Similarly, higher trajectory uncertainty reduces the number of successful idle descents, provided that, additionally, the criteria set is not too strict to conceal the effect. At least 50% of the aircraft descending outside of peak hours could complete an idle descent, regardless of scenario, criteria set, and uncertainty set. Including peak hours, this changes to 40% of all descending aircraft. The difference between high and low uncertainty remained below 2% of all flights for all explicitly developed criteria and scenarios. The theoretical maximum is found when all aircraft fly idle descents in the allocated time frames. This is 76% outside peak hours and 68% overall. This research provides a foundation for assigning idle descents and demonstrates their potential by allowing them outside night hours.**

## I. Introduction

The demand for air travel in Europe is increasing rapidly. In the record year 2019, nearly 11 million flights were conducted in European airspace [1]. This number is expected to increase to 16 million flights by 2050. In order to ensure safe and efficient handling of all flights in the future, innovation is required. Over the past years, extensive research has been performed on Trajectory-Based Operations (TBO). The core of the TBO concept revolves around flying a user-preferred, optimal flight path by constructing the 4D trajectory prior to the flight and updating during the flight, and sharing the trajectory information amongst all stakeholders [2]. This concept enables a greater use of Continuous Descent Operations (CDO). By using CDO, an aircraft can execute a continuous descent profile optimised to the operational capability of the aircraft, with low-thrust settings [3]. Various studies have demonstrated that continuous descents show a reduction in fuel consumption, emissions, and noise compared to conventional step-down descents with level segments [4–7].

In order to minimise fuel consumption, emissions, and noise, a continuous descent is ideally flown with idle thrust [8]. However, an idle descent comes with increased uncertainty as the vertical profile of an idle descent is highly sensitive to the descent speed profile, wind conditions, and aircraft weight. An alternative continuous descent follows a constant geometric flight path angle (FPA). This fixed-FPA descent has higher predictability and thus lower uncertainty compared to an idle descent [6, 8]. The feasibility of flying idle and fixed-FPA descents has been demonstrated [9–14]. However, CDOs are currently restricted to low traffic densities due to low predictability [14]. At Amsterdam Airport Schiphol, this is limited to nighttime operations only [15]. In reality, traffic densities vary throughout the day, meaning that low traffic densities can occur locally. Therefore, potential lies in investigating when idle descents can be flown throughout a 24-hour operation. No clear criteria, based on accurate trajectory uncertainty modelling, have been developed for when these descents can be executed safely throughout the day. This research gap will be addressed in this paper.

The main contribution of this paper is to develop criteria for the execution of idle and fixed-FPA descents from cruise to the Initial Approach Fix (IAF) on a per-flight basis throughout a 24-hour operation, taking into account the associated trajectory uncertainties, and assessing the influence on the number of successful idle descents. This will be done by means of descent simulations. The simulated descents will be flown towards Schiphol Airport using existing Standard Arrival Routes (STARs). The IAFs for Schiphol Airport are the waypoints ARTIP, RIVER, and SUGOL. Within the 24-hour operation, several scenarios with different execution restrictions in time frames are considered. The trajectory uncertainties associated with idle and fixed-FPA descents and the sensitivity of the developed criteria to trajectory uncertainty under the various restriction scenarios will be investigated. Throughout the 24-hour operation, only idle and fixed-FPA descents are flown. The criteria will explicitly assign idle or fixed-FPA descents to each aircraft. The resulting number of successful idle descents is of interest, as idle descents are the most environmentally friendly descents.

Although Schiphol Airport will be used for this research, the aim is to develop general criteria for the application of idle and fixed-FPA descents, allowing the findings to be extrapolated to other airports and airspaces. A clear overview of when idle descents can be applied throughout a 24-hour operation has the potential to accelerate the implementation of idle descents in the daily operation. Executing idle descents in higher traffic densities enables the possibility of further reducing noise, emissions, and fuel burn. Furthermore, a quantification of the sensitivity of the implementation of these continuous descents to trajectory uncertainties potentially provides a new perspective on the discussion regarding uplinking and downlinking data to and from the aircraft, such as uplinking weather information and downlinking aircraft mass via ATS B2 ADS-C EPP data.

This paper is structured as follows. In section II, background information on trajectory uncertainty, idle descents, and fixed-FPA descents is provided. The preliminary research concerning trajectory uncertainty is presented in section III. The main experiment design is described in section IV. The experimental setup is discussed in section V. The results are presented in section VI and discussed in section VII. Conclusions are drawn in section VIII.

## II. Background

This section contains background information relevant to the methodology of the research. Detailed information is provided on trajectory uncertainty, idle descents, and fixed-FPA descents.

### A. Trajectory Uncertainty

It is essential to consider the trajectory uncertainties associated with idle and fixed-FPA descents when developing descent application criteria. Accurately modelled trajectory uncertainty makes the simulation results more reliable. Therefore, several aspects regarding trajectory uncertainty that are relevant for this application are discussed first.

*1. Sources of Trajectory Uncertainty*

Trajectory uncertainty is characterised by various different factors that influence the accuracy of a trajectory prediction. Over the years, numerous studies investigating the sources of trajectory uncertainty have been conducted [16–21]. Their results provide a clear overview of the sources of trajectory uncertainty, and their effects.

*Initial Aircraft State*

Every trajectory prediction starts with a set of initial aircraft states. These states include the aircraft position, heading, speed, vertical rate, and mass [18, 21]. Research has shown that deviations in aircraft mass from the expected greatly influence the uncertainty of the vertical profile of a trajectory, where deviations in speed profiles from the expected or planned mainly affect the duration of flight and the rate of descent [17, 18]. Deviations in the assumed state values from the actual state values will propagate throughout the predicted trajectory [19]. Therefore, the accuracy of trajectory prediction is highly dependent on the accuracy of the initial aircraft state data. ATS B2 ADS-C is a new datalink technology and is expected to be readily available in the future. The EPP profile contains data regarding the aircraft gross mass. By using ATS B2 ADS-C EPP data, the accuracy of trajectory predictors can be improved significantly [22]. Knowing the aircraft mass practically eliminates the mass uncertainty.

*Modelling*

The accuracy of the mathematical representation compared to the real aircraft behaviour directly influences the trajectory prediction [19]. Common simplifications for the mathematical model are the small-angle approximation and the point mass approximation, considering only the centre of gravity of the aircraft [18]. The errors induced by aircraft motion modelling are considered to have a negligible effect on trajectory uncertainty.

The aircraft performance models are used for the calculations on aircraft performance, such as thrust, drag, and fuel consumption for various flight conditions [19]. The parameters for these models are usually generalised. The Base of Aircraft Data (BADA) is commonly used for this. Models from BADA are highly accurate, meaning that the trajectory uncertainties introduced by errors in aircraft performance modelling are small for ATM applications [18]. However, this is difficult to prove, but a necessary assumption for this research, to contain the scope.

Using an Earth Model such as the WGS84 model or a spherical Earth representation leads to trajectory uncertainty. However, errors in the Earth model are second order and therefore negligible for ATM applications [18].

*Aircraft Intent*

Aircraft intent represents the commanded instructions and executed control actions as a result of ATC procedures, pilot procedures, and the flight plan [18, 19]. The uncertainty arises when the aircraft intent is (partially) unknown to the trajectory predictor. This uncertainty represents how the aircraft is actually operated compared to the original flight plan used for the trajectory prediction. This uncertainty can be caused by various factors [20]. These include vectoring, ATC clearance for the TOD location, instructed level-offs, and speed intent. ATS B2

ADS-C data allows controllers to have a clearer picture of aircraft intent and airspace sector loads [23]. With this, the trajectory prediction can be updated, leading to smaller uncertainties.

*Flight Control Inaccuracy*

Uncertainty due to flight control inaccuracy is known as a flight technical error. This error describes the inability of an aircraft to stay on its specified track due to the performance of the FMS and the flight control systems. Arguments have been made stating that the long-term effect of flight technical errors on trajectory accuracy is negligible compared to other uncertainty sources [19].

*Weather*

Atmospheric temperature and pressure influence trajectory uncertainty to some extent. Temperature errors lead to errors in speed due to speed conversions between Mach, indicated airspeed (IAS), and true airspeed (TAS). However, the effect of temperature error on trajectory uncertainty has been found to be marginal [18]. On the contrary, wind uncertainty is overall one of the biggest contributors to trajectory uncertainty, especially influencing the horizontal error [17, 24]. Wind directly influences the ground speed (GS) of the aircraft, and is taken into account by the FMS for constructing the descent path. The wind profile prediction error can be split up into three components [25]. The first component is the prediction error in the base forecast data, defining the difference between the weather forecast and the actual weather. The second component is the error due to selecting forecast grid cells that are not on the planned trajectory. In [25] it is mentioned that the wind forecast available to the FMS is taken as the wind profile of a stationary location, meaning it is likely not representative for an entire descent. This error can be reduced by updating the meteorological information in the FMS during flight execution, using uplink to the aircraft [26]. The last error component is due to interpolation by the FMS between the available levels.

In the literature, an approach for quantifying wind uncertainty is presented. This approach uses time-lagged ensembles of weather forecasts for a specific time to determine the wind uncertainty [19, 27–29]. The forecast error is measured as the difference with the 0-hour forecast. Wind forecast uncertainty is defined as the standard deviation of the ensemble members, where each member is an $x$-hour forecast for a specific time. By using many forecasts, where each forecast has the same number of ensemble members, probability density functions of the wind can be constructed, as done in [29]. Having multiple ensemble members at the same time stamp will lead to better wind uncertainty modelling than having to use $x$-hour forecasts as ensemble members. However, it is the only feasible option if only one forecast is provided per time stamp for a specific forecast time.

A drawback of this approach is that the correlation between ensemble members is generally larger than for other techniques [27]. However, a key advantage is that with this approach, regional variations in uncertainty, that are related to weather phenomena, can be identified. In addition, only the obtained $x$-hour forecasts from e.g. the KNMI are needed, making this method less computationally intensive than methods that require additional forecast models.

When quantifying trajectory uncertainty, it is important to consider the influence of wind error correlation. Various studies have researched this [24, 30–32]. It was found that simplifying assumptions regarding the wind field correlation influences trajectory uncertainty. This is especially relevant for the probability of conflict between two aircraft, as correlation effects are stronger for aircraft in closer proximity to each other. By neglecting wind correlation, the conflict probability is overestimated [24]. Therefore, neglecting it is a conservative assumption. This assumption allows for a first conservative approximation.

### 2. Trajectory Uncertainty Quantification

The track error forms the basis of quantifying trajectory uncertainty. It describes the difference between the desired track position and the actual position. Track error can be expressed as a temporal error and as a spatial error. The temporal error is defined as the time difference between the predicted and actual time the aircraft is at a particular position along the course. This metric is commonly used to determine the status of a flight: premature, delayed, or on time. The spatial error is the result of a combined horizontal and vertical error. The horizontal error is defined as the great-circle distance between the predicted and the actual position of an aircraft at time $t$. It can be decomposed into along-track and cross-track error components. The along-track error is the component of the horizontal error that is projected onto the actual course of the aircraft. The cross-track error is projected perpendicular to the actual course. With this decomposition, it can be shown that the along-track error is associated with the temporal error, whereas the cross-track error is not. In fact, the along-track error is the spatial representation of the temporal error. When a flight is on time, the along-track error is zero. The vertical error is the altitude difference between the predicted and actual aircraft position.

Trajectory uncertainty can be quantified using various techniques. In general, position uncertainty at time $t$ can be visualised as a 3D ellipsoid around the projected aircraft position on the predicted reference trajectory. This covariance ellipsoid represents the probability distributions of the along-track, cross-track, and vertical errors compared to the reference trajectory. This is illustrated in Figure 1. The subsequent ellipsoids at each time $t$ form a tube that represents the possible aircraft positions throughout the trajectory [17].

The positional probability distributions can be constructed using parametric estimations. The error components are then described by zero-mean Gaussian random variables, for which the standard deviation increases with time [33]. This approach is suitable for online applications because of the low computational load. It can therefore be used in a simulation of a representative traffic scenario to determine the worst-case distances to other aircraft.

Additionally, Monte Carlo simulations are used to investigate the effects of changes in uncertain inputs on the trajectory uncertainty, by means of simulating the trajectory. The inputs are treated as random variables, such that different combinations are used in each simulation. The Monte Carlo approach is commonly used to quantify trajectory uncertainties [17–19, 34, 35].

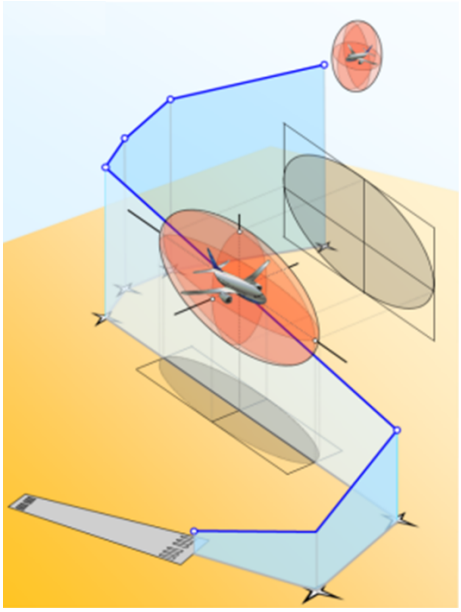

**Figure 1 Trajectory uncertainty expressed as 3D ellipsoid (adapted from [19]).**

From the observed trajectory uncertainties based on varying uncertain inputs, relationships can be derived that describe the uncertainty in a parametric estimation. Essentially, the simulation outputs can be used to find parameter values for a parametric uncertainty estimation. This way, the results of Monte Carlo simulations can be converted to online applications by using them in parametric estimations. Conducting the simulations requires a high computational load, especially since many simulations are required to obtain statistically reliable results.

### *3. Conflict Detection with Trajectory Uncertainty*

The lookahead time for conflict detection considered in this research is approximately 20 minutes, meaning that mid-range conflict detection models are most appropriate. It is important that conflict probabilities can be calculated in real-time. Since trajectory uncertainty changes over time, the conflict probability also changes. An established mid-range conflict prediction model using parametric estimations, which is appropriate for this application [33], will be explained below. This model is developed for level-flight conditions, meaning it is at least appropriate for cruise segments. In this research, the applicability of this model to descents will be investigated. Subsequently, the model will be adjusted if needed.

In the model, trajectory uncertainty is modelled as the variance of the along-track error as a function of time and as the variance of the cross-track error as a function of time. The along-track variance grows quadratically with time, while the cross-track error grows quadratically with distance, which is a function of time. The cross-track variance saturates at a fixed value. That is because corrections for the cross-track error are done in the short term, either by the pilots or the FMS, which has a saturation point. Meanwhile, along-track errors are dealt with in the long term, usually by speed instructions from ATC. The model proposed in [33] can be extended by accounting for vertical error as well. Initially, it is assumed that the vertical error variance grows linearly with time during climb or descent, and returns to zero when a set altitude is reached because the FMS is very capable of holding altitude. This assumption will be verified in this research and adjusted if needed.

$$\begin{aligned} \sigma_a^2(t) &\sim r_a^2 t^2 \\ \sigma_c^2(t) &\sim \min\{r_c^2 s^2(t), \bar{\sigma}_c^2\} \\ \sigma_v^2 &\sim r_v t \end{aligned} \tag{1}$$

Here, $r_a$, $r_c$, and $r_v$ are the error growth rates for the along-track, cross-track, and vertical errors, respectively. These can be determined from (Monte Carlo) simulations that include trajectory uncertainties, or from literature [18], depending on the desired accuracy.

An aircraft trajectory $\vec{x}(t)$ is assumed to be normally distributed, with as mean the predicted nominal trajectory $\vec{p}(t)$ and as variance the covariance matrix composed from the track variances and corrected for aircraft heading $\theta$ using a rotation matrix:

$$\begin{aligned} \vec{x}(t) &\sim \mathcal{N}(\vec{p}(t), V(t)) \\ V(t) &= R(\theta)\bar{V}(t)R(\theta)^T \\ \bar{V}(t) &= \begin{bmatrix} \sigma_a^2 & 0 & 0 \\ 0 & \sigma_c^2 & 0 \\ 0 & 0 & \sigma_v^2 \end{bmatrix} \\ R(\theta) &= \begin{bmatrix} \cos\theta & -\sin\theta & 0 \\ \sin\theta & \cos\theta & 0 \\ 0 & 0 & 1 \end{bmatrix} \end{aligned} \tag{2}$$

Next, it is assumed that the trajectories of aircraft A and B are uncorrelated. The distance between the two aircraft, $\vec{d}(t)$, can then also be modelled as a Gaussian random variable. The mean is the distance function between the two nominal trajectories. The variance is the addition of the separate covariance matrices for aircraft A and B:

$$\begin{aligned} \vec{d}(t) &\sim \mathcal{N}(\vec{\mu}(t), Q(t)) \\ \vec{\mu}(t) &= \vec{p}_A(t) - \vec{p}_B(t) \\ Q(t) &= V_A(t) + V_B(t) \end{aligned} \tag{3}$$

The resulting 3D multivariate probability density function, $\vec{p}_{\vec{d}_t}$, represents the uncertainty ellipsoid of the distance between two aircraft. The overlap between this ellipsoid and the Protected Zone (PZ) is the probability of conflict $PC$. This overlap can be found by integrating $\vec{p}_{\vec{d}_t}$ over the PZ:

$$PC(t) = \int_{y \in PZ} \vec{p}_{\vec{d}_t}(y)\, dy \tag{4}$$

The PZ is a cylinder, with a predefined height of 2000 ft and a horizontal radius of 5 nm. This ensures that the separation minima of 1000 ft vertical and 5 nm horizontal apply from all sides.

$PC(t)$ is calculated for every time step until the lookahead time $T$. The maximum value of conflict probability is straightforwardly:

$$C(\gamma) = \max_{t\in[0,T]} PC(t) \tag{5}$$

Here, $\gamma$ represents the current step in time. Every new time step, new conflict probabilities are calculated until the lookahead time. When the maximum conflict probability $C(\gamma)$ is higher than a predefined threshold $\bar{C}$, a conflict is declared.

In Figure 2, the horizontal ellipse overlap of the joint uncertainty ellipsoid is shown on the left. This ellipse represents the joint uncertainty of the horizontal components of $\vec{d}(t)$, as explained above. On the right side, the vertical ellipse overlap of the joint uncertainty ellipsoid is illustrated.

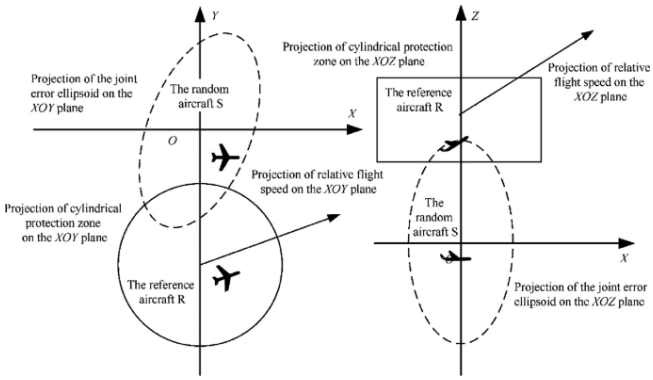


**Figure 2 Joint trajectory uncertainty overlap with the protective zone [36].**

### B. Idle Descents

In an idle descent, the throttle is set to the idle position. This is the lowest power setting possible without shutting down the engines. A small amount of thrust is still produced. During the idle descent, a constant Mach is maintained until the crossover altitude. From this point onward, a constant calibrated airspeed (CAS) is maintained. This is stopped only at a speed change point, such as the IAF, or when ATC instructs a new speed. In Figure 3, a schematic overview of the vertical profile of an idle descent is provided. It shows that constant Mach and later constant CAS are maintained until deceleration is required to adhere to the speed constraint at the IAF.

The idle descent is very efficient in terms of fuel usage, noise, and emissions, but comes with increased uncertainty, thereby needing greater spacing [8]. The vertical profile of an idle descent is highly sensitive to the descent speed profile, wind, and aircraft mass. The descent path becomes shallower with a decrease in descent speed, an increase in tailwind, or an increase in aircraft weight. Typically, large separation buffers are applied by ATC to ensure adequate spacing from an aircraft performing an idle descent. Due to the rapidly increasing uncertainty in an idle descent, level segments are often imposed by ATC to reduce the vertical uncertainty back to zero, usually for conflict resolution purposes.

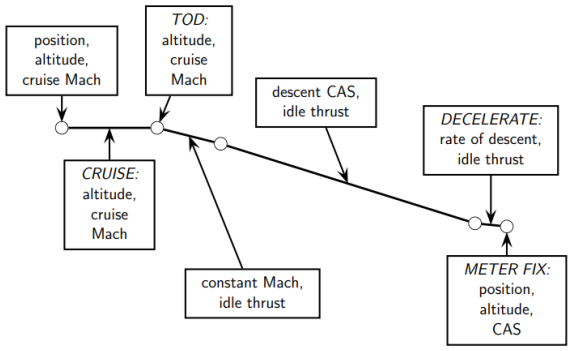


**Figure 3 Schematic overview of an idle descent [9].**

In 2006, a trial was conducted where aircraft flew CDAs from cruise until the final approach at Schiphol Airport, during night-time operations [10]. An idle descent path was flown to the first vertical constraint. This constraint was beyond the TMA boundary and thus beyond the IAF, meaning that idle descents were flown from cruise till at least the IAF. The test was conducted in low traffic densities only, to ensure safe circumstances and sufficient spacing. Optimal CDAs flown during the trial used minimal altitude stabilisation, minimal thrust increase from idle, and no excessive use of speed brakes. The findings of this test support the statement in section II.A.1 that accurate wind information should improve trajectory predictability and thus reduce trajectory uncertainty. Therefore, CDAs should include uplinking weather forecasts prior to TOD. Most aircraft have the ability to receive uplinks.

Even though the vertical profile of an idle descent is highly sensitive to the descent speed profile, wind, and aircraft mass, a large portion of the idle descent is flown with a near-constant FPA until the deceleration segment is started. The magnitude of this FPA depends on aircraft characteristics (including mass), descent speed, and wind conditions. Therefore, a fixed-FPA descent is a logical alternative for the idle descent when seeking to increase trajectory predictability while slightly increasing thrust usage.

### C. Fixed-FPA Descents

In a fixed-FPA descent, the aircraft follows a predefined, constant geometric FPA ($\gamma_g$). A great advantage of this descent type is that the vertical profile of the aircraft is explicitly defined. Because of this, fixed-FPA descents have an increased predictability and thus decreased uncertainty compared to idle descents [6, 8]. Therefore, fixed-FPA descents are more suitable in higher traffic densities. However, in order to adhere to the fixed $\gamma_g$, non-idle thrust is required. Instead of a constant $\gamma_g$ throughout the entire descent, the descent can be split into segments. In each segment, a different $\gamma_g$ can be used. Using this can make a descent more efficient, as the optimal $\gamma_g$ varies with altitude.

In a fixed-FPA descent, a constant Mach is maintained until the crossover altitude. Then, a constant CAS is maintained for each segment, similar to an idle descent. Also, a decelera-

tion segment before the IAF is introduced to adhere to the speed restrictions there [6, 8]. During a deceleration segment, it is possible to fly either at the fixed-FPA, which is typically done, or at different angles to complete the deceleration as quickly as possible. The thrust required is calculated based on the predefined $\gamma_g$ and CAS, and on the other aircraft- and weather-specific variables. In Figure 4, a schematic overview of a fixed-FPA descent is provided.

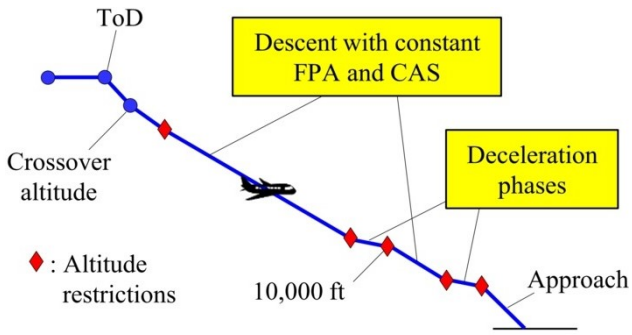


**Figure 4 Schematic overview of a fixed-FPA descent (adapted from [13]).**

Various aircraft types contain an autopilot mode through which a fixed-FPA descent can be flown [15]. The pilot can select the desired $\gamma_g$ using a knob on the Mode Control Panel (MCP). This FPA mode is available on the A320, A330, A340, and A380 Airbus types. For Boeing aircraft, this mode has been introduced on the B777, B787, and B747-800. If no specific FPA mode is available, a fixed-FPA descent is generally flown in the VNAV PATH autopilot mode [37]. Alternatively, the pilot can manually create a waypoint after the TOD, and input an altitude for all necessary waypoints along the route in the FMC [11, 37]. By adhering to these altitude constraints, the desired FPA is flown.

Although the fixed-FPA descent profile is independent of wind conditions, accurate wind information remains important for determining ground speeds and subsequently calculating arrival times at waypoints. Because of this, consistency between wind information available on the ground and wind information loaded into the FMS is desired [6].

A flight test at Louisville International Airport in 2002 confirmed noise reduction and fuel saving compared to a conventional step-down approach [5]. In addition, it was confirmed that accurate trajectory predictions are needed when this descent is to be implemented in high-density traffic, as it requires a different spacing strategy from ATC. In [11], the importance of accurate wind estimations to achieve more accurate time spacing is underlined.

In recent years, various flight tests and simulator tests have shown that the fixed-FPA descent trajectory can be predicted with great accuracy [37], and that the fixed-FPA descent is feasible for wide-body aircraft using the current FMS and pilot intervention, for angles under 2.5° [11–13]. The fixed-FPA descent has the capabilities required for procedure integration into congested airspace. The combination of a fixed-FPA descent with speed control has the potential to result in significant improvements in fuel and time management efficiency in future operations, compared to conventional arrival operations.

In [7], it was demonstrated that the 3° fixed-FPA descent generally has considerably less fuel usage and increased time saving compared to conventional descents. In [38], the highest fuel saving relative to a 1°-FPA was found to be 14.0% (191 kg) for an FPA of 2.5°. Furthermore, [13] demonstrated that the fixed-FPA descent could potentially reduce the fuel consumption in congested airspace compared to the idle descent. This is the case especially when arrival time delays of more than approximately 120 s are present.

In December 2022 and February 2023, for the first time ever, the fixed-FPA descent was demonstrated on scheduled commercial flights with A320neo and A320ceo aircraft to Kansai International Airport [14]. The aim of this demonstration was to expand the time frame for a possible implementation of CDO in Japan. Idle descents are currently limited to three airports in Japan, for scheduled arrival times between 23:00 and 07:00 JST (Japan Standard Time). The flight test showed that, compared to conventional step-down descents, the reduction in fuel consumption for the 2.5°-FPA descent was 9%, while it was 6.7% for the 2.0°-FPA descent. Because of increased predictability, the CDO implementation window can be extended by allowing fixed-FPA descents outside the current CDO hours.

## III. Preliminary Research

The aim of this research is to develop criteria for the application of idle and fixed-FPA descents and analyse the resulting numbers of successfully flown idle descents. This is done by evaluating the conflict probabilities between aircraft involving idle descents in various traffic scenarios. At the core of this lies a realistic trajectory uncertainty model, with which conflict probabilities can be calculated. Therefore, the preliminary research focuses on identifying trajectory uncertainty model parameters. The methodology and resulting models are presented in this section.

### A. General Outline

The trajectory uncertainty model parameters are identified through simulation. With the simulations, trajectory uncertainty solely due to wind prediction error is quantified, as wind uncertainty is generally found to be the biggest contributor to trajectory uncertainty. The trajectory uncertainty model from [33], discussed in section II.A.3, serves as the base model for this, but is adjusted based on the simulation findings.

The simulations for the trajectory uncertainty parameters are conducted for three reasons. Firstly, the uncertainty model in [33] is developed using level flight. These simulations can verify this model for cruise segments. Secondly, an uncertainty model for descent is obtained from the simulations. It can be compared to the cruise model to see the applicability of the model in [33] to descents. Lastly, the simulations enable the determination of trajectory uncertainty parameters that indicate the order of magnitude applicable to idle and fixed-FPA descents.

### B. Assumptions

The trajectory uncertainty models and simulations are set up using several assumptions. These assumptions are listed and explained below.

- Model errors caused by the accuracy of aircraft performance models, the spherical Earth assumption, equations of motion simplifications, and numerical methods are not significant enough to be incorporated in trajectory uncertainties, as shown in [18].
- Variation in aircraft mass is decreased by the capability of receiving ATS B2 ADS-C EPP data, making mass uncertainties irrelevant for trajectory uncertainty [22]. Even though currently ATS B2 ADS-C data is not readily available, this assumption is valid as this research focuses on continuous descent implementations aimed for the future.
- The aircraft intent is clear, so possible errors originating from pilot actions or wrong FMS settings are neglected.
- The FMS has knowledge of the high-resolution wind field grid. Usually, the FMS has knowledge of a few altitude layers. Since only wind prediction error is investigated in this research, it is outside the scope of the research to accurately model those layers. Furthermore, the importance of accurate wind information available to the FMS can be underlined in this way.
- The FMS is assumed to be capable of obtaining very high lateral precision in the flight path due to the current RNP capabilities, as stated in [10]. Therefore, cross-track errors are neglected when modelling trajectory uncertainty. Trajectory uncertainty will be expressed in the along-track and vertical error.
- It is assumed that IAS is equal to CAS. At higher airspeeds and altitudes, IAS and CAS are approximately the same, making this assumption valid.

### C. Simulation Platform

All simulations run for the research presented in this paper are done using BlueSky. BlueSky is a widely used, open-source air traffic simulator, developed at TU Delft. It is written in Python, making it highly suitable for further development. The simulator has a user interface consisting of a main radar screen and a command line, in which user commands can be entered. These commands include simulation commands, sim-operating commands, or aircraft-specific commands. In addition, a BlueSky simulation can be run without the user interface. In "sim-detached" mode, BlueSky can be called directly into a Python script and run in the background. Usually, a simulation is run by calling a scenario file. This file contains information and commands for all aircraft in the simulation. All commands in BlueSky are added to the "stack" and carried out from there. This way, commands can originate from different sources and are all carried out in the correct order. Furthermore, it is possible to run sped-up simulations. The simulation speed can range up to 60x faster than real-time, depending on the CPU usage and computer performance. As BlueSky is open-source, it is being developed by multiple developers and users in parallel, leading to the existence of (slightly) different versions. The specific version of BlueSky used for this research is the version developed at LVNL iLabs. This BlueSky version has improved aircraft performance models, improved autopilot performance, and extra functionalities to increase the resemblance of the interface with actual ATCO working stations. Its default descent mode is a performance descent, which is an idle descent based on the BADA performance model. Due to its extensive functionality and performance models, BlueSky is highly suitable for this research.

### D. Preparations

While BlueSky has many capabilities, it needed some modifications to fulfil the needs of this research. As preparatory work, some features were added to BlueSky. Geometric descent functionality has been implemented in the BlueSky autopilot. Via a stack command, a geometric descent with a pre-specified fixed FPA can be assigned to an aircraft prior to TOD. A geometric path with the fixed FPA is then constructed by placing corresponding altitude constraints at each waypoint along the route. The autopilot adheres to the resulting fixed geometric path using a vertical speed controller with a feed-forward term and P-gain.

Additionally, wind conditions were implemented. Ground speed is updated based on the wind conditions the aircraft encounters. The autopilot uses the wind conditions to construct the descent path and determine the TOD. Furthermore, a plugin was written that allows wind fields from either GRIB files (explained in detail later) or CSV files to be loaded into BlueSky as a wind field. The wind field grids provided in these files are translated into the wind field grid structure present in BlueSky.

### E. Obtaining Trajectory Uncertainty Model Parameters

With BlueSky fully prepared for simulations, the trajectory uncertainty model parameters can be obtained. As stated earlier, the effect of wind prediction error on trajectory uncertainty is investigated through simulation. Other factors, such as not knowing the geometric descent angles of an idle descent, are not taken into account. Because of this, the parameter values found serve as lower bounds for the trajectory uncertainty parameter range to be used for the sensitivity analysis regarding the application criteria.

#### *1. Wind Data Processing*

The weather forecast for the Dutch FIR is provided by the Royal Netherlands Meteorological Institute, which is abbreviated to KNMI in Dutch. Data are provided in the GRIB (GRIdded Binary) format. Every file provides information on wind, temperature, and specific humidity on a predefined grid of latitudes and longitudes for various pressure levels. Every file contains a forecast for a specified time in the future, or for the current time. The forecasts from the GRIB files are used to construct the wind predictions that are used in the simulations.

GRIB files recorded at every full hour, ranging from 12:00 on 13-03-2025 to 12:00 on 17-03-2025, are used as the database, as these files were available. Times are expressed in Central European Time (CET). Firstly, the GRIB files are converted to

CSV files, as the data are processed in this form. Then, the GRIB data is sorted based on forecast time, rather than on the time at which the prediction is made. The forecast times used are at every full hour from 12:00 on 14-03-2025 to 12:00 on 17-03-2025, giving 73 forecast times. This way, every forecast time contains a 0-hour forecast, where the prediction time is equal to the forecast time, and 24 forecasts with a prediction time ranging up to 24 hours before the forecast time, with time steps of 1 hour in between. These 24 forecasts per forecast time are referred to as the ensemble, and the 0-hour forecast is referred to as the true forecast. For every ensemble, the mean $\mu$ and standard deviation $\sigma$ of the wind vectors are calculated per grid point of the wind field. Shapiro-Wilk tests were conducted randomly at grid points to assess the normality of the ensemble. As no strong evidence was found to contradict normality, and since assuming a normal distribution for the wind forecast ensembles is accurate enough for this application, it was found to be valid to assume that the ensembles are normally distributed. This leads to four wind fields per forecast time: the 0-hour forecast, the ensemble $\mu$, the ensemble $\mu - \sigma$, and the ensemble $\mu + \sigma$.

*2. Simulation and Track Error Calculations*

All $73 \cdot 4 = 292$ wind conditions were simulated in BlueSky, for various aircraft parameters, routes, and descent types. The same set of aircraft flies in each wind condition. The simulation setup is explained in more detail in section III.F. After the simulations, the data is processed to calculate the along-track and vertical errors. For each of the 73 wind forecasts, the along-track and vertical errors of each aircraft are calculated relative to the aircraft in the 0-hour forecast wind field. In total, this gives 3 along-track and vertical errors per wind forecast, per timestamp.

The vertical error is simply calculated as the altitude difference of the aircraft between the ensemble condition and the 0-hour condition:

$$\epsilon_v = h_{ens} - h_0 \tag{6}$$

The along-track error is drawn in Figure 5. Here, the black aircraft is the reference aircraft, located at the predicted aircraft position at time $t$. The white aircraft is located at the actual aircraft position at time $t$. The angle $trk$ is the track angle of the reference aircraft. It is the angle between the magnetic North and the ground speed vector. The angle $qdr$ represents the magnetic heading to the actual aircraft position. It is the angle between the magnetic North and the line expressing the distance between the two aircraft positions. The distance $d$ is calculated using the latitude and longitude data.

The along-track error is then calculated as:

$$\epsilon_a = \cos\left(trk - qdr\right) \cdot d \tag{7}$$

The aircraft trajectories are split into a cruise segment and a descent segment, to avoid overlap where, at a certain timestamp, an aircraft is in cruise for one wind forecast but already in descent for another. The descent segment is offset such that for each wind forecast, the TOD falls at $t = 0$. With this, every timestamp in every segment contains a sample of $73 \cdot 3 = 219$ data points for the along-track error and the vertical error, for each aircraft. For each sample, the error variance is calculated, allowing for plotting the along-track error variance and vertical error variance over time for the cruise and descent segments, per aircraft.

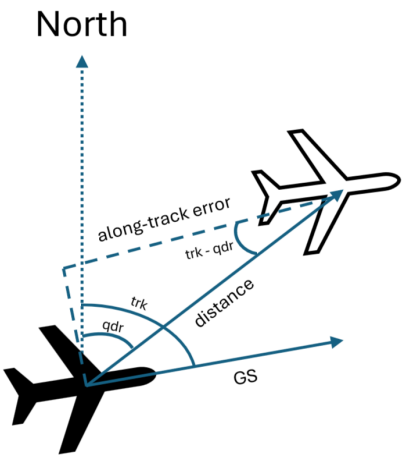


**Figure 5 Visualisation of along-track error.**

*3. Model Parameter Generation*

Curve fits are constructed on the error variances for each aircraft. From these curve fits, the model structure and parameters of $\sigma_a^2$ and $\sigma_v^2$ are found. Different model structures are identified for idle and fixed-FPA descents. As the model structures involve separate segments, curve fits are made for each segment. Additionally, different uncertainty parameters are chosen based on the different aircraft parameters used in the simulations. This means that Light, Medium, and Heavy aircraft all have different uncertainty parameters, while adhering to the different idle and fixed-FPA model structures. The uncertainty parameter values were averaged over the different routes used in the simulations, as all routes showed the same model structure.

The uncertainty parameters described above are referred to as the first uncertainty parameter set. In addition, a second set is constructed to assess the influence of trajectory uncertainty magnitudes on the number of successful idle descents under various criteria. This second set is chosen such that the error standard deviations $\sigma_a$ and $\sigma_v$ are twice as high as for the first set. Essentially, this means that the trajectory uncertainty is doubled. Therefore, the error variance uncertainty parameters for $\sigma_a^2$ and $\sigma_v^2$ of the first set are multiplied by 4 to obtain the second set. The values of $\sigma_a^2$ and $\sigma_v^2$ for both sets are used as the uncertainty model for the conflict probability model described in section II.A.3.

### F. Uncertainty Simulation Setup

As stated in section III.E, 292 wind conditions were simulated in BlueSky for various aircraft parameters, routes, and descent types. The descent types are an idle descent and a fixed-FPA descent at 2.5 deg. Furthermore, three routes were selected,

one to each IAF. This ensures the wind fields are encountered from different directions, as the trajectories are flown towards the West, North, and East. In Table 1, the routes used are shown. The first waypoint is the starting waypoint of the route. The second waypoint is the first waypoint of the STAR to be flown once the Dutch FIR is entered. The last waypoint is the IAF, where the route ends.

**Table 1 Routes used in the simulations.**

| Route Nr. | Waypoints | Route Direction |
|---|---|---|
| 1 | ROBEG-NORKU-ARTIP | West |
| 2 | LESDO-HELEN-RIVER | North |
| 3 | SUPEL-MOLIX-SUGOL | East |

Furthermore, three aircraft types were chosen. For each type, a cruise speed, descent speed, and cruise altitude were selected. The results are shown in Table 2. Combining the parameters, routes, and descent types leads to 18 aircraft to be simulated per wind condition. The scenario files, which are called during each simulation, each contain all 18 aircraft and one of the 292 wind conditions. The specifics for each aircraft, by combining Table 1 and Table 2, are displayed in Table 7, shown in Appendix A.A.

**Table 2 Aircraft parameters used in the simulations.**

| Type | Cruise Alt. | Cruise Spd. | Descent Spd. |
|---|---|---|---|
| E190 | FL350 | 0.74 M | 250 KCAS |
| B737-800 | FL370 | 0.78 M | 280 KCAS |
| B787-800 | FL390 | 0.84 M | 310 KCAS |

A simulation framework was set up in which BlueSky was run in "sim-detached" mode, meaning no user interface was called at startup. BlueSky was called from a function with as inputs a configuration file, the scenario file to be run, and the run directory relative to BlueSky. This function was called in a subprocess, ensuring the correct closure of BlueSky before calling the function again. Each time BlueSky was called, a new scenario file with a different wind condition was used as input. This enables the automatic execution of all scenarios, eliminating the need for manual intervention. In total, four subprocesses were created so that BlueSky could be started four times in parallel. This setup was found to be the most optimal for CPU usage and needed minimal manual intervention. When a simulation was completed, a log file containing the simulation data was written. The log files were used for processing the simulation data, as explained in section III.E.

### G. Resulting Trajectory Uncertainty Models

Firstly, the along-track model is presented and elaborated on. This is followed by the vertical model. The order of magnitude of the uncertainties is presented afterwards.

*1. Along-Track Model*

In Figure 6, the along-track error variance model found from the trajectory uncertainty simulations is presented over time for a B738 aircraft using the first parameter set. Its current position is in cruise, and its lookahead is until the IAF is reached.

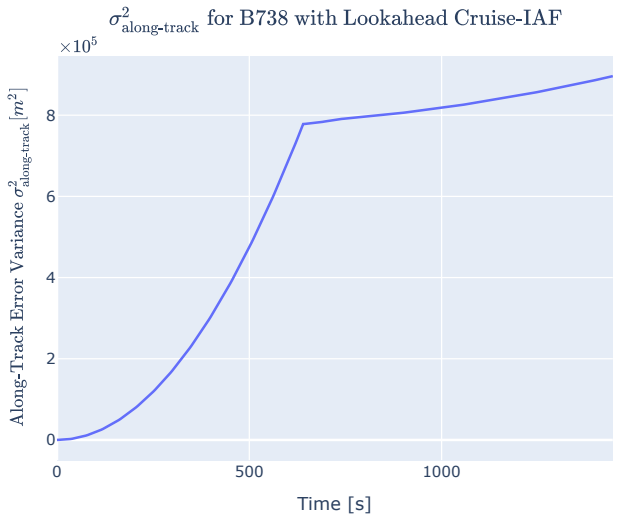


**Figure 6 Along-track error variance for a B738 in cruise, with lookahead until the IAF is reached.**

It can be observed that the along-track error variance is constructed from three parabolas, essentially creating three separate segments. The first parabola is due to the cruise phase. As mentioned in section II.A.3, the along-track error variance was assumed to grow quadratically in cruise. This assumption was validated with the trajectory uncertainty simulations. For completeness, this is shown in Figure 23, in Appendix A.C.

The second parabola starts at the TOD and lasts until the crossover altitude. The last parabola starts at the crossover altitude and continues until the IAF is reached. In Figure 7, the along-track error variance results for descents from the trajectory uncertainty simulations are shown for the route to SUGOL.

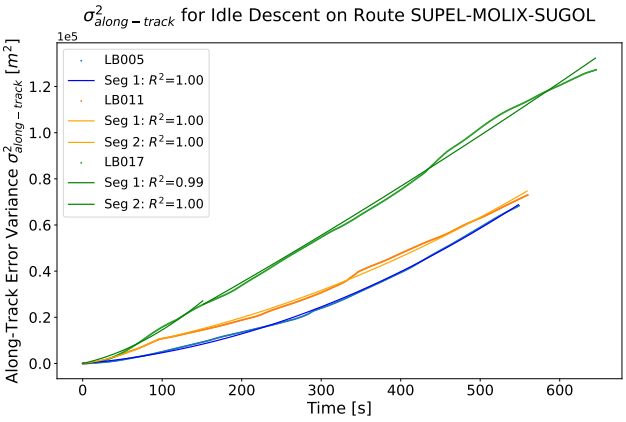


**Figure 7 Along-track error variance for idle descents with quadratic curve fits.**

The aircraft IDs correspond to the data in Table 7, given in Appendix A.A.

The quadratic curve fits on these results confirm the parabolic nature of the along-track error variance for descent. It was found that a new parabola starts at the crossover altitude due to the change in descent speed. Since a speed change also happens at the TOD, a new parabola is started here as well. For reference, the speed changes at the TOD and the crossover altitude can be observed from Figure 25 in Appendix A.E. It must be noted that for LB005 in Figure 7, the cruise altitude is almost at the crossover altitude, meaning that no speed change is present. Therefore, only one descent parabola is present. It was found that the along-track error variance for a fixed-FPA descent has the same parabolic behaviour as for an idle descent. Therefore, showing an example of an idle descent is sufficient to demonstrate the along-track error variance model.

### 2. *Vertical Models*

For the vertical error variance, the idle and fixed-FPA descent exhibit different behaviour. Therefore, two separate models were identified. In Figure 8, the vertical error variance model found from the trajectory uncertainty simulations is presented over time for a B738.

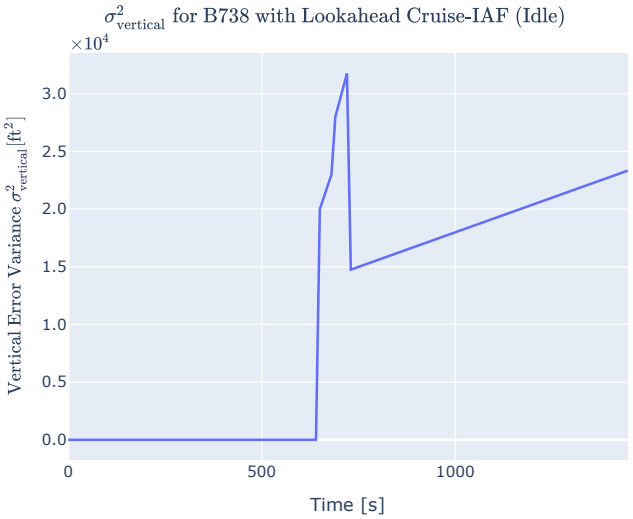


**Figure 8 Vertical error variance for a B738 in cruise, about to fly an idle descent, with lookahead until the IAF is reached.**

Again, the first parameter set is used. The aircraft is in cruise and planning to execute an idle descent. Here, various linear segments are observed. Firstly, the variance is zero during the cruise phase. This was assumed as the altitude hold capabilities of the autopilot are sufficient. The BlueSky autopilot performance confirmed this. After the cruise segment, six segments are identified during descent. A steep increase is observed at the TOD, due to the uncertainty of where the TOD lies in time. The next segment starts at the TOD and ends at the tropopause boundary. Then, a steep increase is observed at the tropopause boundary because of a change in descent angle $\gamma$, as will be explained later. Afterwards, a new segment ranges from the tropopause to the crossover altitude. A steep drop is observed at the crossover altitude, again due to a change in $\gamma$. The last segment ends when the IAF is reached.

In Figure 9, the vertical error variance results for idle descents from the trajectory uncertainty simulations are shown for the route to ARTIP. Here, the six segments are clearly present. The linear behaviour is confirmed with curve fits.

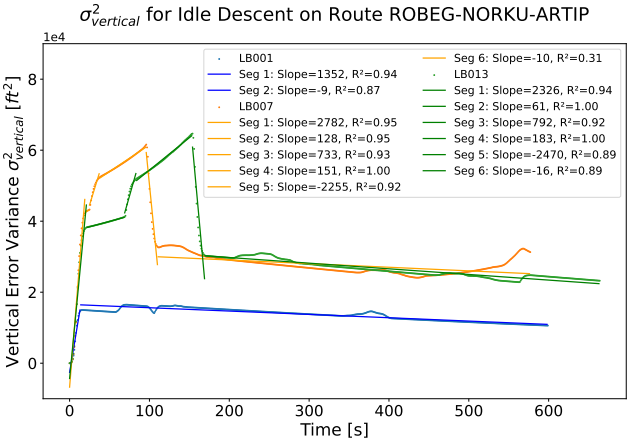


**Figure 9 Vertical error variance for idle descents with linear curve fits.**

The steep segments are caused by changes in descent angle $\gamma$. An idle descent is flown at the most optimal $\gamma$ depending on the flight conditions. The changes in $\gamma$ due to changing flight conditions are sudden. They occur at the TOD, the tropopause boundary, and the crossover altitude. Due to uncertainty about when in time these $\gamma$ changes occur, the vertical error variance changes rapidly during this time, causing the steep segments. This can be explained by comparing the same aircraft flying towards the TOD in two different wind conditions. The time difference between reaching the TOD is the time during which both aircraft fly at different $\gamma$ values. The absolute value of $\gamma$ increases when reaching the TOD, leading to a steep increase of the vertical error variance. On the other hand, at the crossover altitude the $\gamma$ becomes less negative, so its absolute value decreases. Using the same logic as above, the segment at the crossover altitude is now expected to decrease steeply due to the sudden decrease in $\gamma$. This can be observed from Figure 9. For reference, Figure 25 in Appendix A.E contains flight data of an aircraft flying an idle descent. It must be noted that the aircraft used here was flying below the tropopause boundary. The graph of descent angle $\gamma$ shows sudden changes in $\gamma$ at both the TOD and the crossover altitude. The crossover altitude is marked by the grey dashed lines.

As can be seen for LB001 in Figure 9, not all aircraft cruise above the tropopause boundary and above the crossover altitude. Because of this, the vertical error variance for LB001 only has two segments. The first is the increase at TOD, and the second continues until the IAF is reached. This shows that segments are only present when applicable. For every aircraft in the descent criteria simulations, the segments are assigned as applicable.

In Figure 10, the vertical error variance model found from

the trajectory uncertainty simulations is presented over time for a B738 planning to execute a fixed-FPA descent. Similarly to the models above, the first parameter set is used.

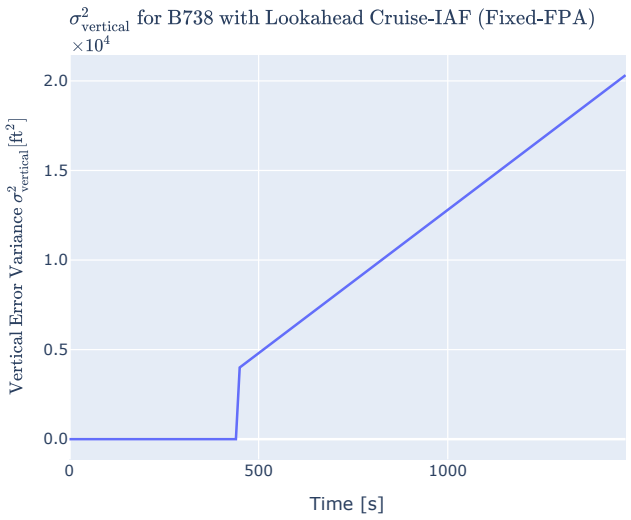


**Figure 10 Vertical error variance for a B738 in cruise, about to fly a fixed-FPA descent, with lookahead until the IAF is reached.**

Comparing this model to the idle model, it is clear that again linear segments can be observed. However, the fixed-FPA descent consists of only two segments. The first segment is the steep increase at the TOD and follows the same logic as described for the idle descent. The second segment ranges from the TOD to the IAF. In Figure 11, the vertical error variance results for fixed-FPA descents from the trajectory uncertainty simulations are shown for the route to RIVER. Here, the linear behaviour of the two segments is confirmed with curve fits.

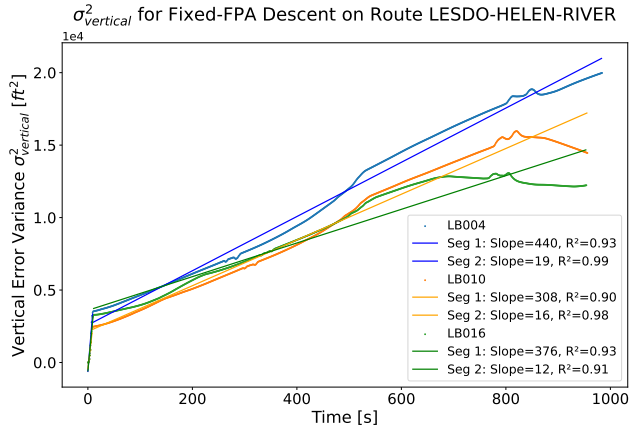


**Figure 11 Vertical error variance for fixed-FPA descents with linear curve fits.**

It should be noted that the tropopause and crossover altitude have no influence on the vertical error variance of a fixed-FPA descent. This is because at the TOD, the absolute value of $\gamma$ increases from 0° to 2.5°, with some overshoot at the beginning. The $\gamma$ is kept at 2.5° throughout the flight. Therefore, no changes in $\gamma$ are present at the tropopause boundary and the crossover altitude, which does happen for an idle descent. As a result, the vertical error variance of a fixed-FPA descent consists of two segments. For reference, the constant $\gamma$ can be observed from flight data of a fixed-FPA descent, displayed in Figure 26, shown in Appendix A.E.

### *3. Trajectory Uncertainty Order of Magnitude*

As mentioned in section III.E.3, the first parameter set was chosen by averaging the curve fit parameters over the routes for each aircraft weight category. The second set was then generated by multiplying all variance parameters by 4, so that the standard deviations are doubled. Because of this, the variance plots for the second set only changed in magnitude compared to those shown in this section. Each aircraft in the descent criteria simulations is assigned trajectory uncertainty parameters that are applicable to its situation. The error variance graphs are shifted such that at the current time, the variance is always 0. The lookahead is always until the IAF is reached. The segments related to the crossover altitude and tropopause are only present when applicable for that aircraft.

To make the trajectory uncertainty parameter sets tangible, the error variances were calculated for all aircraft, with the current position being the aircraft's spawn point. This ensures the highest possible uncertainty at the IAF. The variances were then converted to standard deviations. A 95% confidence interval is constructed using $\mu \pm 1.96\sigma$. Therefore, $1.96\sigma$ is of interest when quantifying trajectory uncertainty. The maximum uncertainties found across all aircraft are expressed as $1.96\sigma$ in Table 3, for various lookahead times. The along-track values are denoted with AT, and the vertical values with V.

**Table 3 Maximum trajectory uncertainty expressed in the 95% confidence interval.**

| Unc. Set | Lookahead | Descent | AT ± | V ± |
|---|---|---|---|---|
| Low | 20 min | Idle | 1.16 nm | 363 ft |
| High | 20 min | Idle | 2.32 nm | 726 ft |
| Low | 20 min | Fixed-FPA | 1.03 nm | 308 ft |
| High | 20 min | Fixed-FPA | 2.06 nm | 616 ft |
| Low | 30 min | Idle | 1.97 nm | 387 ft |
| High | 30 min | Idle | 3.94 nm | 774 ft |
| Low | 30 min | Fixed-FPA | 1.81 nm | 314 ft |
| High | 30 min | Fixed-FPA | 3.62 nm | 628 ft |

## IV. Main Experiment Design

Central to this research are descent simulations from which criteria for applying idle and fixed-FPA descents are identified. This section explains how these simulations are designed. It shows how the research methodology is linked to the literature discussed in section II and the preliminary research presented in section III.

## A. Research Design

From the preliminary research, trajectory uncertainty models are identified. High and low uncertainty parameter sets are constructed and are important variables in the research. It was stated earlier that the aim of this research is to develop criteria for the application of idle and fixed-FPA descents, and analyse the resulting numbers of successfully flown idle descents. The research design is discussed here.

### *1. General Outline*

Various traffic scenarios are constructed that contain varying traffic densities throughout the day, and execution restrictions in time frames for the application of idle descents. These scenarios will be referred to as reference scenarios. Next to these, the trajectory uncertainty parameters and models obtained in the preliminary research are used to develop criteria for the application of idle and fixed-FPA descents and investigate the effects on the number of successfully flown idle descents. The criteria are determined based on the conflict probabilities, aircraft spacing, and IAF arrival times of the descents in various reference scenarios, as stated above. They are tailored to the level of individual flights, allowing the application of idle and fixed-FPA descents to be conducted on a per-flight basis.

The high and low uncertainty parameter sets are used for a sensitivity analysis on how the number of successful idle descents varies with uncertainty under various reference scenarios and criteria sets. Furthermore, the influence of the reference scenarios and criteria sets themselves on the number of successful idle descents is investigated. The exact details of how this is done are explained below.

### *2. Research Variables*

The research variables are formulated based on the main objective of this research. The first part of the objective revolves around developing criteria sets for the application of idle and fixed-FPA descents. The second part focuses on analysing the effects on the number of successful idle descents.

As stated above, various reference scenarios with idle descent execution restrictions are considered. Outside of these constraints, only fixed-FPA descents may be applied. Since a 24-hour operation is considered, varying traffic densities are encountered in each reference scenario. An overview of the reference scenarios to be used in the traffic simulations is provided in Table 4. The constraints are based on fixed time windows and traffic densities.

In the first scenario, idle descents may only be initiated at night between 00:00 and 04:00 LT (Local Time). In the second scenario, this time window is extended from 23:00 to 06:00 LT. This resembles the current implementation at Schiphol, where idle descents are only allowed at night. The third scenario allows for idle descents throughout the day, except during peak hours. How the peak hours are determined is explained later. In the final scenario, idle descents may be applied throughout the day. The percentage of the total flights that may become idle descents in each scenario is indicated in the table. Below the table, all independent variables are listed and explained.

**Table 4 Reference scenarios used in the simulations.**

| Name | Description | Flights |
|---|---|---|
| MIDNIGHT | Idle initiated at 00:00-04:00 LT | 0.3% |
| FULLNIGHT | Idle initiated at 23:00-06:00 LT | 2.6% |
| OFF-PEAK | Idle allowed outside peak hours | 39.2% |
| FREE | No restrictions | 100% |

*Independent variables:*

- Uncertainty parameters: low and high uncertainty parameter sets, as obtained from the preliminary research.
- Time frames for idle descent allocation: these time frames are used in the reference scenarios, which contain traffic derived from radar data. Four time frames and thus four reference scenarios are chosen, as shown in Table 4.
- Idle descent criteria sets: idle and fixed-FPA descent allocation based on distance and time criteria. Three criteria sets are designed in this research, referred to as sets 1, 2, and 3 or as medium, strict, and lenient, respectively. Additionally, set 0, or the zero set, describes the situation where no distance and time criteria are applied. Therefore, a total of four different criteria options are used in this research.

Two uncertainty parameter sets, four time frames, and four criteria sets give a 2x4x4 experiment design. This results in 32 unique combinations for which a dependent variable analysis is conducted. All dependent variables are listed below.

*Dependent variables:*

- Number of conflicts involving idle descents: these follow from the conflict probability calculations.
- Aircraft spacing: nominal distances between aircraft over the full flight, to be used in the conflict probability model.
- Arrival times at the IAF: arrival times following from the nominal trajectories, which are the predicted trajectories.
- Number of successfully flown idle descents: expressed as both a number and a success rate.

To develop the medium, strict, and lenient criteria sets, the FREE scenario and the low uncertainty parameter set are used. Obviously, no distance and time criteria are applied yet, meaning that technically, the zero set is used here. The developed criteria sets result from a post-simulation analysis of the dependent variables. More specifically, the number of conflicts, aircraft spacing, and IAF arrival times are analysed.

Based on the developed criteria sets, idle and fixed-FPA descents will be reassigned within the allowed time frames in each reference scenario. This results in a total of 16 unique idle descent allocations and thus traffic scenarios, all of which are simulated in BlueSky. The two uncertainty sets are applied to all simulations, leading to the 32 unique combinations mentioned earlier. For every combination, the number of successfully flown idle descents is analysed.

A diagram, illustrating the relationships between the independent and dependent variables through simulations, is pre-

sented in Figure 12. The independent variables are depicted in orange, the dependent variables in green, and the simulations in blue. The workflow presented in the diagram is elaborated on in detail in section III.E and section IV.C.

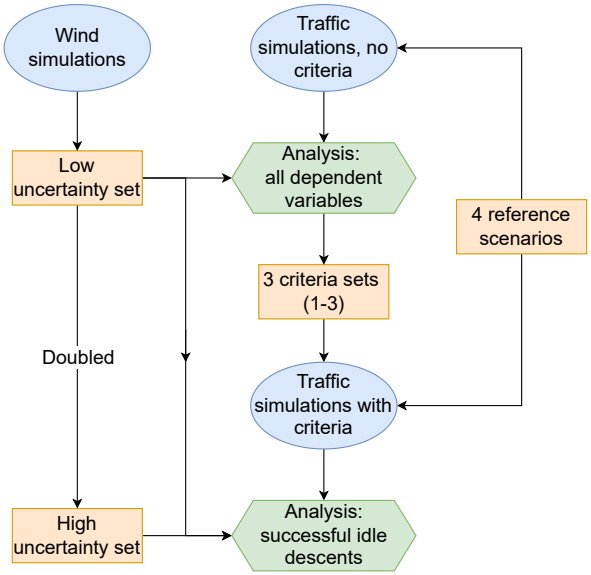


**Figure 12 Overview of how the dependent variables relate to the independent variables and simulations.**

It must be noted that the aircraft spacing and IAF arrival times are independent of the uncertainty parameters, because these are based on the simulated nominal flight trajectories. Trajectory uncertainty is then added to the nominal path to determine the conflict probabilities and calculate the number of conflicts.

*3. Hypotheses*

Hypotheses regarding the influence of the independent variables on the dependent variables are formulated. In total, this research considers three hypotheses:

- **H1: The strictness of the reference scenario and the number of successful idle descents have an inverse relationship.** Overall, it is expected that the most idle descents can be flown successfully when the restrictions from the reference scenario are the least strict. In practice, this means that it is expected that the most idle descents can be flown when idle descents are allowed throughout the full day. This way, the per-flight idle descent allocation can be exploited to the fullest. On the other hand, the smallest number of successful idle descents is expected under the strictest reference scenario.
- **H2: The strictness of the descent criteria and the number of successful idle descents have an inverse relationship.** Overall, the highest number of successful idle descents is expected when the idle descent criteria, which allocate idle descents on a per-flight basis, are the least strict. On the other hand, the smallest number is expected when the idle descent criteria are the strictest.
- **H3: Trajectory uncertainty and the number of successful idle descents have an inverse relationship.** A strong relation between trajectory uncertainty and the number of successful idle descents is foreseen. With greater uncertainty, the success rate is predicted to decrease.

## B. Assumptions

The descent application criteria are developed using several assumptions. These are listed and explained below.

- A lookahead of around 20 minutes is needed for trajectory prediction and uncertainty modelling from the TOD to the IAF. Therefore, Medium-Term Conflict Detection (MTCD) methods are considered.
- The effect of wind correlation on conflict probability is neglected. Wind correlation causes the wind vectors and thus aircraft trajectories in close proximity of each other to be coupled. By neglecting this correlation, the conflict probabilities will be overestimated [24]. This is a conservative assumption and allows for the use of the conflict probability model described in [33].
- It is assumed that IAS is equal to CAS. At higher airspeeds and altitudes, IAS and CAS are approximately the same, making this assumption valid.
- Every aircraft flying a fixed-FPA descent uses the same constant geometric FPA of 2.5 deg, which is shown to be the optimal angle [12, 14, 38].
- The altitude constraint at each IAF is assumed to be at FL100. In reality, any altitude from FL70 to FL100 is allowed. The desired altitude then depends on the runway allocation. This would lead to higher model complexity and is beyond the scope of this research.
- Aircraft can only fly the descent type (idle or fixed-FPA) designated before the TOD. Switching descent type during flight increases model complexity and is beyond the scope of this research.
- In the simulations, no ATC intervention or metering is considered. No speed changes leading to more successful idle descents are allowed, as this would increase model complexity significantly and is beyond the scope of this research.

## C. Developing Criteria for Idle and Fixed-FPA Descent Applications

Using the identified trajectory uncertainty models from section III, the descent criteria can be developed and the dependent variables can be analysed. Firstly, traffic is generated and simulations are run. Then, a conflict analysis is conducted and the criteria are developed. Then, the effects of the criteria on the flown idle descents are analysed. These steps are explained in detail below.

*1. Traffic Generation and Simulations*

Realistic traffic is needed to evaluate the developed criteria and other variables considered. Therefore, radar data of aircraft inbound to Schiphol Airport on the full day of 28-02-2024 are used to set up the BlueSky simulations. This specific day was chosen simply because the radar data were available for this research. Also, the aim is to develop general criteria that should be applicable to any day, meaning that radar data of any regular day should suffice. Any regular day contains both high traffic peaks and periods of low traffic density in various regions.

A dashboard was developed to visualise the radar data, allowing for the verification of the data processing conducted on the radar data. The simulations require a starting position for each aircraft, which in this case must be in cruise. This 'spawn point' is chosen to be the first position visible in the radar data. However, some aircraft from e.g. London or Düsseldorf are still climbing when visible on radar for the first time. For all these aircraft, the first data point in cruise is chosen as the spawn point. Aircraft departing from Schiphol Airport and returning because of an emergency are excluded from the data, as only representative descents from cruise to the IAF are considered. An aircraft is deleted in the simulation when it has reached the IAF.

Some aircraft types in the radar data are not available in BlueSky. These types are converted to available types with the closest resemblance. Furthermore, the types are categorised into either Light, Medium, or Heavy, depending on their RECAT classification. Each category is assigned a different speed schedule, with a cruise speed in Mach and a descent speed in KCAS.

Four reference scenarios with different descent application constraints are constructed. These constraints restrict the possibility to apply an idle descent specifically, as a fixed-FPA descent is flown alternatively. No conventional step-down descents are considered. The reference scenarios were explained in detail in section IV.A, but are summarised here. The first two reference scenarios contain time frames at night during which idle descents are permitted to be initiated. The third reference scenario states that idle descent may be flown only outside peak hours. In the fourth reference scenario, idle descents may be flown at any time. The information on peak hours for the third scenario is derived from the radar data. For every hour, the number of aircraft flying to an IAF is counted. If at least 65 aircraft are counted, the hour is labelled as peak hour. In Figure 24, shown in Appendix A.D, the number of aircraft flying to an IAF is displayed per hour. From this, the peak hours become apparent.

The same approach is used for each reference scenario. The spawn points are exactly the same. For the first simulation set, all aircraft are assigned idle descents within the application constraints of the reference scenario. These application constraints were shown in Table 4 and elaborated on in section IV.A. The results of the fourth scenario (FREE) are used to develop the descent criteria, as will be explained later.

*2. Conflict Probability Model Implementation*

The simulation results represent the nominal (or 'mean') paths denoted in the conflict probability model described in section II.A.3. This means that the trajectories flown in the simulations are considered to be the trajectories predicted by a Trajectory Predictor (TP). The current position of an aircraft can be any position on the nominal path. The trajectory uncertainty is then calculated for the remaining lookahead time until the IAF is reached. The remaining simulated trajectory as the nominal path is used for this, and the error variance parameters on this path, found from the uncertainty models established in section III.E, are applied. These models are always calculated from the time at the spawn point towards the time at the IAF. The graph is then shifted such that an error variance of zero aligns with the time at the current aircraft position. The resulting error variance over time then applies to the remaining lookahead time until the IAF. For any aircraft, the maximum lookahead time for the cruise and descent phases separately is approximately 20 minutes, meaning that MTCD methods are applicable.

The conflict probabilities over time between any aircraft pair are calculated by analysing the timestamps for which both aircraft are still to reach the IAF, starting from the current timestamp. The error variance graphs for $\sigma_a^2$ and $\sigma_v^2$ are constructed for both aircraft. With Equation 2, the covariance matrices are calculated. An illustrative example of two aircraft and their uncertainty is given in Figure 13. The along-track, cross-track, and vertical errors are indicated.

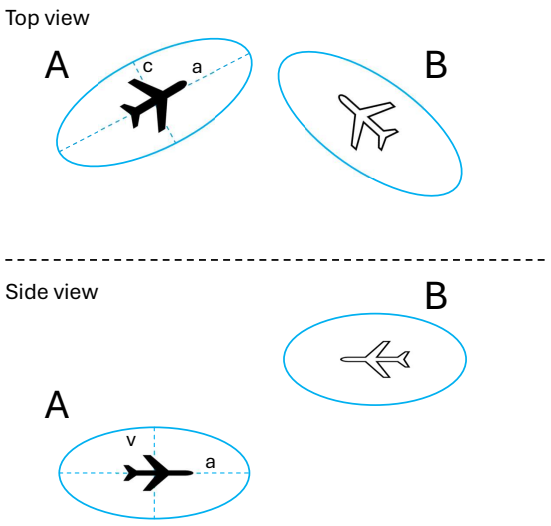


**Figure 13 Two aircraft with uncertainty ellipsoids.**

In accordance with Equation 3, the nominal distances $\vec{\mu}(t)$ and combined covariance matrix $Q(t)$ are calculated. From these, a *multivariate normal* (a 3D Gaussian distribution) is constructed. The visualisation of this is a 3D ellipsoid. For every timestamp, this ellipsoid changes since $\sigma_a^2$ and $\sigma_v^2$ change over time, as explained earlier.

Theoretically, the conflict probabilities (PC) are calculated using Equation 4. In practice, this operation is tedious. It often takes a long time and gives wrong answers when the probability density functions are narrow or sharp, and when the covariance matrix is singular. This can happen when both aircraft are in cruise, because the vertical error variance is then zero. There-

fore, Monte Carlo sampling is used. Essentially, the 3D ellipsoid is reconstructed by taking 1 million samples of the 3D Gaussian distribution. For every sample, it is calculated whether it lies within the Protective Zone (PZ). The ratio between the number of samples within the PZ and the total number of samples is then the PC. If no samples lie within the PZ, then $PC = 0$. If all samples lie within the PZ, then $PC = 1$. The conflict probability between the two aircraft shown above in Figure 13 is illustrated in Figure 14. The overlap between the PZ and the 3D distance ellipsoid $\Delta$ is shown.

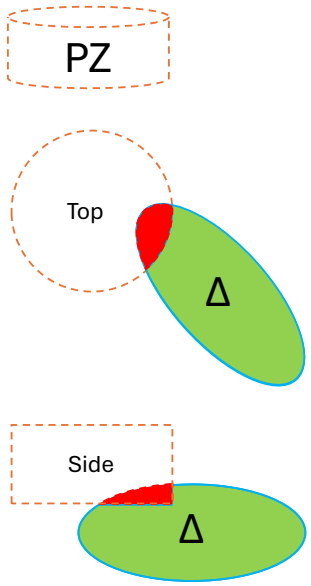


**Figure 14 Conflict probability shown as the overlap between the PZ and the distance ellipsoid.**

A dashboard is created that visualizes aircraft positions, flight parameters, and conflict probabilities over time. With this, the calculations and resulting outcomes could be visually verified. Furthermore, the dashboard provides great insight into the type and location of conflicts encountered. In addition, conflict probabilities can be visually linked to nominal distances and associated 3D ellipsoids, thereby increasing understanding of the situations dealt with.

### *3. Criteria Development*

Naturally, the highest trajectory uncertainties are encountered at the highest lookahead time. Therefore, it is desirable to develop descent criteria based on these uncertainties. It is important to note that the criteria are developed using the first trajectory uncertainty parameter set, as this is the set that was determined from simulations. For every aircraft A, its spawn point is taken as the current position and timestamp. Then, all other aircraft flying to the same IAF and in view at that timestamp are identified. For all these aircraft, the error variances are calculated based on their current position (at the timestamp of the spawn point of aircraft A). The conflict probabilities with aircraft A are then calculated as described above. This is done for every aircraft throughout the day, such that all aircraft pairs and corresponding conflict probabilities over time are captured exactly once. Furthermore, the nominal distances over time and the difference in arrival time at the IAF are calculated and stored. The above is done for the FREE scenario of the first simulation set, where only idle descents are flown throughout the day. This is because the descent criteria are focused on the application of idle descents and are designed to omit any conflicts between two aircraft on idle descents. From the analysis of the FREE scenario, explicit restrictions for assigning idle descents can be developed.

For every aircraft pair in conflict, the exact future timestamp at which the predicted conflict probability becomes non-zero is of particular interest. Based on the nominal aircraft spacing at this first non-zero PC timestamp and the difference in arrival time at the IAF, a set of idle descent criteria is formulated. This is the medium set. Based on this, a strict set is formulated, requiring a larger spacing and greater IAF time difference. Lastly, a lenient set, requiring a smaller spacing and the same IAF time difference, is formulated. Thus, three descent criteria sets are formulated. These sets will be presented in the results, in section VI.A.

### *4. Idle Descent Reassignment and Data Analysis*

For each reference scenario, the idle and fixed-FPA descents are reassigned based on the three descent criteria sets. These three new sets of simulations are run in BlueSky. For all simulations, the conflict probabilities between every aircraft pair are calculated as described in section IV.C.3. This is now done for both trajectory uncertainty parameter sets mentioned in section III.E, in order to assess the effectiveness of the criteria for under different trajectory uncertainties. For every unique combination of reference scenario, criteria set, and uncertainty parameter set, the number of successful idle descents is analysed.

This information is used to compare the performance and effectiveness of the descent criteria sets for different uncertainty parameter sets in a sensitivity analysis. Furthermore, it provides insight into the potential idle descents throughout the day for different application constraints in the reference scenarios.

## V. Experimental Setup

The experiments conducted in this research were performed through simulations. In this section, the simulation setups and structures are explained in detail. First, the speed schedule assignment is discussed. Then, an overview of the simulations is provided.

### A. Speed Schedule Assignment

As stated in section IV.C.1, the aircraft types found from the radar data are converted to similar aircraft types available in BlueSky if needed. Then, all types are categorised into either Light, Medium, or Heavy, depending on their RECAT classification. Each category is then assigned a cruise speed and descent speed for the simulations. In Table 5, the speeds corresponding

to the categories are presented. As stated earlier, the cruise altitude is directly derived from radar data and is thus unique for each aircraft.

**Table 5 Assigned speed schedules from RECAT.**

| Category | RECAT | Cruise Spd. | Descent Spd. |
|---|---|---|---|
| Light (L) | E-F | 0.74 M | 250 KCAS |
| Medium (M) | D | 0.78 M | 280 KCAS |
| Heavy (H) | A-C | 0.84 M | 310 KCAS |

### B. Simulation Overview

A Python script is written that automatically takes the predefined spawn points of each aircraft, explained in section IV.C.1, and assigns a speed schedule based on Table 5 and an idle or fixed-FPA descent based on the constraints for each reference scenario according to Table 4. This gives a BlueSky scenario file for each reference scenario, meaning that one simulation set consists of four BlueSky simulations.

In section IV.C.3, it is explained how three criteria sets are determined from this first simulation set. These three criteria sets are then used to generate three new simulation sets with reassigned idle descents, under each reference scenario. Therefore, a total of 16 BlueSky simulations are performed. Every simulation is referred to by using the reference scenario name from Table 4, and adding '_{*num*}', with *num* the number of the criteria set. Here, 0 indicates the first simulation set, where no criteria other than the reference scenario constraints are enforced. Numbers $1-3$ refer to the criteria sets in the same order as explained in section IV.C.3, with 1 the medium set formulated from the analysis, 2 the strict set, and 3 the lenient set. This notation will be used frequently when discussing the results. An overview of all 16 BlueSky simulations with this notation is provided in Table 8, shown in Appendix A.B.

Both trajectory uncertainty parameter sets, described in section III.E.3, are applied to all 16 simulations. In section IV.C.3, it was explained that the low uncertainty set and the FREE scenario were used to develop the three descent criteria sets. However, the performance of the idle descents in all 4 criteria sets (including number 0 without criteria) is of interest for all reference scenarios and both trajectory uncertainty parameter sets, meaning that $16 \cdot 2 = 32$ unique results are analysed.

## VI. Results

In this section, the main results of this research are presented. The dependent variable analysis from which the descent criteria sets are formulated is presented, along with the criteria sets. Then, the assigned and successful idle descents resulting from the simulations using all reference scenarios, criteria sets, and uncertainty parameter sets are visualised.

### A. Criteria from Idle Descent Performance

As explained in section IV.C.3, FREE_0 is the reference scenario used for the criteria development, as the aim is to omit idle-idle conflicts. Furthermore, the highest uncertainties are used, which are encountered at the highest lookahead times. Therefore, the aircraft's spawn position is taken as the current position, with a lookahead until the IAF is reached. In other words, the spawn position is the actual position of the aircraft and from this point towards the IAF, a trajectory prediction is made. Over this predicted trajectory, the conflict probabilities are calculated for each timestamp. These are thus the predicted conflicts throughout the trajectory towards the IAF. The first uncertainty parameter set is used, as determined from the uncertainty simulations. Firstly, to validate the calculated predicted conflict probabilities throughout the lookahead time, the nominal aircraft distances at maximum predicted conflict probability PC are plotted for all aircraft pairs in conflict. The result is shown in Figure 15. The PZ with a radius of 5 nm horizontally and a length of 2000 ft vertically is shown with the dashed lines.

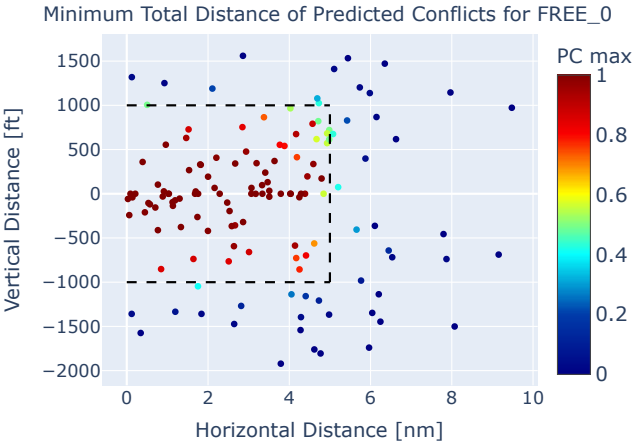


**Figure 15 Nominal aircraft distance at maximum predicted conflict probability for conflicting aircraft pairs.**

The nominal aircraft distances serve as the predicted distances (the mean) since these are simulated. These are the centres of the probability ellipsoids. It can be observed that the nominal distances of aircraft pairs with high predicted conflict probabilities are located in the PZ, while those of aircraft pairs with low predicted conflict probabilities are located outside the PZ. The nominal distances of the aircraft pairs with a conflict probability of around 50% are located on or near the PZ border. This is because half of the probability ellipsoid then lies inside the PZ, while the other half lies outside. All these results are expected and validate the implementation.

In section IV.C.3, it was mentioned that the exact predicted timestamp and nominal distances where the predicted PC becomes nonzero for an aircraft pair in conflict are of particular interest to develop the descent criteria, as these indicate the start of the predicted conflict. This is because a nonzero conflict probability indicates the possibility of a conflict at that particular time in the future. The corresponding predicted nominal distance is then the border between no chance of conflict at that time, or a

nonzero chance of conflict. The time at which this is predicted to occur will be referred to as the conflict start. Figure 16 shows the nominal aircraft distances at the start of the predicted conflict, for each aircraft pair in conflict.

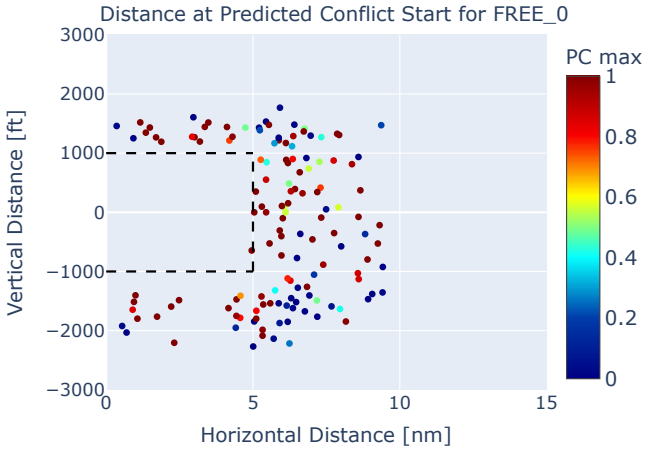


**Figure 16 Nominal aircraft distance at the predicted timestamp at which the predicted conflict probability becomes nonzero, for conflicting aircraft pairs.**

It can be observed that, as expected, the predicted conflict probabilities become nonzero when the nominal distances between the aircraft are still outside the PZ, as a result of the associated trajectory uncertainties. In addition, it is clear that most conflicts are predicted to start when the predicted nominal horizontal distance is less than 10 nm and the vertical distance less than 2000 ft. Because of this, these numbers are used in the first criteria set, which will be formulated later.

Another parameter of interest is the predicted time difference of arrival at the IAF. In Figure 17, these time differences are shown.

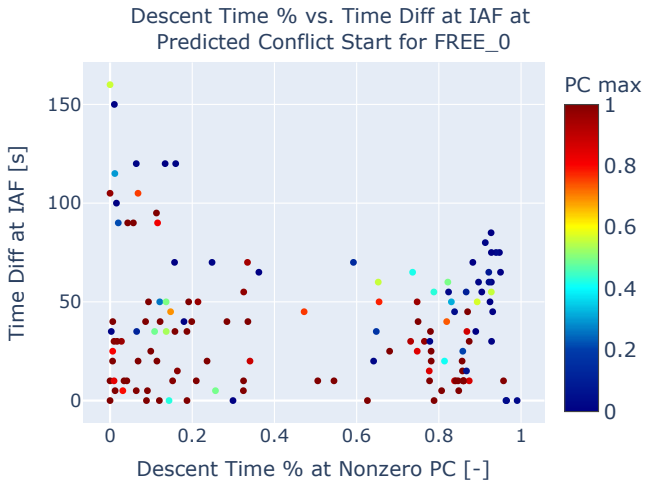


**Figure 17 Predicted arrival time difference at the IAF for conflicting aircraft pairs, plotted against the ratio of descent time at the predicted start of the conflict.**

On the x-axis, the average descent time of an aircraft pair in conflict at the start of that conflict (when the predicted conflict probability becomes nonzero) is shown as the ratio of the full descent time.

The figure shows that most conflicts are predicted to occur either at the start of the descent or at the end, when aircraft are merging towards the IAF. Especially close to the IAF, the arrival time difference is important. It can be seen that no conflicts are predicted to occur near the IAF when the arrival time difference is larger than 90 seconds. Therefore, this number is used when formulating the first criteria set.

The clear split in conflict occurrence can also be visualised by plotting the average descent time of an aircraft pair in conflict at the predicted start of that conflict against the average altitude at that moment. This is done in Figure 18, for FREE_0 again.

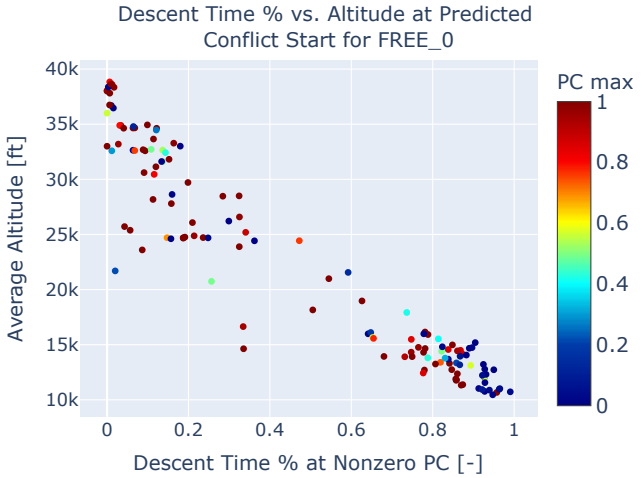


**Figure 18 The predicted conflict start visualised in terms of descent time ratio and altitude for conflicting aircraft pairs.**

Logically, aircraft are close to their cruising altitude for conflicts that are predicted to occur earlier in the descent and close to the IAF altitude constraint of FL100 for the conflicts that are predicted to occur late in the descent. In the formulated criteria sets, the constraint of arrival time difference at the IAF is used to mitigate the conflicts that occur when merging towards the IAF, while the distance constraint is used to also mitigate the conflicts that occur at the start of the descent.

As explained, the first criteria set is formulated based on the graphs above. A second and third criteria set are formulated to be stricter and more lenient, respectively, than the first criteria set, in order to assess the influence of the criteria on the number of successful idle descents under both uncertainty parameter sets. In Table 6, the three criteria sets are formulated. The criteria are formulated explicitly for when idle descents are not allowed. For distances, the constraints hold for any point in time throughout the predicted nominal flight trajectory. The time difference at the IAF is the predicted time difference that follows from the predicted nominal flight trajectory. If an idle descent is not permitted, the aircraft must fly a fixed-FPA descent in the simulation. For completeness, the situation where no distance and time restrictions are applied is added to the table as set 0.

**Table 6 Criteria formulation of when idle descents are not allowed. The constraints hold throughout the flight.**

| Criteria Set | Hor. Dist. | Vert. Dist. | IAF $\Delta T$ |
|---|---|---|---|
| 0, zero | Unrestricted | Unrestricted | Unrestricted |
| 1, medium | $\leq$ 10 nm | $\leq$ 2000 ft | $\leq$ 90 sec |
| 2, strict | $\leq$ 15 nm | $\leq$ 2500 ft | $\leq$ 120 sec |
| 3, lenient | $\leq$ 7 nm | $\leq$ 1500 ft | $\leq$ 90 sec |

## B. Idle Descents under Criteria

In section V.B, it was explained how simulations and data processing were performed for all four reference scenarios, the four criteria sets, and the two uncertainty parameter sets. The results are presented here.

### *1. Successful Idle Descent Ratios*

For every unique combination, the number of successful idle descents was obtained and expressed as a ratio of the maximum number of theoretically possible idle descents. The maximum number theoretically possible is the number of descents flown when the reference scenario restrictions allow an idle descent to be flown. Therefore, this number is equal to the number of idle descents flown for criteria set 0, where no additional distance and time criteria are applied. An idle descent is marked as successful when no conflicts are predicted throughout the flight. The results are visualised in Figure 19.

Every sub-figure represents one of the four reference scenarios. For every criteria set, the results are shown per uncertainty parameter set. The bars indicate the number of successful idle descents as a ratio of the maximum number theoretically possible, as mentioned above. The green dots indicate the number of assigned idle descents for that criteria set as a ratio of the maximum number theoretically possible. The numbers written on the bar in the white boxes are the numbers of assigned idle descents. For criteria set 0, this is the maximum number theoretically possible, as explained above. The numbers in the boxes are related to the green dots, as the green dots express these numbers as ratios.

When the green dot and the bar share the same value, it means that all assigned idle descents were successful. It must be noted that the idle descents were assigned using the first uncertainty parameter set, as explained in section IV.C.3. Therefore, the number of assigned idle descents is the same for both uncertainty parameter sets. This allows for a sensitivity analysis investigating the effect of trajectory uncertainty on the number of successful idle descents. The findings from Figure 19 are discussed in detail in section VII.A.1.


**Figure 19 The number of successful and assigned idle descents expressed as ratios of the maximum theoretically possible number of idle descents, for each reference scenario, criteria set and uncertainty parameter set.**

*2. Successful Idle Descents throughout the Day*

In addition to analysing the number of successful idle descents in its totality, it is interesting to see how the number of successful idle descents varies throughout the day. This is shown in Figure 20. The total descents show the number of aircraft in the air at every hour. The number of successful idle descents per hour is then shown for each criteria set and uncertainty parameter set. The number of assigned idle descents is not displayed in this graph to prevent clutter, and showing it does not align with the intent of this graph.

From this graph, it becomes clear when the reference scenarios allow for idle descents, independent of the criteria set used. For FULLNIGHT, it can be seen that after 6:00 LT, no idle descents are allowed. The graph for OFF-PEAK clearly shows the peak hours that were identified as explained in section IV.C.1, using Figure 24 in section A.D. By comparing Figure 24 to the OFF-PEAK graph, it is clear that hours 7, 8, 12, 15, 18, and 19 are marked as peak hours, because in the radar data used for the simulations at least 65 aircraft were flying towards an IAF during those hours. In the simulations and thus in Figure 20, the total descent numbers are slightly different because here different descent types are flown compared to the conventional descents in the radar data, meaning that the time in the air is different for each aircraft. Additionally, this graph clearly shows which hours are busiest and what effects the criteria sets and uncertainty parameter sets have on the number of successful idle descents. This is most interesting for the OFF-PEAK and FREE scenarios.

This analysis is taken a step further for those scenarios by plotting the information from Figure 20 separately per IAF. This is presented in Figure 21 for the OFF-PEAK scenario and in Figure 22 for the FREE scenario. With these graphs, it is possible to identify traffic streams throughout the day towards each IAF. It can be observed that these vary strongly per IAF, indicating that it is important to consider this in the interpretation of the simulation results. The effects of the criteria sets and uncertainty parameter sets are clearly visible. This will be elaborated on in the discussion, in section VII.A.2.

## VII. Discussion

The main results from this research entail the successful idle descents under various reference scenarios, criteria sets, and uncertainty parameter sets. The findings from these results will now be discussed, using the figures introduced in section VI.B. In addition, limitations and potential are discussed. The discussion ends with recommendations for future work.


**Figure 20 The number of total descents and successful idle descents throughout the day for each reference scenario, criteria set and uncertainty parameter set.**

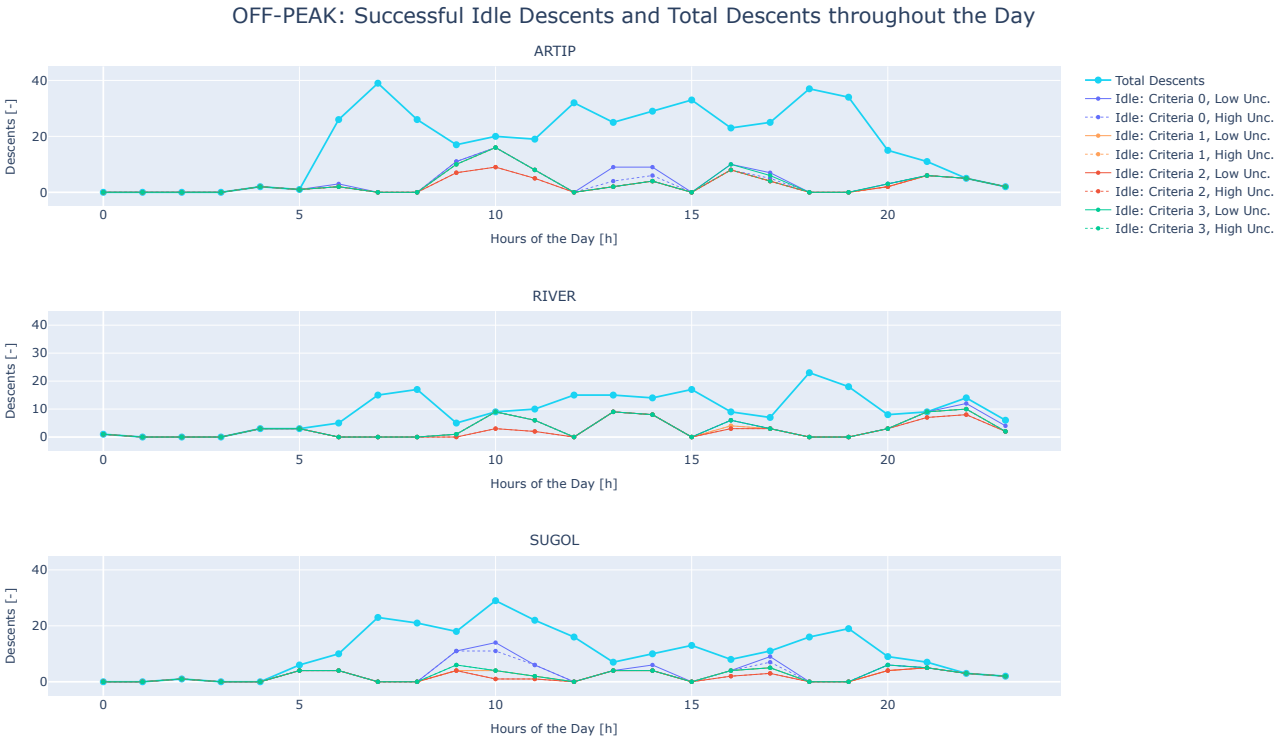


**Figure 21 The number of total descents and successful idle descents throughout the day for reference scenario OFF-PEAK, split up per IAF.**

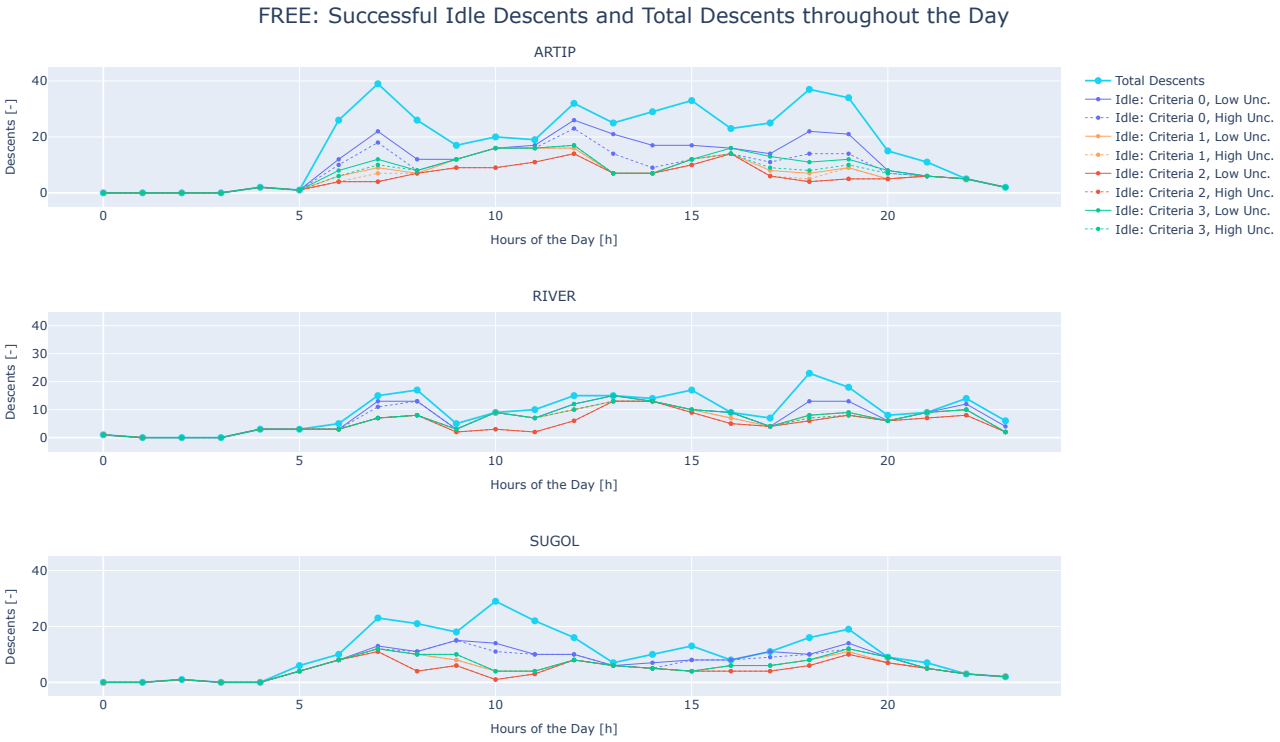


**Figure 22 The number of total descents and successful idle descents throughout the day for reference scenario FREE, split up per IAF.**

## A. Research Findings

### *1. Successful Idle Descent Ratios and Numbers*

From Figure 19, several interesting facts can be observed. For the MIDNIGHT scenario, only two aircraft were flying during the idle descent window, and both were able to complete an idle descent under all circumstances. For the FULLNIGHT scenario, 16 aircraft were flying during the idle descent window, of which 14 were able to complete an idle descent under all circumstances. In fact, apart from the two aircraft in conflict, all other aircraft were tens of nautical miles separated from each other. This suggests that allowing idle descents during the night is a safe measure with barely any increase in workload for ATC, as most aircraft are not even near each other.

For both the OFF-PEAK and FREE scenarios, it can be observed that, as expected, criteria set 0, with no restrictions, allows for the most successful idle descents. To reiterate, criteria set 3 contains the lenient restrictions for idle descents (H: $\leq$ 7 nm, V: $\leq$ 1500 ft and IAF $\Delta$T $\leq$ 90 sec), criteria set 1 the medium restrictions (H: $\leq$ 10 nm, V: $\leq$ 2000 ft and IAF $\Delta$T $\leq$ 90 sec) and criteria set 2 the strict restrictions (H: $\leq$ 15 nm, V: $\leq$ 2500 ft and IAF $\Delta$T $\leq$ 120 sec) respectively, as displayed in Table 6. It is therefore expected and confirmed from the graph that the order of most successful idle descents follows the order of criteria strictness.

Furthermore, doubling the trajectory uncertainty (by means of uncertainty parameter set 2, the high uncertainty set) has no influence on the number of successful idle descents flown under the strict criteria set. This criteria set is strict enough to allow for a great variety in trajectory uncertainty without causing extra workload for ATC to avoid idle-idle conflicts. For all other criteria sets, more idle descents are successful under lower uncertainty, which is to be expected. However, the difference between high and low uncertainty remained below 2% of all flights for all explicitly developed criteria (sets 1-3) and scenarios. The greatest difference is 12 flights, found for the FREE_3 scenario. This indicates that the developed criteria sets are not very sensitive to varying uncertainties. Thus, the spacing chosen is sufficient to ensure a safe execution of the idle descents, without drastically increasing the workload of ATC. When no criteria are applied (set 0), the differences are greater. The greatest difference is logically found for the FREE_0 scenario, which is 9% or 54 flights. For OFF-PEAK, the greatest difference is 7% or 17 flights. This indicates that the maximum number of possible idle descents is sensitive to trajectory uncertainty, which is to be expected.

The actual numbers of successful idle descents are significantly higher for the OFF-PEAK and FREE scenarios than for the night scenarios, which were considered realistic scenarios. It was found that at least 50% of all aircraft flying outside of peak hours can perform an idle descent successfully, regardless of the criteria and uncertainty parameter set used. This value goes up to 62% for the lenient criteria set (which is set 3). The zero set demonstrates the full potential independent of extra criteria, which is 76% for the low uncertainty parameter set.

For the FREE scenario, at least 40% of all aircraft can perform an idle descent successfully, regardless of the criteria and uncertainty parameter set used. This value goes up to 52% for the lenient criteria set, set 3. In numbers, the 40% corresponds to more than double the number of aircraft that make up the 50% for the OFF-PEAK scenario (244 aircraft versus 121 aircraft). This captures the great advantage of allowing idle descents during peak hours as well, as roughly double the amount of fuel can be saved. The full potential of successful idle descents throughout the day is almost 68%, or 419 aircraft for the low uncertainty parameter set.

The numbers found for the OFF-PEAK and FREE scenarios are much higher than for the night scenarios, demonstrating a high potential for fuel savings and emission reduction by assigning idle descents outside of night hours, and based on the descent criteria formulated in this research.

It should be noted that some conflicts in which an idle descent is involved are between an idle and a fixed-FPA descent instead of two idle descents. This means that this idle descent could, in theory, still be flown successfully when the aircraft on the fixed-FPA descent is given an instruction by ATC. Accounting for these situations also brings the numbers of assigned and successful idle descents even closer together.

### *2. Successful Idle Descents throughout the Day*

From Figure 20, it can be observed that the traffic flow is highly dynamic. The effects of different criteria sets on the number of successful idle descents are noticeable throughout the day. In general, the spread of successful idle descents between criteria sets is highest when the most total descents are flown, when looking at the FREE scenario. Clearly, the most idle descents are successfully flown under the zero criteria set and the least under the strict criteria set, as already observed from Figure 19 and mentioned above. Figure 20 clearly shows that many idle descents can be flown during peak hours, by comparing the OFF-PEAK and FREE graphs.

It is interesting to express the spread of successful idle descents between the criteria sets in numbers. During the night hours, between 80% and 100% of the total descents per hour are successful idle descents. The other off-peak hours are more dynamic. For the strict criteria set, between 15% and 73% of the total descents per hour are successful idle descents. This high variability is a result of the traffic flows being very dynamic throughout the day. For the zero criteria set, the ratios vary from 15% to 91%. The effect of the criteria sets on the number of successful idle descents is measured as the ratio increase from the strict set to the zero set for every hour. The highest increase from the strict to the zero set is 45% and occurs at hour 10. Thus, the effect of the criteria sets is the greatest here. The peak hours show a smaller variability. For the strict criteria set, between 21% and 44% of the total descents per hour are successful idle descents. This changes to a range from 42% to 76% for the zero criteria set. Here, the ratio increase from the strict to the zero set is more consistent. For most peak hours, the increase is between 30 and 40%.

The high ratios of successful idle descents during peak hours demonstrate the benefits of applying the criteria sets under the FREE scenario over the OFF-PEAK scenario. From Figure 19, it was already determined that more idle descents can be flown

during peak hours than during off-peak hours, for all formulated criteria sets.

Splitting the OFF-PEAK and FREE scenarios between the IAFs, as shown in Figure 21 and Figure 22, provides more insights. ARTIP is found to be the busiest IAF, as it has the highest total descents. As a result, the effect of the criteria sets on the number of successful idle descents is greatest there. This is especially noticeable for the FREE scenario. These graphs demonstrate how dynamic the traffic flows to the different IAFs are. It can be seen how the traffic density varies per IAF and per hour, underlining that the total traffic density is not necessarily a good indication of the traffic density per IAF. The graphs thus demonstrate the benefits of applying the criteria sets in a dynamic way, by assigning idle descents on a per-flight basis.

*3. Hypotheses Assessment*

Based on the findings discussed above, statements can be made about the hypotheses presented in section IV.A.3. Statistical tests are needed to formally accept or reject a hypothesis. However, not enough data are used in this research to perform statistical tests on, as only one day of traffic is simulated and two uncertainty parameter sets are used. However, the results of this research support or contradict the hypotheses. For the first hypothesis, stating an inverse relationship between the strictness of the reference scenario and the number of successful idle descents, strong evidence is found that supports this. The results clearly show that the most idle descents can be flown under the FREE scenario, which is the least strict. The stricter the reference scenario, the fewer idle descents can be flown.

The second hypothesis states an inverse relationship between the strictness of the descent criteria and the number of successful idle descents. The results partially support this hypothesis, showing that it is true under certain circumstances. In the OFF-PEAK and FREE scenarios, the least strict descent criteria indeed allow for the highest number of successful idle descents and vice versa. However, for the MIDNIGHT and FULLNIGHT scenarios, the aircraft spacing was so large that the difference in the criteria sets had no effect on the idle descent allocation. In the FULLNIGHT scenario, the only conflict encountered in criteria set 0 was filtered out by all three other criteria sets as the aircraft were very close together.

The third hypothesis states an inverse relationship between trajectory uncertainty and the number of successful idle descents. Again, this hypothesis is supported under certain circumstances. For various reference scenarios and criteria sets, the combination of the aircraft spacing and the strictness of the criteria sets led to trajectory uncertainty having no effect on the number of successful idle descents. For the MIDNIGHT and FULLNIGHT scenarios, this is solely because of aircraft spacing as discussed above. For the OFF-PEAK and FREE scenarios, it is a combination of both. For the least strict criteria sets, the zero set and the lenient set, the hypothesis is supported because lower uncertainty leads to a higher number of successful idle descents. This is because the criteria are within the range where an increase in uncertainty has an effect. In the other cases, the criteria sets are so strict that even with increased uncertainty, no extra conflicts are induced.

## B. Limitations from Assumptions

Naturally, the assumptions taken in this research and listed in section III.B and section IV.B affect the research outcome. For the identification of the trajectory uncertainty models, only wind uncertainty is considered. Possible model errors in the BlueSky simulation are neglected, as this simulator is widely accepted as a useful tool for real-world applications. Mass uncertainty is neglected under the assumption that ATS B2 ADS-C EPP data are available and can be downlinked. Aircraft intent and flight control inaccuracy are neglected, as their effects are considered small when flying on autopilot and highly complex to model accurately. The FMS is required to have knowledge of a high-resolution wind field grid, which is in reality not the case yet. However, this is expected to be possible in the future. Cross-track errors are neglected because of the current RNP capabilities of aircraft. Trajectory uncertainty is expected to be higher when these factors are all accounted for, but a sensitivity analysis using two uncertainty parameter sets was designed to account for this.

The greatest effect on the research outcome follows from several other assumptions. Firstly, every aircraft flies to FL100 at the IAF, whereas in reality, any altitude between FL70 and FL100 is allowed. This assumption takes away opportunities for successful idle descents, which would have been there if altitude spacing at the IAF had been possible. In addition, no ATC intervention is considered, and fixed speed schedules based on RECAT categories are used. Because of this, possibilities for more successful idle descents by means of speed changes or different speed schedules are excluded. These assumptions result in the research outcome presenting a lower bound for idle descent possibilities. With these assumptions lifted, even more idle descents would be possible for multiple reference scenarios and criteria sets.

Lastly, only one descent type is considered per aircraft. Because of this, only fully completed idle descents are marked as successful. In reality, an idle descent can be completed partially and then stopped by introducing a level segment or switching to a fixed-FPA descent in order to avoid a conflict. This way, the total time of idle descents flown increases, resulting in higher fuel savings and reduced emissions.

These limitations show that the numbers found in this research should be viewed as conservative, since they can be increased by introducing the discussed additional complexities.

## C. Operational Potential

This research serves as a foundation for implementing more idle descents in daily operations in the future. A clear view on what this implementation would look like in the operation is sketched now. The uplinking of weather information to the FMS and the downlinking of ATS B2 ADS-C EPP data are needed to ensure low trajectory uncertainty, ensuring more idle descents can be flown safely. While an aircraft is in cruise and has appeared on the ACC radar, a trajectory predictor (TP) predicts this aircraft's path in case an idle descent is initiated for a certain speed schedule. The same is done for all other aircraft on the radar and flying towards the same IAF. Then, trajectory uncer-

tainty is added to these nominal flight paths, and conflict probabilities are calculated between each aircraft pair. All aircraft that adhere to the criteria of the chosen criteria set are assigned idle descents. If desired, from each aircraft pair in conflict, one aircraft could still be assigned an idle descent while the other is given a conventional descent with ATC intervention. To increase complexity, aircraft of conflict pairs can be granted permission to fly a partial idle descent for the part where no conflicts are predicted. In order to execute the above safely, information sharing between various ANSPs is vital. Depending on the cruise altitude, an idle descent permission is granted by either UAC or ACC, meaning that EUROCONTROL and LVNL are both involved. When handing over an aircraft, this information must be transferred. Airspace capacity and flow management, as provided by EUROCONTROL, must also be considered.

### D. Recommendations for Future Work

As stated above, no statistical tests can be performed to accept or reject the hypotheses, due to insufficient data being used for this. In this research, only one day of traffic is simulated. Therefore, the first recommendation is to repeat the analysis for multiple days of traffic, where different traffic distributions are encountered, to see if the trends discovered in this research still hold. In addition, it is recommended to expand the analysis with more uncertainty parameter sets, to more accurately quantify the effect of trajectory uncertainty on the number of successful idle descents.

In order to achieve the operational potential described in the section above, it is recommended to research several aspects. Firstly, it is important to remember that the trajectories are determined using only wind uncertainty in the trajectory simulations. For this assumption to be correct, it is important that accurate weather information is uplinked to the aircraft and ADS-C EPP data is downlinked to the ground. In case this is not possible, further research is needed to quantify uncertainty by accounting for other uncertainty sources that are now assumed to be small.

Next to this, successful idle descents can be investigated when altitude spacing at the IAF is included. Furthermore, the effect of ATC intervention and different speed schedules can be researched. In addition, the possibility and effects of assigning partial idle descents can be investigated. Also, an analysis can be conducted that quantifies the benefits of flying idle descents throughout the day in terms of fuel usage and emissions. This is vital for creating a business case to actually implement idle descents based on per-flight criteria in daily operations.

After everything mentioned above has been researched, a framework can be set up that allows for assigning idle descents throughout the day in daily operations. The trajectory prediction simulations performed in BlueSky for this research take several seconds or minutes per aircraft. Adding trajectory uncertainty to the predicted path and calculating subsequent conflict probabilities also takes several minutes per aircraft. This is not feasible for real-time operations. A framework is needed in which all these calculations can be done in the order of seconds, to ensure feasibility for real-time operations.

## VIII. Conclusion

Information on when idle descents can be flown throughout a 24-hour operation based on per-flight criteria cannot be found in the literature. Therefore, the aim of this research was to develop per-flight criteria for the application of idle and fixed-FPA descents towards the IAF and to analyse the resulting numbers of successfully flown idle descents, thereby taking into account associated trajectory uncertainties. Trajectory uncertainty models for along-track and vertical motion for both idle and fixed-FPA descents were obtained using aircraft simulations under various wind conditions. These models were used to calculate conflict probabilities between aircraft flying towards the same IAF. Four reference scenarios with time restrictions on the application of idle descents were constructed. Three descent criteria sets were developed based on the idle descent conflicts encountered without imposed criteria. The number of successful idle descents was evaluated for all four reference scenarios, four criteria sets, and two trajectory uncertainty parameter sets.

This research produced various results. An inverse relationship between the strictness of the reference scenario and the number of successful idle descents was found. In addition, an inverse relationship between the strictness of the criteria set and the number of successful idle descents was found for scenarios where aircraft pairs were found to be separated within the range of the criteria sets. Outside this range, no effect of the strictness of the criteria set on the number of successful idle descents was observed. Furthermore, an inverse relationship between trajectory uncertainty and the number of successful idle descents was found for some reference scenarios and criteria sets. To observe this relationship, aircraft spacing was again required to be in the range of the criteria sets. Furthermore, some criteria sets were strict enough to conceal this inverse relationship and make trajectory uncertainty have no effect on the number of successful idle descents.

In fact, the difference between high and low uncertainty remained below 2% of all flights for all explicitly developed criteria (sets 1-3) and scenarios. The greatest difference in these sets was found to be 12 flights, for the FREE_3 scenario. The total greatest difference is 9% or 54 flights, logically found for the FREE_0 scenario. These numbers demonstrate that, even though the inverse relationship with trajectory uncertainty exists, the effects under developed criteria are small.

Furthermore, it was found that between 50% and 62% of all aircraft descending outside of peak hours can complete an idle descent successfully, depending on the criteria set and uncertainty used. This goes up to 76% when criteria set 0 (no extra criteria) and low uncertainty are used, meaning this is the theoretical upper bound. The lower bound of 50% corresponds to 121 successful idle descents. When looking at all descending aircraft throughout the day, between 40% and 52% can complete an idle descent successfully, with a maximum potential of 68%. The lower bound of 40% here corresponds to 244 successful idle descents, which is more than double the number obtained for the off-peak hours. Both numbers are significantly higher than for the night scenarios, due to considerably fewer aircraft flying idle.

In addition, the variability of the number of successful idle

descents per hour throughout the day was expressed using ratios of the total descents per hour. This was done by comparing the strict criteria set to the zero set, where no developed criteria were applied. The highest variability was found for the off-peak hours, with night hours excluded. For the strict set, between 15% and 73% of the total descents per hour are successful idle descents for those off-peak hours. The greatest effect of the criteria sets was measured for hour 10, where the difference in successful idle descents between the strict set and the zero set was 45%. During peak hours, between 21% and 44% of the total descents per hour are successful idle descents for the strict set. Here, the ratio increase from the strict to the zero set is more consistent. For most peak hours, the increase is between 30 and 40%. The high variability indicated by these numbers underlines the dynamic flow of traffic throughout the day. Splitting the hourly descents per IAF further demonstrates the benefits of applying criteria on a per-flight basis. The effect of the different criteria sets varies per IAF due to the different traffic densities, and is most noticeable during peak hours.

Recommendations are made to allow the hypotheses stated in this research to be formally accepted or rejected. Firstly, it is recommended to repeat the analysis for multiple days of traffic with different traffic distributions. Additionally, it is recommended to expand the analysis with more uncertainty parameter sets, to more accurately capture the effect of trajectory uncertainty on the number of successful idle descents.

To prepare this concept for daily operations, several aspects should be researched. It is important to uplink accurate weather information and downlink ADS-C EPP data, so that wind uncertainty is the only main contributor to trajectory uncertainty. Further research is needed to quantify uncertainty by accounting for other uncertainty sources that are now assumed to be small, in case this is not possible. The possibility of altitude spacing at the IAF could be introduced in the model. ATC intervention and different speed schedules could be introduced, and their effects on the number of successful idle descents are to be investigated. Also, the effect of assigning partial idle descents instead of only full idle descents can be investigated. An analysis quantifying the benefits of idle descents throughout the day in terms of fuel usage and emissions has to be carried out. Afterwards, a framework should be set up that allows for calculating predicted trajectories, trajectory uncertainty, and conflict probabilities in the order of seconds, to allow for real-time operations. The research presented in this paper serves as a foundation for assigning idle descents on a per-flight basis throughout the day in daily operations. It demonstrates the possibilities for greatly increasing the number of idle descents flown throughout the day by allowing idle descents outside of night hours.

## References


[1] SESAR Joint Undertaking, "European ATM Master Plan, 2025 Edition," `https://www.sesarju.eu/MasterPlan2025_SupportingDocuments`, 2025. Accessed: 22-04-2025.

[2] Tielrooij, M., Kok, R., de Jong, T., Dijkstra, F., Dufourmont, T., Lap, E., Okina, A., and Vos, R., "Transition to Trajectory Based Operations (TBO)," *KDC/2021/0062*, 2022.

[3] ICAO, *Continuous Descent Operations (CDO) Manual (Doc 9931)*, International Civil Aviation Organization, Montreal, Quebec, Canada, 2010.

[4] Wubben, F., and Busink, J., "Environmental benefits of continuous descent approaches at Schiphol Airport compared with conventional approach procedures," *NLR-TP-2000-275*, 2000.

[5] Clarke, J.-P., Brown, J., Elmer, K., Ho, N., Ren, L., Tong, K.-O., and Wat, J., "Continuous Descent Approach: Design and Flight Test for Louisville International Airport," *Journal of Aircraft*, Vol. 41, 2004, pp. 1054–1066. https://doi.org/10.2514/1.5572.

[6] Tong, K.-O., Schoemig, E. G., Boyle, D. A., Scharl, J., and Haraldsdottir, A., "Descent Profile Options for Continuous Descent Arrival Procedures within 3D Path Concept," *2007 IEEE/AIAA 26th Digital Avionics Systems Conference*, 2007, pp. 3.A.3–1–3.A.3–11. https://doi.org/10.1109/DASC.2007.4391872.

[7] Aksoy, H., Turgut, E. T., and Usanmaz, ., "The design and analysis of optimal descent profiles using real flight data," *Transportation Research Part D: Transport and Environment*, Vol. 100, 2021, p. 103028. https://doi.org/10.1016/j.trd.2021.103028.

[8] Pradeep, P., and Wei, P., "Predictability, Variability and Operational Feasibility Aspect of CDA," *2017 IEEE Aerospace Conference*, 2017, pp. 1–14. https://doi.org/10.1109/AERO.2017.7943728.

[9] Stell, L., "Predictability of Top of Descent Location for Operational Idle-Thrust Descents," *10th AIAA Aviation Technology, Integration, and Operations (ATIO) Conference*, 2010. https://doi.org/10.2514/6.2010-9116.

[10] Wat, J., Follet, J., Mead, R., Brown, J., Kok, R., Dijkstra, F., and Vermeij, J., "In Service Demonstration of Advanced Arrival Techniques at Schiphol Airport," *6th AIAA Aviation Technology, Integration and Operations Conference (ATIO)*, 2006. https://doi.org/10.2514/6.2006-7753.

[11] Itoh, E., Wickramasinghe, N. K., Hirabayashi, H., Uejima, K., and Fukushima, S., "Analyzing Feasibility of Continuous Descent Operation Following Fixed-Flight Path Angle from Oceanic Route to Tokyo International Airport," *AIAA Modeling and Simulation Technologies Conference*, 2016. https://doi.org/10.2514/6.2016-0168.

[12] Itoh, E., Wickramasinghe, N. K., Hirabayashi, H., and Fukushima, S., "Feasibility study on fixed flight-path angle descent for wide-body passenger aircraft," *CEAS Aeronautical Journal*, Vol. 10, No. 2, 2018, p. 589–612. https://doi.org/10.1007/s13272-018-0337-9.

[13] Toratani, D., Wickramasinghe, N. K., Westphal, J., and Feuerle, T., "Feasibility study on applying continuous descent operations in congested airspace with speed control functionality: Fixed flight-path angle descent," *Aerospace Science and Technology*, Vol. 107, 2020, p. 106236. https://doi.org/10.1016/j.ast.2020.106236.

[14] Iwata, D., Nonaka, Y., Funai, Y., Shindo, T., Tanaka, S., Sato, M., and Itoh, E., "Demonstration of Fixed Flight-Path Angle Descent via Scheduled Commercial Flights," *Journal of Air Transportation*, 2024, p. 1–16. https://doi.org/10.2514/1.d0400.

[15] Sopjes, R., Jong, P. d., Borst, C., Paassen, M. M. v., and Mulder, M., "Continuous Descent Approaches with Variable Flight-Path Angles under Time Constraints," *AIAA Guidance, Navigation, and Control Conference*, 2011. https://doi.org/10.2514/6.2011-6219.

[16] Warren, A., "Trajectory Prediction Concepts for Next Generation Air Traffic Management," *3rd USA/Europe ATM R&D Seminar*, Citeseer, 2000, p. 171.

[17] Weitz, P., "Determination and Visualization of Uncertainties in 4D-Trajectory Prediction," *2013 Integrated Communications, Navigation and Surveillance Conference (ICNS)*, 2013, pp. 1–9. https://doi.org/10.1109/ICNSurv.2013.6548525.

[18] Torres, S., "Trajectory Accuracy Sensitivity to Modeling Factors," *15th AIAA Aviation Technology, Integration, and Operations Conference*, 2015. https://doi.org/10.2514/6.2015-2599.

[19] Casado Magaña, E. J., "Trajectory prediction uncertainty modelling for Air Traffic Management," Ph.D. thesis, University of Glasgow, 2016.

[20] Mondoloni, S., and Bayraktutar, I., "Impact of Factors, Conditions and Metrics on Trajectory Prediction Accuracy," *Proceedings of the 6th USA/Europe Air Traffic Management Research and Development Seminar, ATM 2005*, 2005, p. 305 – 314.

[21] Sankararaman, S., and Daigle, M., "Uncertainty Quantification in Trajectory Prediction for Aircraft Operations," *AIAA Guidance, Navigation, and Control Conference*, 2017. https://doi.org/10.2514/6.2017-1724.

[22] Bronsvoort, J., McDonald, G., Torres, S., Paglione, M., Young, C., Hochwarth, J., Boucquey, J., and Vilaplana, M., "Use of the Extended Projected Profile (EPP) in Trajectory Management," *16th American Institute of Aeronautics and Astronautics (AIAA) Aviation Technology, Integration, and Operations Conference*, 2016.

[23] EUROCONTROL, "Automatic Dependent Surveillance Contract (ATS-B2)," https://www.eurocontrol.int/service/automatic-dependent-surveillance-contract-ats-b2, 2025. Accessed: 02-04-2025.

[24] Chaloulos, G., and Lygeros, J., "Effect of Wind Correlation on Aircraft Conflict Probability," *Journal of Guidance, Control, and Dynamics*, Vol. 30, No. 6, 2007, p. 1742–1752. https://doi.org/10.2514/1.28858.

[25] Bronsvoort, J., McDonald, G., Potts, R., and Gutt, E., "Enhanced Descent Wind Forecast for Aircraft," *Proceedings of the Ninth USA/Europe Air Traffic Management Research and Development Seminar (ATM2011)*, 2011.

[26] ICAO, "TBO Concept: version Appendix A to WP-652 - TBOCD 3.0," https://www.sesarju.eu/sites/default/files/documents/reports/Appendix_A_to_WP652_TBOCD_3.0.pdf, 2015. Accessed: 01-04-2025.

[27] Lee, A., Weygandt, S., Schwartz, B. E., and Murphy, J. R., "Performance of Trajectory Models with Wind Uncertainty," *AIAA Modeling and Simulation Technologies Conference*, 2009. https://doi.org/10.2514/6.2009-5834.

[28] Zheng, Q., and Zhao, Y., "Modeling Wind Uncertainties for Stochastic Trajectory Synthesis," *11th AIAA Aviation Technology, Integration, and Operations (ATIO) Conference*, 2011. https://doi.org/10.2514/6.2011-6858.

[29] Hernández-Romero, E., Valenzuela, A., and Rivas, D., "Probabilistic multi-aircraft conflict detection and resolution considering wind forecast uncertainty," *Aerospace Science and Technology*, Vol. 105, 2020, p. 105973. https://doi.org/10.1016/j.ast.2020.105973.

[30] Seyedipour, S., Nobahari, H., and Prandini, M., "A probabilistic approach to mid-term conflict detection with accuracy estimate," *Journal of the Franklin Institute*, Vol. 359, No. 16, 2022, p. 9193–9219. https://doi.org/10.1016/j.jfranklin.2022.08.055.

[31] Hu, J., Prandini, M., and Sastry, S., "Aircraft Conflict Prediction in the Presence of a Spatially Correlated Wind Field," *IEEE Transactions on Intelligent Transportation Systems*, Vol. 6, No. 3, 2005, pp. 326–340. https://doi.org/10.1109/TITS.2005.853699.

[32] Hu, J., Prandini, M., and Sastry, S., "Aircraft Conflict Detection in Presence of Spatially Correlated Wind Perturbations," *AIAA Guidance, Navigation, and Control Conference and Exhibit*, 2003. https://doi.org/10.2514/6.2003-5339.

[33] Prandini, M., Hu, J., Lygeros, J., and Sastry, S., "A Probabilistic Approach to Aircraft Conflict Detection," *IEEE Transactions on intelligent transportation systems*, Vol. 1, No. 4, 2000, pp. 199–220. https://doi.org/10.1109/6979.898224.

[34] Yang, L. C., and Kuchar, J. K., "Using Intent Information in Probabilistic Conflict Analysis," *Guidance, Navigation, and Control Conference and Exhibit*, 1998, p. 797–806. https://doi.org/10.2514/6.1998-4237.

[35] Lecchini Visintini, A., Glover, W., Lygeros, J., and Maciejowski, J., "Monte Carlo Optimization for Conflict Resolution in Air Traffic Control," *IEEE Transactions on Intelligent Transportation Systems*, Vol. 7, No. 4, 2006, pp. 470–482. https://doi.org/10.1109/TITS.2006.883108.

[36] Li, G., Zhai, S., and Jia, Q., *Conflict Detection and Resolution Based on Four-Dimensional Trajectory*, Springer Nature Singapore, 2024, pp. 149–188. https://doi.org/10.1007/978-981-97-5300-0_6.

[37] Wickramasinghe, N. K., Toratani, D., Itoh, E., Westphal, J., Schoniger, H., Feuerle, T., and Stanisak, M., "Experimental Approach for Efficient Arrival Procedures with Fixed-Flight Path Angle Descent," *2019 Integrated Communications, Navigation and Surveillance Conference (ICNS)*, 2019, pp. 1–14. https://doi.org/10.1109/ICNSURV.2019.8735118.

[38] Turgut, E. T., Usanmaz, O., Cavcar, M., Dogeroglu, T., and Armutlu, K., "Effects of Descent Flight-Path Angle on Fuel Consumption of Commercial Aircraft," *Journal of Aircraft*, Vol. 56, No. 1, 2019, p. 313–323. https://doi.org/10.2514/1.c033911.

# A. Appendix

## A. Aircraft Data for Trajectory Uncertainty Simulations

**Table 7 Aircraft data used in the trajectory uncertainty simulations.**

| ID | Type | Route | Cruise Alt. | Cruise Spd. | Descent Spd. | Descent Type |
|---|---|---|---|---|---|---|
| LB001 | E190 | ROBEG-NORKU-ARTIP | FL350 | 0.74 M | 250 KCAS | Idle |
| LB002 | E190 | ROBEG-NORKU-ARTIP | FL350 | 0.74 M | 250 KCAS | Fixed-FPA |
| LB003 | E190 | LESDO-HELEN-RIVER | FL350 | 0.74 M | 250 KCAS | Idle |
| LB004 | E190 | LESDO-HELEN-RIVER | FL350 | 0.74 M | 250 KCAS | Fixed-FPA |
| LB005 | E190 | SUPEL-MOLIX-SUGOL | FL350 | 0.74 M | 250 KCAS | Idle |
| LB006 | E190 | SUPEL-MOLIX-SUGOL | FL350 | 0.74 M | 250 KCAS | Fixed-FPA |
| LB007 | B738 | ROBEG-NORKU-ARTIP | FL370 | 0.78 M | 280 KCAS | Idle |
| LB008 | B738 | ROBEG-NORKU-ARTIP | FL370 | 0.78 M | 280 KCAS | Fixed-FPA |
| LB009 | B738 | LESDO-HELEN-RIVER | FL370 | 0.78 M | 280 KCAS | Idle |
| LB010 | B738 | LESDO-HELEN-RIVER | FL370 | 0.78 M | 280 KCAS | Fixed-FPA |
| LB011 | B738 | SUPEL-MOLIX-SUGOL | FL370 | 0.78 M | 280 KCAS | Idle |
| LB012 | B738 | SUPEL-MOLIX-SUGOL | FL370 | 0.78 M | 280 KCAS | Fixed-FPA |
| LB013 | B788 | ROBEG-NORKU-ARTIP | FL390 | 0.84 M | 310 KCAS | Idle |
| LB014 | B788 | ROBEG-NORKU-ARTIP | FL390 | 0.84 M | 310 KCAS | Fixed-FPA |
| LB015 | B788 | LESDO-HELEN-RIVER | FL390 | 0.84 M | 310 KCAS | Idle |
| LB016 | B788 | LESDO-HELEN-RIVER | FL390 | 0.84 M | 310 KCAS | Fixed-FPA |
| LB017 | B788 | SUPEL-MOLIX-SUGOL | FL390 | 0.84 M | 310 KCAS | Idle |
| LB018 | B788 | SUPEL-MOLIX-SUGOL | FL390 | 0.84 M | 310 KCAS | Fixed-FPA |

## B. Descent Criteria Simulations

**Table 8 Overview of the 16 BlueSky simulations with different reference scenarios and criteria sets.**

| Criteria / Ref. Scn | Set 0 (Zero) | Set 1 (Medium) | Set 2 (Strict) | Set 3 (Lenient) |
|---|---|---|---|---|
| **MIDNIGHT** | MIDNIGHT_0 | MIDNIGHT_1 | MIDNIGHT_2 | MIDNIGHT_3 |
| **FULLNIGHT** | FULLNIGHT_0 | FULLNIGHT_1 | FULLNIGHT_2 | FULLNIGHT_3 |
| **OFF-PEAK** | OFF-PEAK_0 | OFF-PEAK_1 | OFF-PEAK_2 | OFF-PEAK_3 |
| **FREE** | FREE_0 | FREE_1 | FREE_2 | FREE_3 |

### C. Trajectory Uncertainty in Cruise

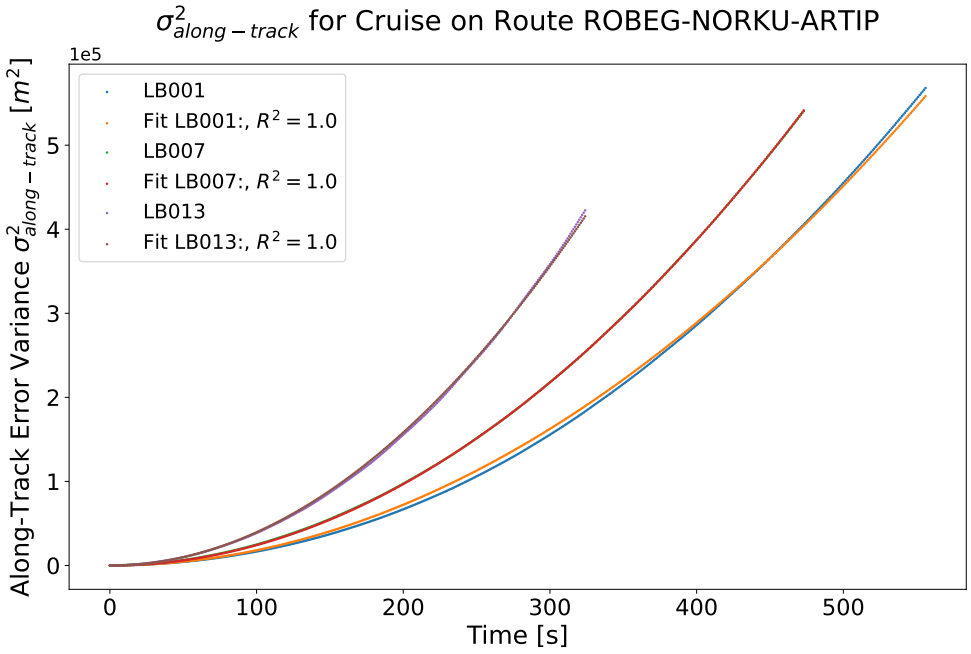


**Figure 23 Along-track error variance for cruise with quadratic curve fit.**

### D. Peak Hours from Radar Data

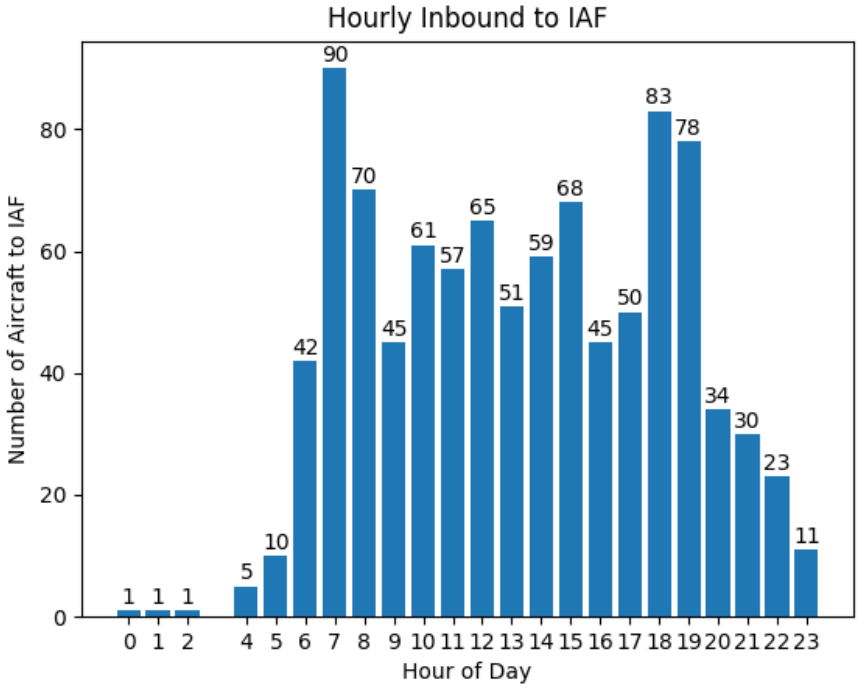


**Figure 24 Hourly traffic towards an IAF, used to identify peak hours.**

## E. Descent Data

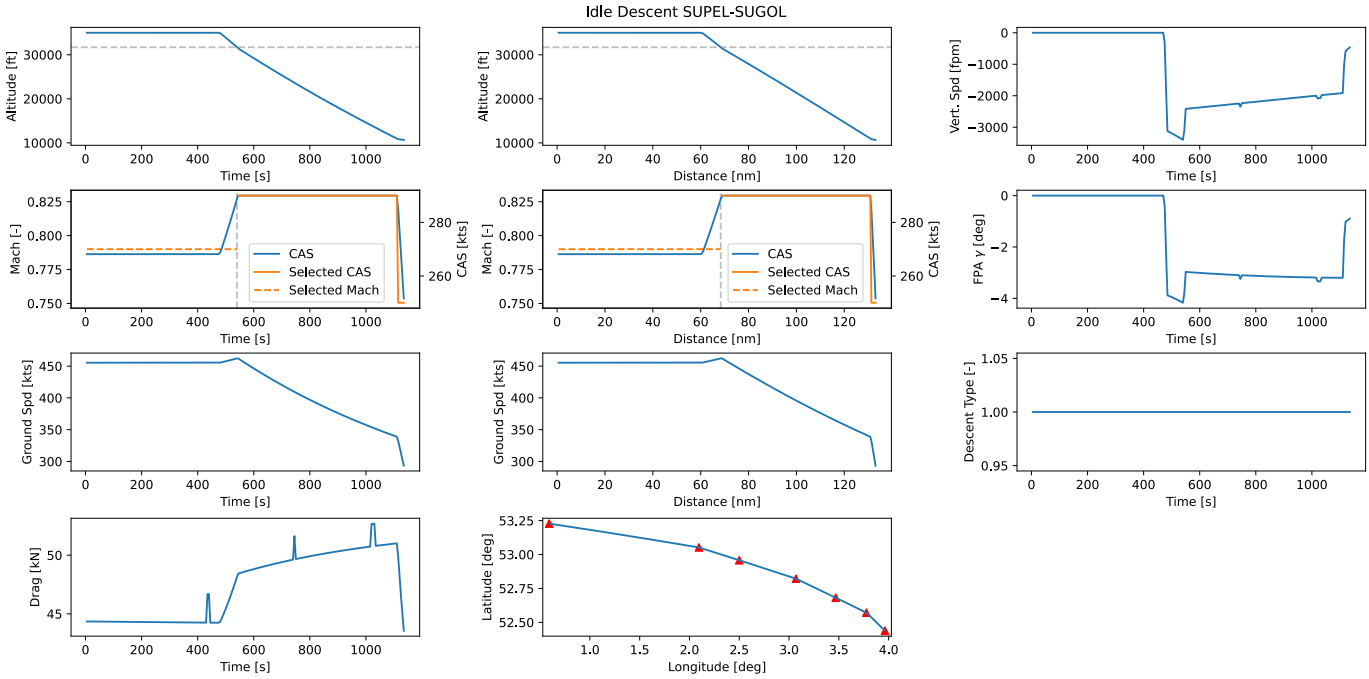


**Figure 25 Data overview for an idle descent from SUPEL to SUGOL, with the crossover altitude marked by grey dashed lines.**

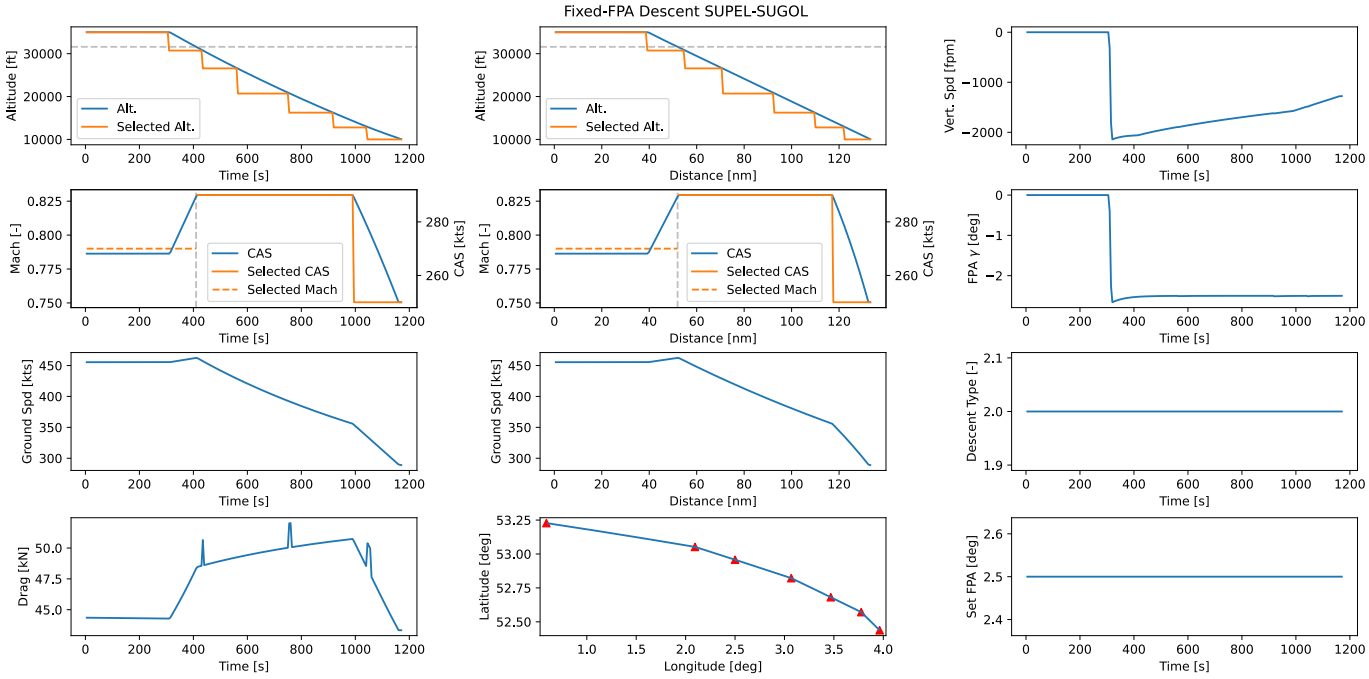


**Figure 26 Data overview for a fixed-FPA descent from SUPEL to SUGOL, with the crossover altitude marked by grey dashed lines.**

# Part B

## Verification

# 1

# Verification Methods

Verification of the implemented simulations and data processing code is highly important to ensure the credibility of the results obtained in this research. For this, various verification methods have been applied. These will be discussed here.

Next to verification, validation is important to ensure the models resemble reality. Validation of the identified trajectory uncertainty models and the number of idle descents under the developed descent application criteria is not possible within this thesis research. It would involve multiple real aircraft flying idle descents towards the IAFs of Schiphol Airport to replicate the simulations. In addition, access to these data would be required. Unfortunately, for this research it is not possible to achieve that. Furthermore, it must be noted that the verification and validation of the existing version of the BlueSky simulator were outside the scope of this research. The BlueSky simulator is widely used and assumed to be suitable for this research.

To start with, assumptions taken in this research were verified by consulting literature and assessing the effects on the research outcomes. Regulations were consulted to ensure the research takes place in a realistic context. Examples of this are the aircraft separation minima and RECAT classifications.

It is important to verify all core computations by means of unit tests. Throughout this research, all calculations were subjected to unit tests to verify the correctness of the calculation implementations. This includes the calculations added to the BlueSky simulator autopilot files. Afterwards, the calculations were expanded to automate the calculations and apply them to multiple cases simultaneously. When appropriate, outcomes were saved into CSV files and manually recalculated to make sure the outcomes matched.

Additionally, graphs were constructed to visually verify certain parameters. Fixed-FPA descent data graphs were constructed to assess the newly added fixed-FPA descent implementation into the BlueSky autopilot. It was checked whether key flight parameters had sensible values. Next to this, conflict probabilities calculated for each aircraft pair were shown along with the nominal distances between the aircraft. These were compared to the Protective Zone (PZ) to assess whether the probabilities were sensible in all situations.

The number of successful idle descents was verified by calculating it using different methods. Counters were added to the processing code to count the descents while processing the data. Afterwards, the data were extracted from the CSV files they were saved to, and the number of successful idle descents was recalculated using the raw data. Both outcomes from these methods were compared, and matching values ensured correct calculations.

The most complicated task in this context is to verify whether the large simulations are set up correctly. In addition, it is important to fully comprehend the data generated from the simulations and from the subsequent processing steps. The most intuitive way to verify whether all this has been done correctly, is through visualisation. Because of this, a custom interactive dashboard was developed during this research. This dashboard allows for full comprehension of the simulations and resulting conflicts encountered, thereby providing a clear view on the correctness of the implementations. This dashboard is presented and elaborated on in chapter 2. Part of this dashboard evolved from a similar dashboard created to visualise the radar data used to set up the simulations. That dashboard is not elaborated on due to the similarities, but it was of vital importance to verify all filtering steps taken on the radar data in order to generate the simulation spawn points for all aircraft.

# 2

# Interactive Dashboard for Data Visualisation

As mentioned in chapter 1, the interactive dashboard showing the simulations and corresponding conflicts is presented in this chapter. This dashboard is the main tool for visually verifying the simulation data and the conflict probabilities between any aircraft pair, to obtain a thorough understanding of the simulation results and the conflict scenarios encountered.

At start-up, a time slider and a world map are shown. All other fields are still empty. Via the time slider, any time throughout a full 24-hour day can be selected with a resolution of 2 minutes. On the map, a snapshot of the simulation at that time is displayed. The three IAFs are shown as black crosses on the map. Every dot represents an aircraft. The aircraft are distinguished by colour based on to which IAF they are flying, to clearly show the traffic streams towards each IAF. By changing the selected time in steps of 2 minutes, the BlueSky simulation can be replayed. The view is shown in Figure 2.1.

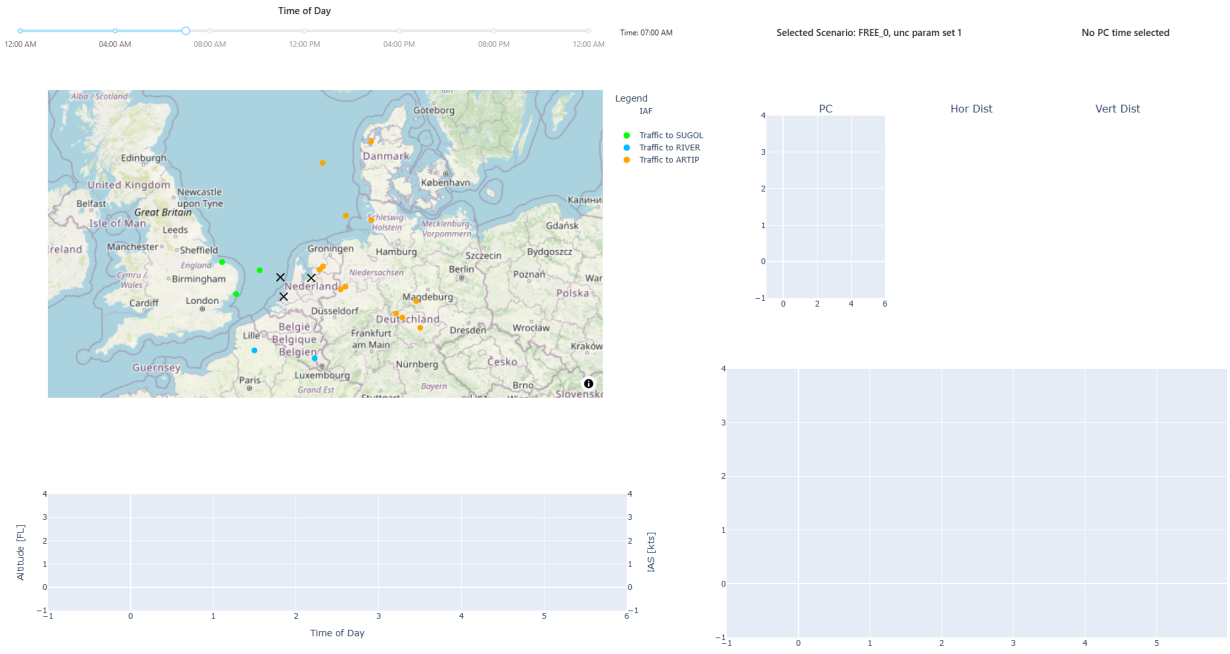


**Figure 2.1:** Snapshot of the dashboard at start-up for a selected time, using one of the simulation configurations.

At the top, the selected scenario is displayed. In this case, the FREE reference scenario using criteria set 0 is loaded. The first trajectory uncertainty parameter set is used to calculate the conflict probabilities, as shown later.

By clicking on an aircraft, its dot turns red and its route is displayed. The waypoints making up the route are shown as black triangles. Its altitude and speed graphs are shown below the map. The current position is indicated on these graphs by annotations. By clicking on a second aircraft, its route and its altitude and speed information appear as well. For demonstration purposes, an example is chosen where two aircraft from two different routes are meeting around the IAF. This is depicted in Figure 2.2.

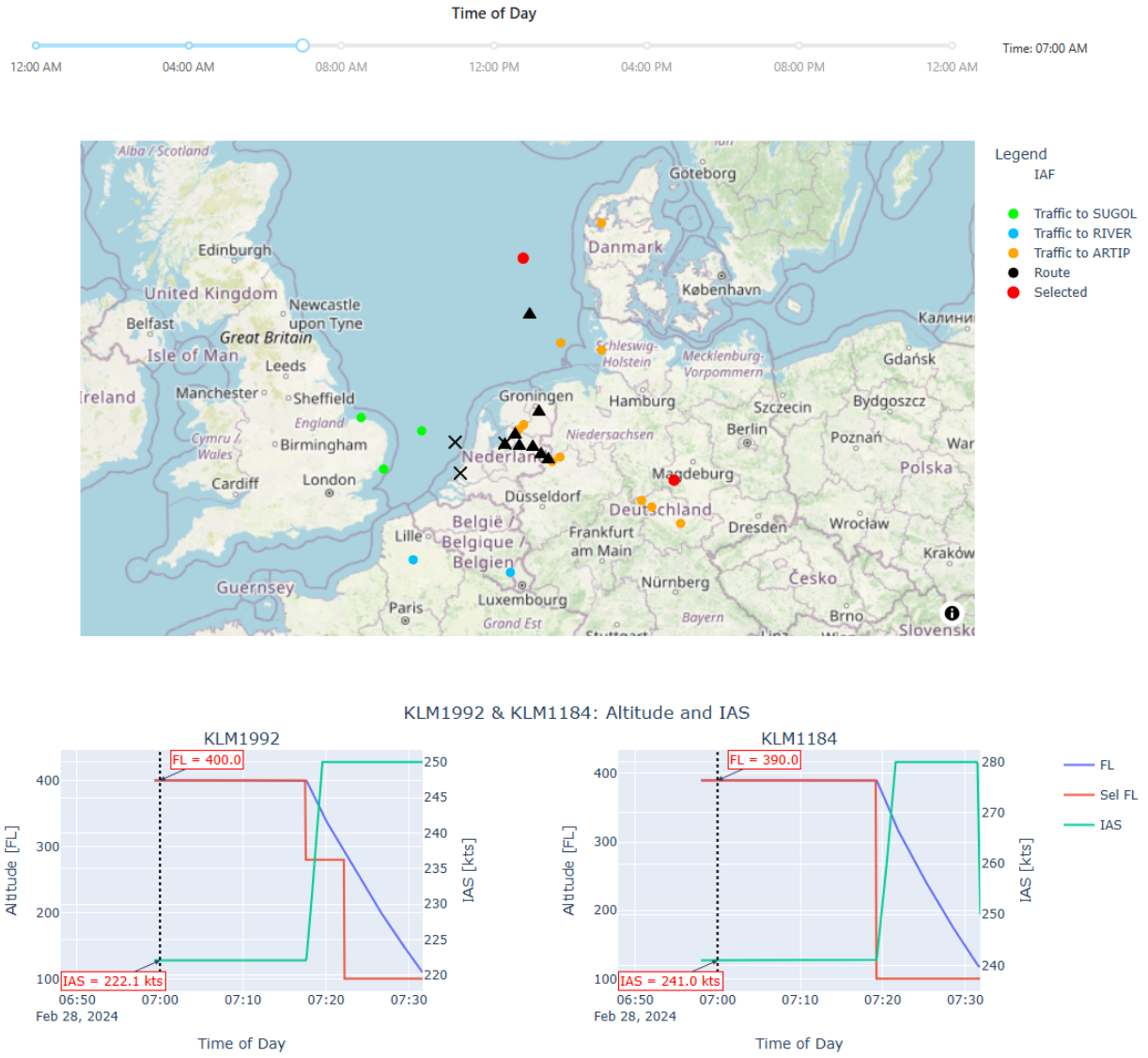


**Figure 2.2:** Altitude and speed graphs for two selected aircraft.

When two aircraft are selected, the trajectory uncertainties for the lookahead until the IAF are calculated, and the resulting conflict probabilities are computed. The conflict probabilities and nominal distances are plotted over time in separate graphs. In Figure 2.3, this is shown for the same aircraft selected in Figure 2.2. Clicking on any value of the conflict probability graph generates the corresponding uncertainty ellipsoid in the graph below. This ellipsoid shows the positional difference of the two aircraft for the selected lookahead time, based on the trajectory uncertainties with a 95% confidence interval. The selected lookahead time is displayed in the top right corner of the dashboard. In Figure 2.3, the conflict probability clicked on is 0. Hence, the uncertainty ellipsoid is fully green. It can be seen that, even though the vertical distance has a possibility of dropping below $1000$ ft, the horizontal distance is not even close to $5$ nm. The nominal aircraft positions for the selected aircraft on the selected lookahead time are displayed in purple on the map. Additionally, the altitude and speed at the lookahead time are annotated in blue in the altitude and speed graphs.

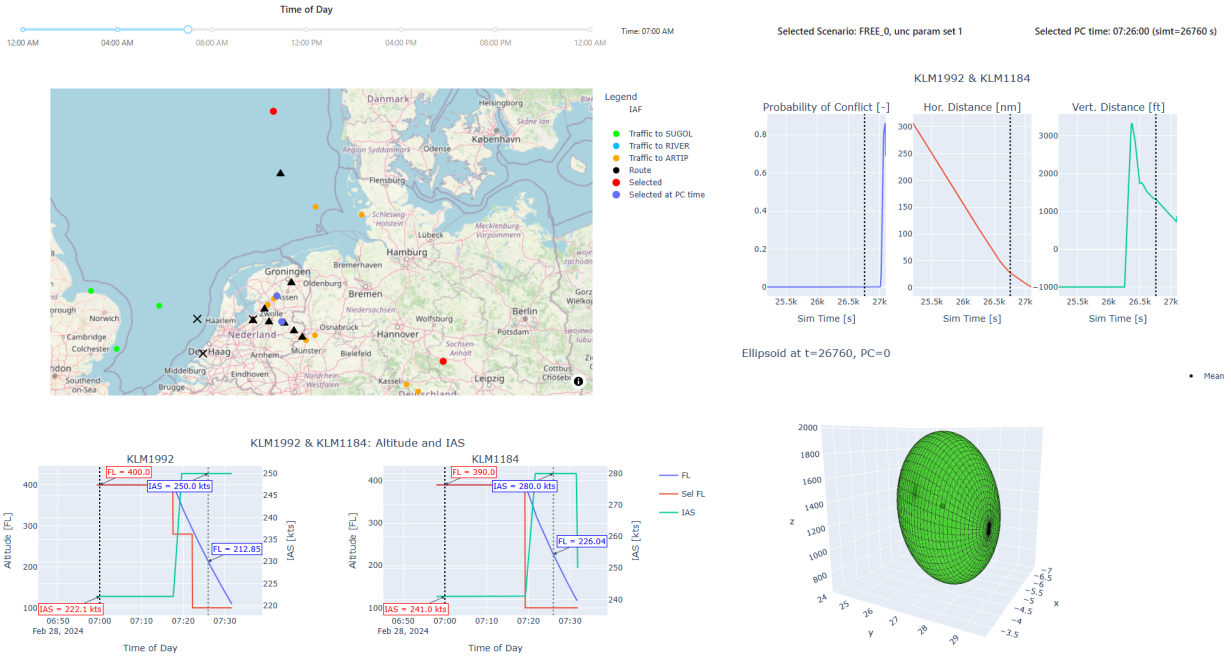


**Figure 2.3:** Conflict probabilities and nominal distance over time for two selected aircraft, and the uncertainty ellipsoid for a selected lookahead time.

In Figure 2.4, a lookahead time is selected where the probability of conflict is 46%. The map shows how the two aircraft will arrive at the IAF at nearly the same time. Their nominal IAF arrival time difference is 10 seconds. Because of this, the probability of conflict increases to more than 80% during the final stage of the descent. The part of the uncertainty ellipsoid lying in the PZ, thus where a loss of separation would occur, is coloured in red. Since here 46% of the ellipsoid is red, the probability of conflict is 46%. For this ellipsoid, the radius of $5$ nm of the protective zone is clearly visible as it cuts through the ellipsoid. It can also be seen that part of the ellipsoid is under the vertical separation minimum of $1000$ ft.

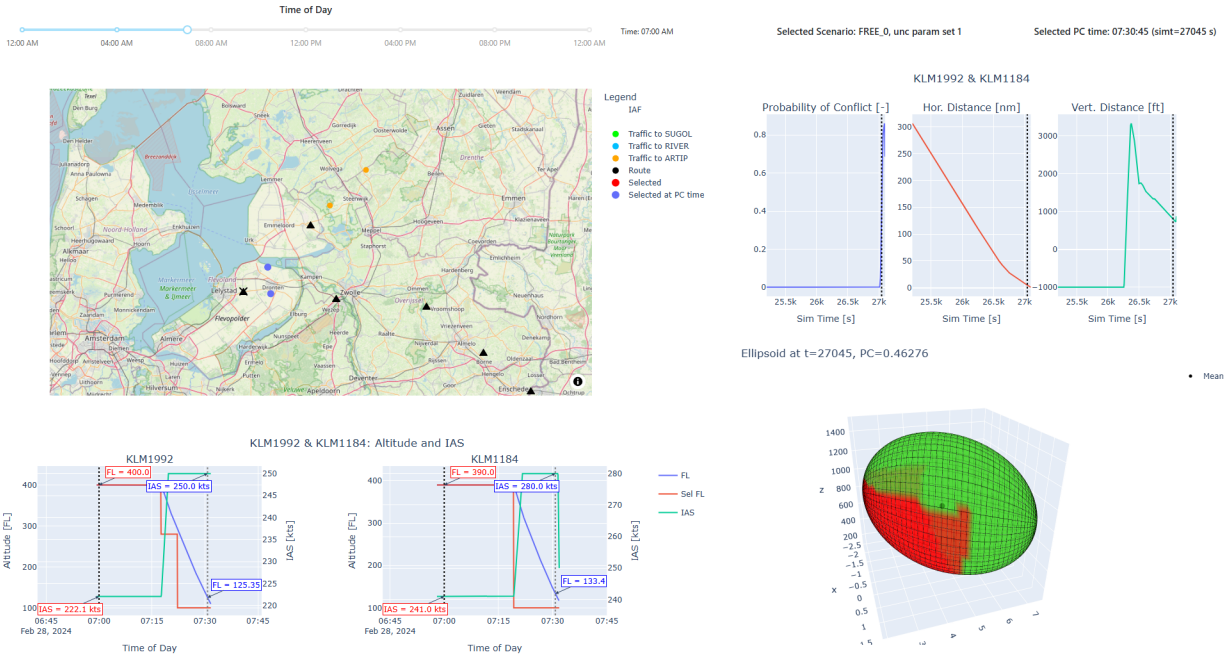


**Figure 2.4:** Snapshot of the dashboard for a lookahead time with nonzero conflict probability, for the two selected aircraft.

This demonstration shows that this dashboard is extremely valuable for understanding the simulations and the calculated conflict probabilities. It allows for visually verifying whether the calculated distances and conflict probabilities are sensible. Furthermore, it provides great insights in the type of conflicts encountered throughout the simulation. The example used in this demonstration shows how two aircraft on very different routes arrive at the IAF at nearly the same time, and how this is detected in terms of conflict probabilities. Many other conflict encounters, such as conflicts due to differences in cruise levels and TODs, can easily be visualised with this dashboard.

# Part C

## Literature Review & Research Definition

# 1 Introduction

The demand for air travel in Europe is increasing rapidly. In the record year 2019, nearly 11 million flights were conducted in European airspace[1]. This number is expected to increase to 16 million flights by 2050. Furthermore, new types of air vehicles will occupy the European skies, as autonomous aircraft and electric- and hydrogen-powered aircraft are developed. In order to ensure safe and efficient handling of all flights in the future, innovation is required. Over the past years, extensive research has been performed on Trajectory-Based Operations (TBO). The core of the TBO concept revolves around flying a user-preferred, optimal flight path by constructing the 4D trajectory prior to the flight, and sharing the trajectory information amongst all stakeholders [2]. This concept allows for Continuous Descent Operations (CDO). Via CDO, an aircraft can execute a continuous descent profile optimised to the operational capability of the aircraft, with low-thrust settings [3]. Various studies have demonstrated that CDs show a reduction in fuel consumption, emissions, and noise compared to conventional step-down descents with level segments.

In order to minimise fuel consumption, emissions, and noise, a continuous descent is ideally flown with idle thrust [4]. However, an idle descent comes with increased uncertainty as the vertical profile of an idle descent is highly sensitive to the descent speed profile, wind conditions, and aircraft weight. An alternative continuous descent follows a constant geometric flight path angle (FPA). This fixed-FPA descent has increased predictability and thus decreased uncertainty compared to an idle descent [4], [5]. However, CDOs are currently restricted to low traffic densities due to low predictability [6]. At Schiphol, this is restricted to nighttime operations only [7]. In reality, varying traffic densities occur throughout the day, so local low traffic densities can occur. Therefore, potential lies in investigating when idle descents can be flown throughout a 24-hour operation. No clear criteria exist for when these descents can be executed safely in the presence of other traffic. Using accurate trajectory uncertainty modelling to determine these criteria is novel. In the context of CDO, it is desired to investigate idle descent criteria in a full continuous descent environment. This entails flying solely idle and fixed-FPA descents throughout the day.

In this thesis, it will be investigated through simulations how idle and fixed-FPA descents can be applied throughout a 24-hour operation by means of per-flight descent application criteria, by analysing the number of successful idle descents. The descents will be flown towards Schiphol Airport using existing Standard Arrival Routes (STARs). Within the 24-hour operation, several scenarios with different idle descent execution restrictions are considered. The trajectory uncertainties associated with idle and fixed-FPA descents will be quantified, and the sensitivity of the developed criteria to trajectory uncertainty under the various restriction scenarios will be investigated. Although the focus is on Schiphol Airport, the aim is to develop general descent application criteria, such that the findings can be extrapolated to other airports and airspaces. A clear overview of when idle descents in particular can be applied throughout a 24-hour operation has the potential to accelerate the implementation of this outside of night hours. Furthermore, a quantification of the sensitivity of the number of successful idle descents to trajectory uncertainties potentially demonstrates the benefits of uplinking and downlinking data to and from the aircraft, such as uplinking weather information and downlinking aircraft mass via ATS B2 ADS-C EPP data.

The structure of this report is as follows. In chapter 2, the research foundations are established. The research objective and research questions are formulated. Chapters 3–5 contain background information obtained through a literature study. Chapter 3 contains information on the airspace structure and on the concept of Trajectory-Based Operations. In chapter 4, trajectory uncertainty is discussed. This is followed by a detailed explanation on idle and fixed-FPA descents in chapter 5.

# 2

# Research Foundations

In this chapter, the research foundations are established. Firstly, the research objective is formulated in section 2.1. Afterwards, the research questions are presented in section 2.2. Lastly, the expected outcome is discussed in section 2.3.

## 2.1. Research Objective

With the research topic having been introduced in chapter 1, the research objective can be formulated. The main research objective of this thesis is formulated as follows:

**Research Objective**

The objective of this research is to develop criteria for the execution of idle and fixed-FPA descents from cruise to the Initial Approach Fix (IAF) on a per-flight basis throughout a 24-hour operation under various idle descent application constraint scenarios, taking into account the associated trajectory uncertainties, and assessing the influence on the number of successful idle descents.

The objective can be broken down into several parts. The trajectory uncertainties associated with idle and fixed-FPA descents must be investigated and modelled such that these uncertainties can be displayed for the required look-ahead time until the IAF. Using these uncertainties, conflict probabilities between aircraft involving idle descents in various traffic scenarios can be calculated. These are then used to develop per-flight criteria sets for the application of idle and fixed-FPA descents. The influence of these criteria sets on the number of successful idle descents is evaluated for all traffic scenarios, with the idle descent application constraints and trajectory uncertainty sets considered. This then provides tangible results regarding the benefits of applying idle descents in particular throughout a 24-hour operation.

## 2.2. Research Questions

The research objective can be translated into research questions, the answers to which are necessary for accomplishing the research objective. The main research question is formulated as follows:

**Main Research Question**

How does the number of successful idle descents from cruise to the IAF, throughout a 24-operation, change for different per-flight idle and fixed-FPA descent application criteria, under various idle descent application constraint scenarios and trajectory uncertainties?

In order to aid the process of answering the main research question, several supporting research questions are formulated. By answering these questions, a final answer to the main research question can be constructed. The supporting research questions consider several aspects that need to be investigated before the main research question can be answered. These questions are provided below.

**Supporting Research Questions**

1. How can idle and fixed-FPA descents be simulated?
2. What are the trajectory uncertainties associated with idle and fixed-FPA descents?
3. What traffic scenarios are suitable for simulating idle and fixed-FPA descents?
4. What idle descent application constraint scenarios (also referred to as reference scenarios) must be considered?
5. What are the main KPIs to be used for developing per-flight idle and fixed-FPA descent application criteria?

## 2.3. Expected Results

Guided by the research questions, expected results can be formulated. These are formulated as three hypotheses:

- **H1: The strictness of the reference scenario and the number of successful idle descents have an inverse relationship.** Overall, it is expected that the most idle descents can be flown successfully when the restrictions from the reference scenario are the least strict. In practice, this means that it is expected that the most idle descents can be flown when idle descents are allowed throughout the full day. This way, the per-flight idle descent allocation can be exploited to the fullest. On the other hand, the smallest number of successful idle descents is expected under the strictest reference scenario.
- **H2: The strictness of the descent criteria and the number of successful idle descents have an inverse relationship.** Overall, the highest number of successful idle descents is expected when the idle descent criteria, which allocate idle descents on a per-flight basis, are the least strict. On the other hand, the smallest number is expected when the idle descent criteria are the strictest.
- **H3: Trajectory uncertainty and the number of successful idle descents have an inverse relationship.** A strong relation between trajectory uncertainty and the number of successful idle descents is foreseen. With greater uncertainty, the success rate is predicted to decrease.

The hypotheses are directly linked to the variables mentioned in the research objective and main research question, for whose unique combinations the number of successful idle descents will be calculated.

# 3

# Airspace and TBO

This chapter covers information on the Dutch airspace structure and on Trajectory-Based Operations (TBO). This information is essential as it provides the context for the research presented in this thesis. The general structure and layout of the Dutch airspace are elaborated on in section 3.1. A discussion on TBO and Continuous Descent Operations (CDO) in particular is provided in section 3.2.

## 3.1. Dutch Airspace Structure

Firstly, the general airspace structure will be discussed. Then, the layout of the airspace is elaborated on.

### 3.1.1. General Structure

The Flight Information Region (FIR) is the largest division of airspace [8]. In each FIR, flight information service and alerting service are provided. Figure 3.1 shows the Dutch Airspace, formally known as the Amsterdam FIR:

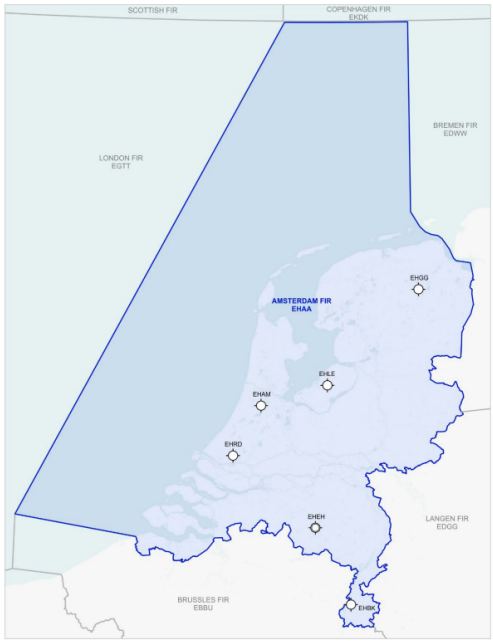


**Figure 3.1:** Map of the Amsterdam FIR with airports [9].

Two Air Navigation Service Providers (ANSPs) are involved in the ATC of the civil airspace within the Amsterdam FIR, as shown in Figure 3.2a [8]. The upper airspace, above FL245, is controlled by the Maastricht Upper Area Control Centre (MUAC). The lower airspace, below FL245, is controlled by Air Traffic Control the Netherlands (LVNL). The upper airspace is referred to as the Upper Control Area (UTA). The lower airspace is divided into several areas and zones. An overview of this is provided in Figure 3.2b.

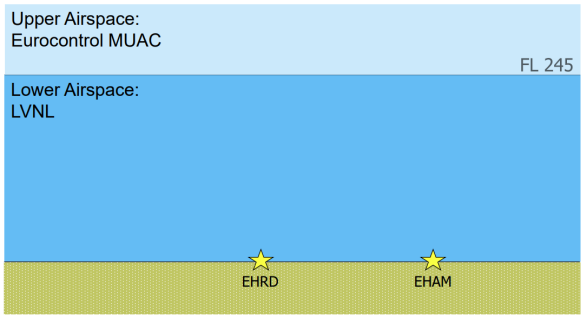


**(a)** Civil airspace responsibility in Amsterdam FIR.

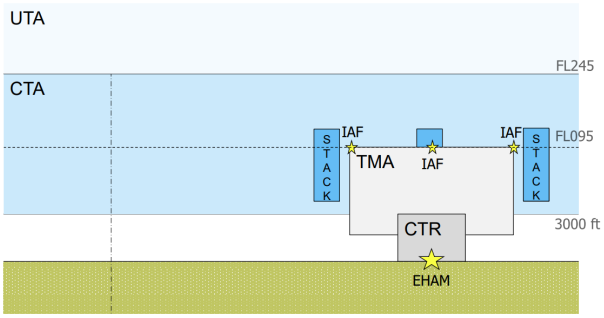


**(b)** Overview of the airspace structure around Schiphol Airport.

**Figure 3.2:** Overview of the Dutch civil airspace [8].

The Control Area (CTA) is generally controlled by Area Control (ACC). ACC is located at the LVNL main office building at Schiphol. In the CTA, departing aircraft climb further towards the ATS routes, which can be seen as highways in the sky [10]. Arriving aircraft are descending through the CTA towards an Initial Approach Fix (IAF), thereby following a Standard Arrival Route (STAR). The IAF marks the start of the approach procedure. At every IAF, a holding area is present. In this area, holding stacks can be built to regulate the traffic flow towards the airport.

The Terminal Manoeuvring Area (TMA) is controlled by Approach Control (APP). APP is located in the same operations room as ACC, at LVNL. This area surrounds the airport and is designed to protect aircraft climbing from or descending to the airport [10]. Arriving aircraft are guided from the IAF until the aircraft is established on the Instrument Landing System (ILS). Departing aircraft follow a Standard Instrument Departure (SID) until they arrive on the ATS route. APP sequences all arriving aircraft towards the runways, while ensuring sufficient spacing between all aircraft in the TMA.

The Control Zone (CTR) is controlled by Tower (TWR). TWR controllers are located in the aerodrome control towers. The CTR is the airspace directly surrounding the airport. It is designed to protect arriving and departing traffic in the vicinity of the airport [10]. TWR is responsible for operations on, to, and from active runways. When an aircraft is on the ground but not on an active runway, it is controlled by Ground Control (GND).

### 3.1.2. Airspace Layout

The layout of the Dutch airspace will be discussed further in this section. As stated earlier, the CTA contains aircraft flying to and from the ATS routes. As the CTA takes up a major part of the airspace in the Amsterdam FIR, is the CTA divided into sectors [10]. An ACC controller is responsible for all traffic in a specific sector. When the traffic density is low, multiple sectors can be combined, and one ACC controller then oversees the combined sectors. The CTA in the Amsterdam FIR is divided into five sectors. These are, along with the Schiphol TMA, displayed in Figure 3.3.

From this figure, it is clear that not all sectors are adjacent. The area between sectors 1 and 5, as well as sectors 2 and 3, is reserved for military airspace. Civil air traffic is not allowed to cross military airspace. Military airspace is part of the special traffic zones. These zones can be established when restrictions are necessary to accommodate air traffic operations that require special integration with civil aviation [10]. These zones are referred to as restricted areas, danger areas, and prohibited areas, depending on the imposed restrictions. Usually, special traffic zones are activated because of military operations. In addition, prohibited areas are often areas around objects that must not be overflown. Examples are royal palaces and international conferences.

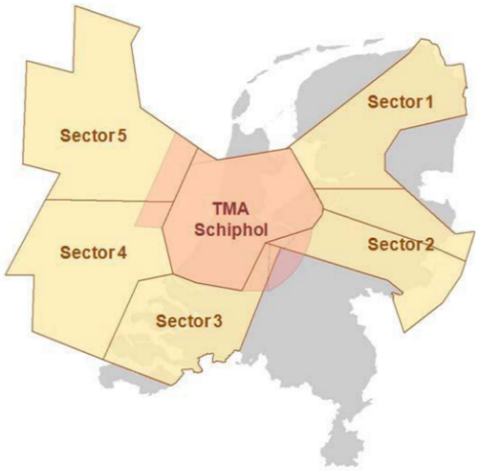


**Figure 3.3:** Map with the CTA sectors in the Amsterdam FIR and with the Schiphol TMA [10].

In Figure 3.4, the STARs for Schiphol are displayed. It shows several aspects that will be discussed under the figure.

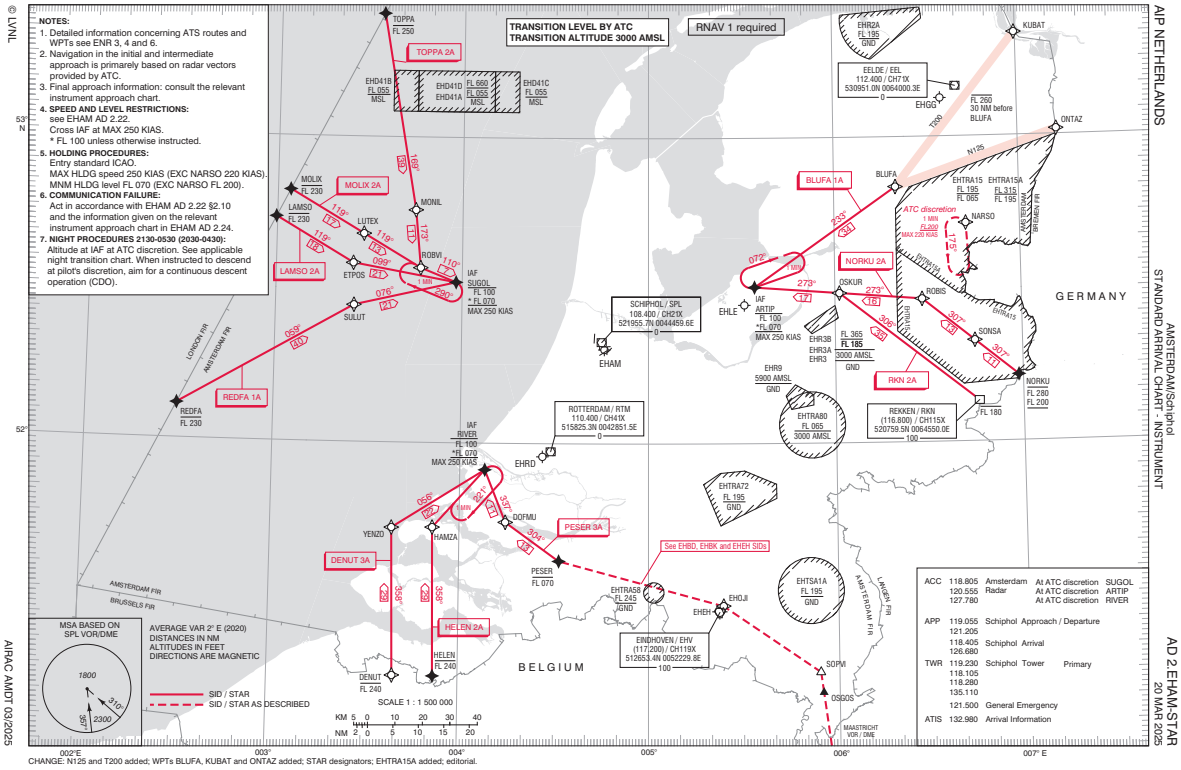


**Figure 3.4:** Schiphol Standard Arrival Chart, showing the STARs for Schiphol in the Amsterdam FIR [11].

It can be seen that, as stated earlier, each STAR ends at an IAF. For Schiphol, three IAFs exist. ARTIP is located in the East near Lelystad, above Flevoland. RIVER is located in the South near Europoort Rotterdam. SUGOL is located in the West, above the North Sea. At each IAF, an aircraft must be between FL70 and FL100, and have an indicated airspeed (IAS) of $250$ kts at maximum.

In addition, the holding patterns next to each IAF are drawn. One pattern consists of two right-handed $180°$-turns and two straight segments. The straight segment away from the holding fix is the outbound leg. Similarly, the segment towards the holding fix is the inbound leg. The inbound leg should have a duration of 1 minute. The time in the outbound leg may be adjusted such that the specified time of 1 minute for the inbound leg is met.

Lastly, the entry coordination points (COPs) are shown in Figure 3.4. These are the waypoints on the Amsterdam FIR boundary. They mark the start of the STAR and have a maximum (and sometimes minimum) FL defined with them. Therefore, it is important to note that generally speaking, an aircraft has already started its descent before entering the Amsterdam FIR. This means that the descent considered in this thesis research extends beyond the Amsterdam FIR, as it starts at cruise altitude.

## 3.2. Trajectory-Based Operations

This section elaborates on TBO and CDO in particular, to provide background information regarding these concepts.

### 3.2.1. General Concept

In Europe, ATM is at a crossroads. In 2019, the European Network experienced nearly 11 million flights [1]. This is expected to grow to 16 million flights by 2050. In the meantime, the European airspace will become more complex as new types of air vehicles emerge. Furthermore, the airspace for civil aviation in Europe has been reduced by approximately 20% because of the war in Ukraine.

In order to keep the capability of handling the growing amount of flights in the European Network safely and efficiently, innovation is required [1]. The Single European Sky (SES) program aims at improving ATM performance by reducing the fragmentation of the European airspace. The Single European Sky ATM Research (SESAR) project is the pillar of technological innovation of the SES. The SESAR 3 Joint Undertaking is a partnership between Europe's leading innovators in the aviation industry, to develop the required technologies and deliver the Digital European Sky. The Digital European Sky is a modern ATM system providing Europe with a high-performance, standardised, and interoperable ATM infrastructure. The European ATM Master Plan is the planning tool for realising the Digital European Sky. It sets out the vision and priorities for this. In addition, its aim is to make Europe the most efficient and environmentally friendly airspace in the world by 2045.

Two important concepts to accommodate this transformational change are Trajectory-Based Operations (TBO) and dynamic airspaces [1]. It is expected that in the future, many types of air vehicles will occupy the European skies. Electric and hydrogen aircraft will emerge. Remotely piloted and autonomous aircraft will fly through the European airspace. In order to guarantee optimisation of all aircraft trajectories while maintaining sufficient spacing in a congested airspace, TBO are necessary. The TBO concept foresees an ATM environment in which every flown flight path is as close as possible to the user-preferred flight path [2]. This is achieved by reducing potential conflicts and resolving imbalances between demand and capacity in an earlier stage, thereby increasing efficiency. The key to this is a 4D flight trajectory that is developed, managed, and shared between all stakeholders, so that it serves as a common reference for decision-making.

TBO involves three key aspects [2]. Firstly, the full intended trajectory is constructed in 4D, such that the geographical location, altitude, and time are known along the trajectory. Secondly, trajectory information is shared amongst the stakeholders. This allows all involved parties and systems to have access to up-to-date 4D flight information, as well as meteorological information, airspace information, and aerodrome information. As not all stakeholder require access to all information, the information sharing is based on operational needs only. The continuous sharing and updating of information is enabled through innovation in air-ground datalink, automation, and information management. Thirdly, trajectory management by Air Navigation Service Providers (ANSPs) is needed to ensure the trajectories can be executed. With TBO, more accurate trajectory predictions can be made because of the extensive trajectory information

available. A planned trajectory might change to accommodate any needs for modification of the trajectory. If, because of this, the execution precision is exceeded, replanning, coordination, and modification are required in order to obtain an updated, planned trajectory.

TBO plays a major role in avoiding unnecessary fuel burn, thereby reducing emissions [1]. As touched upon earlier, accurate trajectory predictions are required to ensure the optimal execution of the planned 4D trajectory. Dynamic spacing allows for more efficient traffic flow, which is beneficial for the execution of planned trajectories. Dynamically adjustable airspace sector configurations are seen as a possible solution. This provides maximum airspace efficiency and flexibility in response to (rapidly) changing weather conditions and traffic densities [12]. Therefore, dynamic airspaces can aid the implementation of the TBO concept.

Required Navigation Performance (RNP) is part of the Performance-Based Navigation (PBN) framework. At the core of RNP lies the specification of allowable navigation performance metrics, specifically for position accuracy, integrity, availability, and continuity of function [13]. RNP includes a requirement for on-board navigation performance monitoring and alerting [14]. For this, Global Navigation Satellite Systems (GNSS) are required. With this, possibilities arise to obtain very high lateral precision in the flight path. Modern aircraft are capable of conforming to defined lateral routes to a high degree of accuracy [15]. This way, trajectories can be tailored to a specific aircraft, thereby optimising fuel efficiency. Therefore, it is an important consideration for TBO.

### 3.2.2. Continuous Descent Operations

The TBO framework opens up the possibility for Continuous Descent Operations (CDO). The technology and strategic planning developed to realise TBO enables the implementation of CDO. CDO is defined as an aircraft operating technique for descent, that enables an aircraft to execute a flight profile that is optimised to the operating capability of the aircraft [3]. This includes low engine thrust settings and a low-drag configuration. With CDO, fuel burn and hence emissions and noise are reduced during descent. Level segments are reduced to a minimum, used only when needed to decelerate and configure the aircraft, or to establish on a landing guidance system. The optimal flight profile consists of a continuously descending path, from the Top of Descent (TOD) until the Final Approach Fix (FAF) or establishment on the landing guidance system. Ideally, the aircraft stays as high as possible until the optimal descent point (TOD) is reached, which is computed by the FMS. Every aircraft has a different optimal flight profile, as it is based on aircraft performance and weight. In addition, the optimal flight profile depends on weather conditions, meaning that the same aircraft has a different optimal profile every flight.

In order to safely execute continuous descents in varying traffic densities, traffic sequencing must start in the cruise phase or in the early stages of the descent, by small speed interventions [3]. This minimises the sequencing required at lower altitudes, leading to a reduction in fuel burn and noise. The challenge lies in balancing the goal of reducing flight times and distances, fuel burn, emissions, and noise, while meeting airport capacity and handling all traffic safely. Arrival management tools and sophisticated CDO procedures can aid the execution of CDO in environments where traffic density is high.

Continuous Descent Approaches (CDAs) have been flown at Schiphol Airport for multiple years during the night on a single runway [16]. A CDA is flown from the IAF to the ILS intercept point. Research on this has shown that fuel burn and noise are substantially reduced for CDA compared to conventional approaches. However, as a downside of CDA, it was found that the landing interval had to be increased from $1.8$ min to $4.0$ min, to guarantee sufficient spacing on the final landing segment. A flight test during which CDAs were executed at Louisville International Airport in 2002 also demonstrated significant reduction in fuel burn and noise [17].

Because of its broad definition, there are many ways in which a continuous descent can be flown [4]. In general, it consists of a series of descent segments that are consistent with piloting procedures. For a continuous descent, this entails a constant Mach until the crossover altitude. From there onwards, the descent consists of various constant and decelerating Calibrated Airspeed (CAS) segments. The two continuous descent types considered in this thesis research are the idle descent and the fixed-FPA descent. These types will be discussed in detail in chapter 5, as they form the basis of this research.

# 4

# Trajectory Uncertainty

In this chapter, trajectory uncertainty is discussed in detail. Firstly, track error definitions are discussed in section 4.1. Sources of trajectory uncertainty are listed in section 4.2. Then, trajectory uncertainty quantification techniques are discussed in section 4.3. Wind uncertainty is discussed in depth in section 4.4. Furthermore, conflict detection with and without uncertainties is elaborated on in section 4.5. Lastly, the potential effects of using ATS B2 ADS-C for trajectory prediction are mentioned in section 4.6.

## 4.1. Track Error Definitions

Before elaborating on the sources and quantification of trajectory uncertainty, it is important to discuss the errors associated with trajectory prediction. These error definitions are used to quantify the difference between the predicted trajectory and the actual trajectory flown [18], [19]. A distinction is made between spatial errors and temporal errors.

### 4.1.1. Spatial Error

The spatial error is the result of a combined horizontal and vertical error. The horizontal error is defined as the great-circle distance between the predicted and the actual position of an aircraft at time $t$. It can be decomposed into along-track and cross-track error components, as shown in Figure 4.1

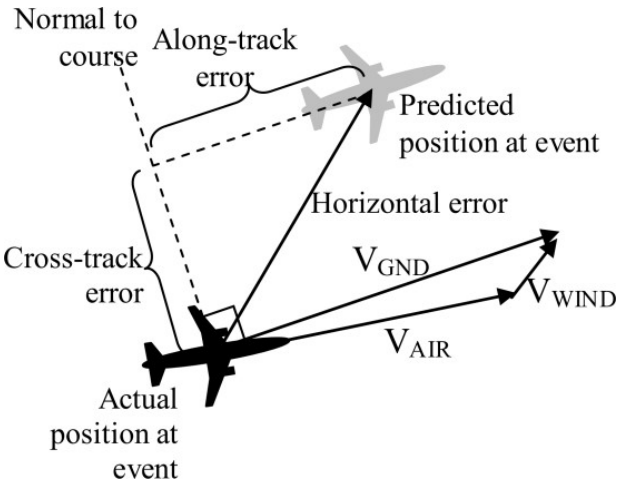


**Figure 4.1:** Visualisation of the decomposed horizontal error [18].

The along-track error is the component of the horizontal error that is projected onto the actual course of the aircraft. The cross-track error is projected perpendicular to the actual course. With this decomposition, it can be shown that the along-track error is associated with the temporal error, whereas the cross-track error is not. The vertical error is the altitude difference between the predicted and actual aircraft position. It is orthogonal to the horizontal error. Logically, the spatial error is the result of combining the horizontal and vertical error components.

### 4.1.2. Temporal Error

The temporal error is defined as the time difference between the predicted and actual time the aircraft is at a particular position along the course. This metric is commonly used to determine the status of a flight: premature, delayed, or on time. Because of this definition, the along-track error is the spatial representation of the temporal error. When a flight is on time, the along-track error is zero. However, the cross-track error may be non-zero, as it is perpendicular to the flown course.

## 4.2. Sources of Trajectory Uncertainty

Trajectory uncertainty is characterised by various factors that influence the accuracy of a trajectory prediction. Over the years, many studies investigating the sources of trajectory uncertainty have been conducted [13], [19]–[23]. Their results provide a clear overview of the sources of trajectory uncertainty, and their effects. The results are described in this section. Uncertainty sources can be divided into several categories, each describing a different type of source. These will be elaborated on below.

### 4.2.1. Initial Aircraft State

Every trajectory prediction starts with a set of initial aircraft states. These states include the aircraft position, heading, speed, vertical rate, and mass [20], [23]. Deviations in the assumed state values from the actual state values will propagate throughout the predicted trajectory [21]. Therefore, the accuracy of trajectory prediction is highly dependent on the accuracy of the initial aircraft state data.

Research has shown that deviations in aircraft mass greatly influence the uncertainty of the vertical profile of a trajectory [19], [20]. The uncertainty is larger during climb than during descent, but is clearly noticeable in both. During cruise, the uncertainty decreases to zero because the aircraft can hold accurately at a fixed altitude. In addition, deviation in speed profiles mainly affects the duration of flight and the rate of descent [19], [20].

### 4.2.2. Weather

The weather conditions considered are atmospheric temperature and pressure, as well as wind. The latter is arguably the biggest source of horizontal uncertainty. It has been shown that deviations in wind direction have a greater impact than deviations in wind speed [19]. Wind uncertainty is discussed in detail in section 4.4.

Deviations in temperature affect the computation of true airspeed (TAS). Aircraft speed control is performed using Mach above the cross-over altitude and calibrated airspeed (CAS) below the cross-over altitude. For conversion to TAS, the atmospheric temperature is needed. The TAS can then be converted to ground speed (GS). For trajectory prediction, the observed GS can be converted to Mach (or CAS). This means that temperature errors lead to errors in speed. However, the effect of temperature error on trajectory uncertainty has been found to be marginal to negligible [20].

The weather forecast used on the FMS must be as accurate as possible to limit the uncertainty in trajectory execution and increase efficiency, since fewer corrections with thrust or speed brakes are needed. The inaccurate representation of the wind in the FMS is a main contributor to errors in the total energy estimation, thereby reducing efficiency and increasing uncertainty [24]. Due to limited storage capacity in the FMS, only a limited, less accurate forecast can be loaded in. In order to reduce the difference between the used weather forecast and reality, updates of meteorological information are needed during flight [25]. With this, the forecast on the FMS can be updated, and the trajectory calculations can be adjusted.

In the planning phase, the 4D trajectory is constructed. The trajectory calculation can be optimised when the meteorological conditions are known best along the full trajectory [26]. This requires several stakeholders to share their data. Currently, only limited data is shared, so improvements are required. During the flight execution, accurate updates can be sent to the FMS based on the shared data. With more accurate trajectory information, buffers in declared capacity can be reduced, thereby increasing capacity and limiting recalculations.

### 4.2.3. Modelling

Several types of models are used in trajectory prediction. The types considered are the aircraft motion model, the aircraft performance model, and the Earth model. All will be elaborated on below.

The chosen aircraft motion model describes the mathematical representation of the aircraft, used to calculate future aircraft states. This representation includes the equations of motion and the numerical methods used to solve them. The accuracy of the mathematical representation compared to the real aircraft behaviour directly influences the trajectory prediction [21]. Common simplifications for the mathematical model are the small-angle approximation and the point mass approximation, considering only the centre of gravity of the aircraft [20]. The errors induced by aircraft motion modelling are considered to have a negligible effect on trajectory uncertainty.

The aircraft performance models are used for the calculations on aircraft performance. Straightforward examples are the calculations of thrust, drag, and fuel consumption for various flight conditions [21]. The parameters for these models are usually generalised. The Base of Aircraft Data (BADA) is commonly used for this. However, using generic performance models that are more robust, inevitably introduces errors in the trajectory prediction, thus contributing to trajectory uncertainty. Still, models from BADA are highly accurate, meaning that the trajectory uncertainties introduced by errors in aircraft performance modelling are negligible for ATM applications [20].

Another type of model needed for trajectory prediction is an Earth model. The accuracy of distance calculations and trajectory projections depends on the Earth model used. Common models used are the WGS84 model and a spherical Earth representation. However, errors in the Earth model are second order, and therefore negligible for ATM applications [20].

### 4.2.4. Aircraft Intent

Aircraft intent represents the commanded instructions and executed control actions as a result of ATC instructions, pilot procedures, and the flight plan [20], [21]. The uncertainty arises when the aircraft intent is (partially) unknown to the trajectory predictor. This uncertainty represents how the aircraft is actually operated compared to the original flight plan used for the trajectory prediction. This uncertainty includes deviations from the pilot and FMS models used for the prediction, such as a different reaction time to execute an ATC command.

In general, there are five types of intent errors that are of high impact on the prediction accuracy [22]. Vectors provided by ATC lead to deviations from the expected route, leading to spatial errors. Knowledge of the TOD location is limited when it depends on ATC clearance. Knowledge of altitude crossing restrictions is beneficial for the prediction, but it is not sufficient to accurately predict the TOD location. In addition, instructions to level off at interim altitudes are usually unaccounted for in the trajectory prediction. Lastly, uncertainty in the speed intent of the aircraft affects the vertical error, as well as the along-track error and temporal error.

### 4.2.5. Flight Control Inaccuracy

Uncertainty due to flight control inaccuracy is known as a flight technical error. This error describes the inability of an aircraft to stay on its specified track due to the performance of the FMS and the flight control systems. Arguments have been made stating that the long-term effect of flight technical errors on trajectory accuracy is negligible compared to other uncertainty sources [21]. The underlying reason for these errors becoming noticeable is that the aircraft is not operated according to its nominal capabilities. Because of this, it can be assumed that the specified, predicted track is then unsuitable for the aircraft, and that a more suitable track must be designed.

## 4.3. Trajectory Uncertainty Quantification Techniques

Trajectory uncertainty can be quantified using various techniques. In general, position uncertainty at time $t$ can be visualised as a 3D ellipsoid around the projected aircraft position on the predicted reference trajectory. This covariance ellipsoid consists of the probability distributions of the along-track, cross-track, and vertical errors compared to the reference trajectory. This is illustrated in Figure 4.2. The ellipsoids at each time $t$ together then form a tube that represents the possible aircraft positions throughout the trajectory [19].

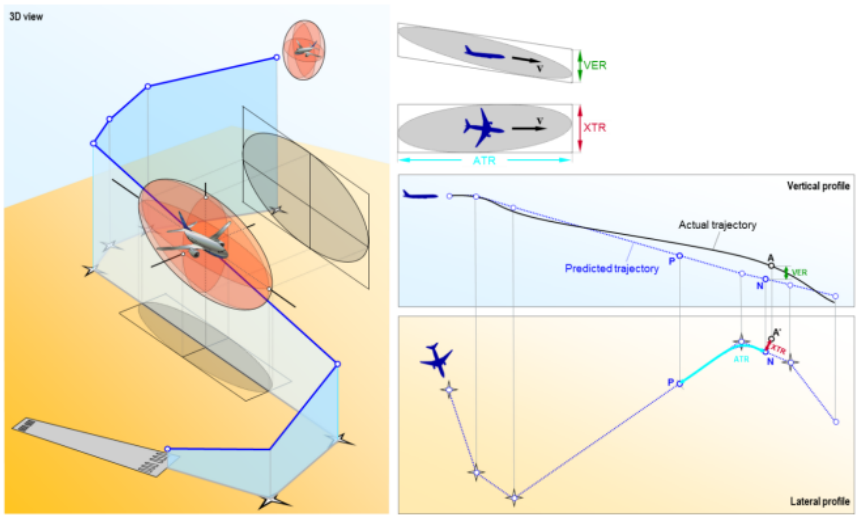


**Figure 4.2:** Visualisation of trajectory uncertainty as 3D ellipsoid [21].

The positional probability distributions can be constructed using parametric estimations. The error components are then described by zero-mean Gaussian random variables, for which the standard deviation increases with time [27]. This approach is suitable for online applications, because of the low computational load. It can therefore be used in a simulation of a representative traffic scenario, to determine the worst-case distances to other aircraft.

Monte Carlo simulations are used to investigate the effects of changes in uncertain inputs on the trajectory uncertainty, by means of simulating the trajectory. The inputs are treated as random variables, such that different combinations are used in each simulation. The Monte Carlo approach is commonly used to quantify trajectory uncertainties [19]–[21], [28], [29]. From the observed trajectory uncertainties based on varying uncertain inputs, relationships can be derived that describe the uncertainty in a parametric estimation. Essentially, the simulation outputs can be used to find parameter values for a parametric uncertainty estimation. This way, the results of Monte Carlo simulations can be converted to online applications by using them in parametric estimations. Conducting the simulations requires a high computational load, more so because many simulations are required to obtain statistically reliable results. Even though this method will be used in the research presented in this thesis, it is important to provide an overview of the possibilities. Therefore, two other methods are discussed below.

Polynomial Chaos Expansions (PCE) are an alternative to using Monte Carlo simulations. While obtaining practically the same trajectory uncertainties, the computational load is considerably lower [21], [30], [31]. With a PCE, the output of a system is presented as the sum of multivariate polynomials that form the orthogonal basis for the input parameters. This way, uncertainty in input parameters is directly translated into uncertainty in the system output, which is in this case the trajectory uncertainty. The amount of equations needed to solve the system is directly proportional to the amount of input parameters and the polynomial degree. Because of this, it takes less computational effort to solve this system than to run thousands of Monte Carlo simulations. However, solving this system still takes time in the order of seconds. Therefore, it is not suitable for online applications.

The Bayesian-Entropy information fusion method can be used to integrate data from a simulation model with real-time traffic data and physical constraints, to calibrate trajectory uncertainty [32]. With the updated uncertainties, more accurate trajectory predictions can be made. The method makes use of Bayes' theorem, stating that the posterior probability (the uncertainty after calibrating) is proportional to the product of the prior probability (the uncertainty from simulation data only) and the likelihood function, describing the likelihood of the observed real-time data given the simulation data. The likelihood function takes spatial errors into account, but no temporal errors. In order to visualise the trajectory confidence bounds for the prior and posterior distributions, Monte Carlo simulations are used. The distribution parameters are calculated for the waypoints, and samples from these waypoint locations are drawn to evaluate the resulting aircraft trajectories in the Monte Carlo simulations. Since this approach focuses on waypoint locations

and requires Monte Carlo simulations, it is not suitable for online applications. For online applications, the Monte Carlo simulations need to be replaced with a trained neural network that calculates the aircraft position based on simulation input parameters directly. Instead of focusing on the aircraft trajectory of one aircraft based on its input parameters, the Bayesian-Entropy information fusion method focuses on a specific route to be flown. However, the idea of incorporating real-time traffic data into the uncertainty estimate can be useful, also for validation purposes.

## 4.4. Wind Uncertainty

Wind uncertainty is one of the main contributors to trajectory uncertainty, and a central topic in this thesis, as wind uncertainty will be used to quantify trajectory uncertainty. A discrepancy between the actual winds and the wind forecast known to the FMS leads to deviations from the predicted trajectory. Due to limited storage capacity on the FMS, the wind forecast loaded into the FMS covers a small number of altitude levels on which the weather forecast is known [24]. The FMS considered in [24] accepts four levels for descent. These are generally standard levels. The wind forecast loaded into the FMS is taken from the wind profile above the destination. The FMS then interpolates between the levels to obtain a predicted wind profile, as shown in Figure 4.3. The FMS uses this profile to construct its geometric path for an idle descent, or to control staying on a predefined path. Since it is reasonable to assume that the wind profile constructed by the FMS, based on four levels at the destination location, has deviations from the actual wind forecast throughout the descent, the trajectory will not be flown as predicted.

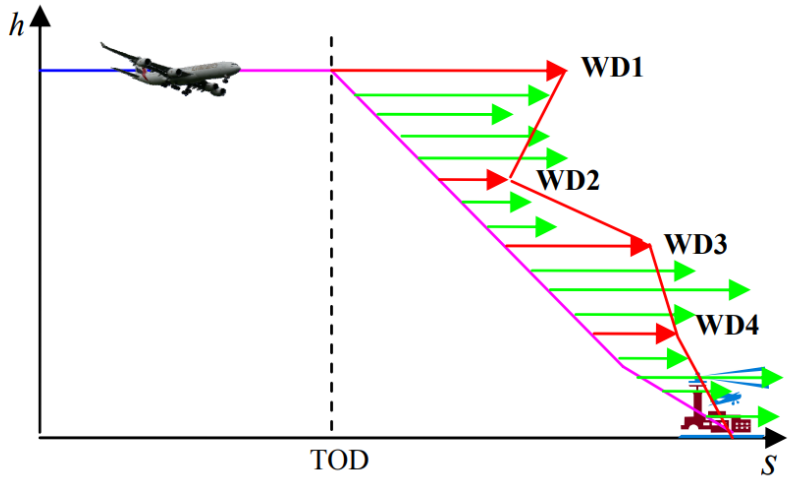


**Figure 4.3:** Interpolated wind profile (red line), based on wind forecast at used levels (red arrows) and compared to the actual profile (green arrows) [24].

The weather forecast for the Dutch FIR is provided by the Royal Netherlands Meteorological Institute, abbreviated to KNMI in Dutch. Data are provided in the GRIB (GRIdded Binary) format. Every file provides information on wind, temperature, and specific humidity on a predefined grid of latitudes and longitudes for various pressure levels. Every file contains a forecast for a specified time in the future, or for the current time. The forecasts from the GRIB files are used to select the limited forecast used in the FMS.

The wind profile prediction error can be split up into three components [24]. The first component is the prediction error in the base forecast data. This defines the difference between the weather forecast and the actual weather. The second component is the error due to selecting forecast grid cells that are not on the planned trajectory. As stated earlier, the wind forecast is taken from the wind profile above the destination, meaning it is likely not representative for an entire descent. This error can be reduced by updating the meteorological information in the FMS during flight execution, using uplink to the aircraft [25]. The last error component is due to interpolation by the FMS between the available levels.

A proposed method to obtain better insight into wind prediction accuracy is to utilise wind forecast integrity monitoring [13]. By comparing wind forecasts with the downlinked aircraft observed values, regions with

poor prediction accuracy can be identified. Then, using this information, the forecast can be corrected or the trajectory uncertainty can be increased.

In [24], a method is proposed to increase the accuracy of the winds available to the FMS. The Tailored Descent Winds Tool (TDWT), developed by Airservices Australia, aims to reduce the wind profile prediction error in all three components described above. Firstly, it utilises weather forecasts with the highest resolution. Secondly, the wind profile is updated along the trajectory, instead of using the wind profile above the destination. Lastly, the winds at the four levels for the FMS are not just the forecast winds at those levels. Instead, these winds are determined so that they describe the entire wind profile as accurately as possible, thereby minimising the interpolation error. By using weights, the solution is biased towards levels where the wind is most significant to true airspeed. This is achieved by minimising the Root Mean Square Interpolation Error (RMSIE). The resulting tailored winds at the four levels can then be uplinked to the FMS. The study found that the Tailored Descent Winds provide the FMS with a more accurate representation of the full wind profile compared to the standard forecast at each level.

According to the literature, two main approaches are used to quantify wind uncertainty. The first approach uses time-lagged ensembles of weather forecasts for a specific time, to determine the wind uncertainty [21], [33]–[35]. The forecast error is measured as the difference with the 0-hour forecast. Wind forecast uncertainty is defined as the standard deviation of the ensemble members, where each member is an $x$-hour forecast for a specific time. Since wind forecast errors decrease with decreasing lead time, weighted interpolation can be used to determine the uncertainty. Purely random corrections can be included to account for model residuals, measurement errors, and nominal wind determination (interpolation) errors [34]. A drawback of this approach is that the correlation between ensemble members is generally larger than for other techniques [33]. However, a key advantage is that with this approach, regional variations in uncertainty that are related to weather phenomena can be identified. In addition, no additional model forecasts next to the obtained forecast from e.g. the KNMI are needed, making this method less computationally intensive.

In [35], the ECMWF EPS is used. This is a 51-member ensemble based on the ECMWF Global Atmospheric Model. This generates 51 forecasts at the same time for a particular forecast horizon. Every forecast uses slight different initial conditions, to get an idea of the weather uncertainty. It can be compared to the Monte Carlo simulation method. From these forecasts, probability density functions of the wind can be constructed, as done in [35]. Having multiple ensemble members at the same time stamp will lead to better wind uncertainty modelling than having to use $x$-hour forecasts as ensemble members. However, it is the only feasible option if only one forecast is provided per time stamp.

The second approach compares aircraft wind data with the wind forecast at that time [36], [37]. The wind forecast is again provided by a meteorological institute such as KNMI. However, the papers cited here use the Rapid Update Cycle (RUC), an American model that was replaced after the papers were published. In [36], ACARS reports from the aircraft were used to compare the wind forecasts to. The differences found account for both errors in the ACARS data and errors in the forecast model. From this, the actual forecast model errors can be estimated. Since the wind uncertainty model estimates found in the literature are for the United States, it cannot be assumed blindly that these are representative for the Dutch FIR. In addition, RUC and ACARS data should be replaced by KNMI and ADS-C data, which will have different uncertainties. Therefore, the first approach described here is a more suitable alternative for evaluating wind uncertainty.

When quantifying trajectory uncertainty, it is important to consider the influence of wind error correlation. Various studies have researched this [37]–[40]. It was found that simplifying assumptions regarding the wind field correlation influences trajectory uncertainty. This is especially relevant for the conflict probability between two aircraft. Correlation effects are stronger for aircraft in closer proximity of each other. By neglecting wind correlation, the conflict probability is overestimated [37]. Therefore, neglecting it is a conservative assumption. When only wind uncertainty is considered in the model as a source for trajectory uncertainty, this conservative assumption can implicitly account for the trajectory uncertainty as a result of other sources discussed in section 4.2. Even though neglecting wind correlation results in less accurate trajectory uncertainty computations and subsequent conflict probabilities, the estimate can be considered a first conservative approximation.

## 4.5. Conflict Detection

In order to determine whether a planned trajectory can be executed, it is important to consider potential conflicts with other aircraft. State-based conflict detection is the most straightforward method and will be elaborated on to demonstrate the concept of conflict detection. However, since trajectory uncertainties must be considered, a probabilistic approach to conflict detection is provided, as this approach will be used in the thesis research. This approach can be used in online applications and takes into account trajectory uncertainties to estimate conflict probabilities.

### 4.5.1. State-Based Conflict Detection

Two aircraft are in a conflict when a loss of separation between the two is predicted within the lookahead time horizon. A loss of separation (LoS) occurs when the two aircraft positions are within the protected zone (PZ), thereby violating the separation minima. Conflicts are detected by predicting the aircraft trajectories and evaluating these against the separation minima. To illustrate this, the principle of state-based conflict detection will be explained. This method uses the current aircraft positions and extrapolates the current velocity vectors, assuming that the aircraft continue their current path [41]. The closest point of approach (CPA) is defined as the relative position closest to the other aircraft at any point in time. The time of CPA and the CPA distance are calculated using vector algebra. In Figure 4.4, horizontal conflict detection is visualised. It shows the relative position of two aircraft. Around aircraft B, the PZ of radius $R$ is drawn. When aircraft A is within this PZ at any time, a LoS has occurred. The CPA distance is also drawn.

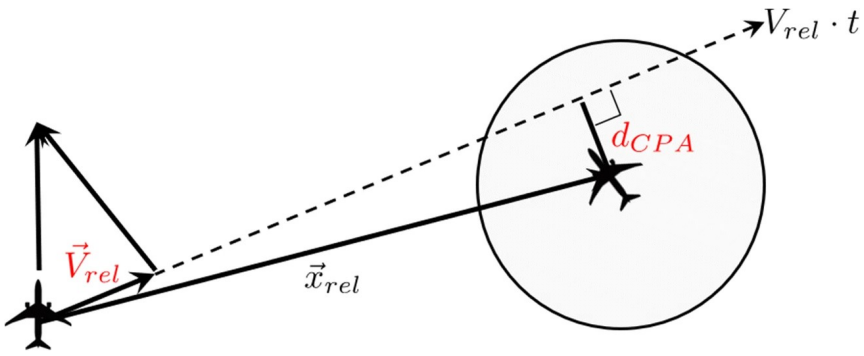


**Figure 4.4:** State-based conflict detection by calculating the closest point of approach [41].

The relative velocity $\vec{V_{rel}}$ and relative position $\vec{x_{rel}}$ are defined as:

$$\begin{aligned} \vec{V}_{rel} &= \vec{V}_a - \vec{V}_b \\ \vec{x}_{rel} &= \vec{x}_b - \vec{x}_a \end{aligned} \tag{4.1}$$

The time of CPA and the CPA distance can be calculated as follows [41]:

$$\begin{aligned} \vec{V}_{rel} &\perp \left(\vec{x}_{rel} - t_{CPA} \cdot \vec{V}_{rel}\right) \\ \vec{V}_{rel} &\cdot \left(\vec{x}_{rel} - t_{CPA} \cdot \vec{V}_{rel}\right) = 0 \\ t_{CPA} &= \frac{\vec{V}_{rel} \cdot \vec{x}_{rel}}{\vec{V}_{rel} \cdot \vec{V}_{rel}} = \frac{\vec{V}_{rel} \cdot \vec{x}_{rel}}{\left|\vec{V}_{rel}\right|^2} \\ d_{CPA} &= \left|\vec{x}_{rel} - \vec{V}_{rel} \cdot t_{CPA}\right| \end{aligned} \tag{4.2}$$

Subsequently, the time interval of LoS depending on the PZ radius $R$ is:

$$t_{LoS_{bound}} = t_{CPA} \pm \frac{\sqrt{R^2 - d_{CPA}^2}}{\left|\vec{V}_{rel}\right|} \tag{4.3}$$

For vertical spacing, the calculation involves only an altitude difference and a relative vertical speed. Here, the calculations will be shown for a constant relative vertical speed to demonstrate the calculation procedure. The time of vertical CPA is calculated as:

$$\begin{aligned} h_{rel} &= h_b - h_a \\ vs_{rel} &= vs_a - vs_b \\ t_{CPA} &= \frac{h_{rel}}{vs_{rel}} \end{aligned} \tag{4.4}$$

Here, $h_{rel}$ is the relative altitude and $vs_{rel}$ is the relative vertical speed. These are calculated with opposite signs, so that a positive time results when aircraft A is lower than aircraft B and has a positive relative vertical speed. This means that the two aircraft are vertically moving towards each other. The $t_{CPA}$ is the time when both aircraft are at exactly the same altitude. Since a minimum vertical separation $h_{sep}$ of usually $1000$ ft is required, the time interval of vertical LoS is defined as:

$$t_{LoS_{bound}} = t_{CPA} \pm \frac{h_{sep}}{vs_{rel}} \tag{4.5}$$

The combined LoS time interval is found by taking the overlapping interval from the horizontal and vertical intervals.

### 4.5.2. Probabilistic Conflict Detection

The lookahead time used for conflict detection is important for determining what conflict detection model is appropriate to use. For very short lookahead times, the previously explained state-based detection model can be sufficiently accurate. The lookahead time considered in this research is around $20$ minutes, meaning that mid-range conflict detection models are more appropriate. Furthermore, it is important that conflict probabilities can be calculated in real-time. Since trajectory uncertainty changes over time, the conflict probability changes too. An established mid-range conflict prediction model that is appropriate for this application [27], will be explained below.

Trajectory uncertainty is modelled as the variance of the along-track error as a function of time and as the variance of the cross-track error as a function of time. The along-track variance grows quadratically with time, while the cross-track error grows quadratically with distance, which is a function of time. The cross-track variance saturates at a fixed value because corrections for the cross-track error are done in the short term, either by the pilots or the FMS, which has a saturation point. The relations are written out below:

$$\begin{aligned} \sigma_a^2(t) &\sim r_a^2 t^2 \\ \sigma_c^2(t) &\sim \min\{r_c^2 s^2(t), \bar{\sigma}_c^2\} \end{aligned} \tag{4.6}$$

Here, $r_a$ and $r_c$ are the error growth rates. These can be determined from Monte Carlo simulations that include trajectory uncertainties, or from literature, depending on the desired accuracy. This uncertainty model is considered fairly accurate for a lookahead time up to around $20$ minutes [27]. Since corrections for the cross-track error are done in the short term, a saturation point is present. Meanwhile, along-track errors are dealt with in the long term, usually by speed instructions from ATC.

An aircraft trajectory $\vec{x}(t)$ is assumed to be normally distributed, with as mean the predicted nominal trajectory $\vec{p}(t)$ and as variance the covariance matrix composed from the track variances and corrected for aircraft heading $\theta$ using a rotation matrix:

$$\begin{aligned} \vec{x}(t) &\sim \mathcal{N}(\vec{p}(t), V(t)) \\ V(t) &= R(\theta)\bar{V}(t)R(\theta)^T \\ \bar{V}(t) &= \begin{bmatrix} \sigma_a^2 & 0 \\ 0 & \sigma_c^2 \end{bmatrix} \\ R(\theta) &= \begin{bmatrix} \cos\theta & -\sin\theta \\ \sin\theta & \cos\theta \end{bmatrix} \end{aligned} \tag{4.7}$$

Next, it is assumed that the trajectories of aircraft A and B are uncorrelated. In practice, this is not the case due to e.g. correlations in wind fields. However, by assuming this, the spacing between the two aircraft $\vec{d}(t)$ can then also be modelled as a Gaussian random variable. The mean is the distance function between the two nominal trajectories. The variance is the addition of the separate covariance matrices for aircraft A and B:

$$\begin{aligned} \vec{d}(t) &\sim \mathcal{N}(\vec{\mu}(t), Q(t)) \\ \vec{\mu}(t) &= \vec{p}_A(t) - \vec{p}_B(t) \\ Q(t) &= V_A(t) + V_B(t) \end{aligned} \tag{4.8}$$

The resulting multivariate probability density function, $\vec{p}_{\vec{d}_t}$, represents the uncertainty ellipse of the distance between two aircraft. The overlap between this ellipse and the PZ is the probability of conflict $PC$. This overlap can be found by integrating $\vec{p}_{\vec{d}_t}$ over the PZ:

$$PC(t) = \int_{y \in PZ} \vec{p}_{\vec{d}_t}(y)\, dy \tag{4.9}$$

$PC(t)$ is calculated for every time step until the lookahead time $T$. The maximum value of conflict probability is straightforwardly:

$$C(\gamma) = \max_{t \in [0,T]} PC(t) \tag{4.10}$$

Here, $\gamma$ represents the current step in time. Every new time step, new conflict probabilities are calculated until the lookahead time. When the maximum conflict probability $C(\gamma)$ is higher than a predefined threshold $\bar{C}$, a conflict is declared.

Because the nominal trajectories are known and readily available at each time step, the nominal CPA can be determined from these trajectories immediately. At this $t_{CPA}$, $PC(t)$ will then be the highest. In other words, $C(\gamma) = PC(t_{CPA})$. Knowing this decreases the computational effort, since the integration over PZ has to be conducted only once per time step.

In Figure 4.5, the horizontal ellipse overlap is shown on the left. This ellipse represents the joint uncertainty from $\vec{d}(t)$, as explained earlier. The horizontal PZ is a circle with a specified radius, which is most commonly $5$ nm. This is the standard minimum separation when surveillance systems such as radar or ADS-B are used. The separation may be decreased in some situations, that are not taken into account in this research.

The described model only considers horizontal conflict detection. However, for the 3D case, the vertical error should also be accounted for. It can be assumed that the vertical error variance grows linearly with time during climb or descent, and return to zero when a set altitude is reached. This is because the FMS is very capable of altitude holding. The covariance matrix $\bar{V}(t)$ then becomes:

$$\sigma_v^2 = r_v t$$
$$\bar{V}(t) = \begin{bmatrix} \sigma_a^2 & 0 & 0 \\ 0 & \sigma_c^2 & 0 \\ 0 & 0 & \sigma_v^2 \end{bmatrix} \tag{4.11}$$

The vertical error growth rate for climb and descent can also be determined from Monte Carlo simulations, or from literature [20]. The probability density function $\vec{p}_{\vec{d}_t}$ then becomes 3D multivariate. It is now represented by an ellipsoid. The 3D PZ is a cylinder, with a predefined height of usually $2000$ ft. This is because $1000$ ft is the minimum vertical separation for IFR flight. On the right side of Figure 4.5, the vertical overlap of the joint uncertainty ellipsoid is illustrated.

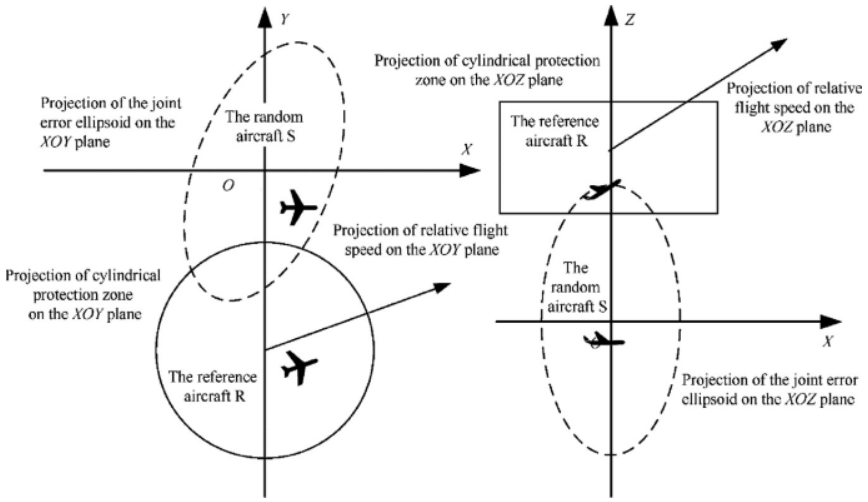


**Figure 4.5:** Joint trajectory uncertainty overlap with the protective zone [42].

In [35], a method is proposed to transform wind uncertainties into distance uncertainties and subsequently into conflict probabilities. The conflict probabilities are calculated in essentially the same way as described above in Equation 4.9. However, the probability density function of the distance between aircraft is generated by transforming the probability density functions of the wind components. This is done using the Probabilistic Transformation Method (PTM).

The idea behind this method is that an explicit expression relating the wind components and the aircraft distance is found. When the wind components then are expressed in terms of aircraft distance, the distance probability density function is obtained by multiplying the wind probability density function with the absolute value of the Jacobian determinant of that expression.

Finding the explicit expression is not straightforward. Since no clear explanation of how the expression was obtained in [35] is available, a proper implementation of the method becomes difficult. Instead, Monte Carlo simulations of aircraft trajectories using wind uncertainties to find the track error variances, which are used in [27], are more robust.

## 4.6. Possibilities with ATS B2 ADS-C

ATS B2 Automatic Dependent Surveillance - Contract (ADS-C) is a new datalink technology. It allows ATC to obtain aircraft information from the FMS directly, without requiring any pilot interaction. It is operational at MUAC since May 2022 [43]. Aircraft can automatically establish an ADS-C connection and downlink aircraft intent information to the control centre. While basic information is transmitted with every message, it can be expanded with the Extended Projected Profile (EPP) [44]. With this, information about the reference trajectory computed by the FMS as the predicted path can be shared with the ground, in a maximum of 128 trajectory change points. In addition, the current gross mass of the aircraft can be shared. Furthermore, meteorological data as perceived by the aircraft are shared [43].

With all this information available on the ground, the accuracy of trajectory predictors on the ground can be improved significantly [44]. Knowing the aircraft mass practically eliminates the mass uncertainty discussed earlier. Also, from the EPP data, it can be analysed what type of descent is flown, e.g. an idle or a fixed-FPA descent. This information can be used to analyse the actual trajectory and, if necessary, adjust the trajectory predicted on the ground. In addition, ”what-if” scenarios can be constructed by a TP on the ground, thereby using the downlinked aircraft intent. This is done by making adjustments to the received intent and analysing the results.

In general, ATS B2 ADS-C allows controllers to have a clearer picture of aircraft intent and airspace sector loads [43]. Air navigation efficiency, situational awareness, and safety are improved, while the odds of human errors going unnoticed are reduced. Since ATS B2 ADS-C data are already available and will become more commonly used in the future, the effect of having access to the data needs to be included in the trajectory uncertainty models.

# 5

# Idle and Fixed-FPA Descents

This chapter contains information on idle and fixed-FPA descents. Firstly, relevant descent physics are elaborated on in section 5.1. Then, idle descents are explained in detail in section 5.2. This is followed by a detailed discussion on fixed-FPA descents in section 5.3. Lastly, the knowledge gap that this research project attempts to fill is formulated clearly in section 5.4.

## 5.1. Descent Physics

In this section, the descent physics are explained. First, airspeed definitions are provided. Then, the equations of motion for an aircraft in descent are provided, and expressions for the FPA are derived.

### 5.1.1. Airspeed Definitions

During a descent, the airspeed ranges from high subsonic numbers near the TOD to low subsonic numbers at landing. Therefore, it is important to discuss the concept of compressible flow. All flows are in fact compressible, meaning they experience considerable changes in fluid density under certain circumstances. As a rule of thumb, flow can be considered incompressible for Mach numbers below 0.3 [45]. Above Mach 0.3, the flow should be treated as compressible. Within the TMA, Mach numbers are generally around 0.3. This means that assuming incompressible flow would be valid. For the descent from the TOD to the IAF, the Mach number is always higher than 0.3. Therefore, compressible flow must be assumed. This information is relevant for the calculation of various airspeeds. Furthermore, the flow is always considered to be isentropic.

Airspeed can be expressed in various ways. When talking about airspeed, it is important to clearly state which airspeed type is meant. An overview of the various airspeed types and their relationships will be provided below.

Indicated Airspeed (IAS) is the airspeed reading measured by the Airspeed Indicator (ASI) [46]. The airspeed is calculated from the total pressure measured with a pitot tube and the static pressure measured with a static port. This pressure difference is the dynamic pressure, which is a measure for velocity. IAS is uncorrected for variations in atmospheric conditions, instrument error, and installation error. However, an airspeed independent of atmospheric conditions (temperature, pressure, density) can form the basis for aircraft performance characteristics. For example, the stall speed of an aircraft is a constant value when expressed in IAS. In IAS, the stall speed is expressed as the dynamic pressure required to not stall. The required dynamic pressure is independent of atmospheric conditions. This means that the same dynamic pressure is required at any altitude. The actual speed of the air required to obtain this dynamic pressure, of course, changes with altitude. This will be discussed later.

For subsonic, inviscid, compressible flow, IAS is calculated as [45]:

$$V_{IAS} = a_0 M_0 = \sqrt{\gamma R T_0} \sqrt{\frac{2}{\gamma - 1} \left( \left( \frac{q}{p_0} + 1 \right)^{\frac{\gamma - 1}{\gamma}} - 1 \right)} \tag{5.1}$$

From this equation, it can be seen that only the dynamic pressure $q$ is a variable. $T_0$ and $p_0$ are the

temperature and static pressure at sea level, being $288.15$ K and $101\,325$ Pa respectively. $R$ is the specific gas constant of air, with $R$ = $287$ J$/$(kgK). Lastly, $\gamma$ is the heat capacity ratio of air, with $\gamma$ = 1.4.

Calibrated Airspeed (CAS) is the IAS corrected for installation and instrument error [46]. Unfortunately, installation errors and instrument errors are always present. Generally, these errors are the greatest at lower airspeeds. At higher airspeeds and altitudes, IAS and CAS are approximately the same. No explicit mathematical model exists to convert IAS to CAS. Airspeed calibration charts exist and can be used as look-up tables for conversion between IAS and CAS. Since this research considers higher speeds and altitudes, it is valid to assume that IAS is equal to CAS.

Equivalent Airspeed (EAS) is CAS corrected for compressibility effects [45]. These effects occur at higher speeds and altitudes, as stated earlier. EAS and CAS are equal at sea level. Where IAS (and thus CAS) considers the static pressure and temperature at sea level only, EAS considers the actual static pressure, as well as a compressibility correction. It still uses the temperature at sea level. For low subsonic speeds and lower altitudes, it is often assumed that EAS and CAS are equal. This assumption follows from assuming incompressible isentropic flow. For high subsonic speeds and altitudes, which are considered when analysing descents from the TOD to the IAF, the compressibility effects cannot be neglected, as stated earlier.

For subsonic, inviscid, compressible flow, EAS is calculated as [45]:

$$V_{EAS} = a_0 M \sqrt{\frac{p_s}{p_0}} = \sqrt{\gamma R T_0} \sqrt{\frac{2}{\gamma - 1} \left( \left( \frac{q}{p_s} + 1 \right)^{\frac{\gamma - 1}{\gamma}} - 1 \right)} \sqrt{\frac{p_s}{p_0}} \tag{5.2}$$

Here, the actual static pressure $p_s$ is used to calculate the Mach number at altitude. Also, the compressibility correction $\sqrt{\frac{p_s}{p_0}}$ is added. Note that the speed of sound $a_0$ is still calculated for sea level conditions.

When IAS is known, it is possible to determine the corresponding EAS. From Equation 5.1, the dynamic pressure $q$ can be obtained by rewriting the equation. Furthermore, $p_s$ can be obtained for the current altitude, by using the International Standard Atmosphere (ISA) relations. The values found for $q$ and $p_s$ can then be used in Equation 5.2 to obtain the corresponding EAS.

True Airspeed (TAS) is CAS corrected fully for altitude and non-standard temperature [46]. It defines the actual speed of the air travelling over the aircraft wing. Since air density decreases with increasing altitude, an aircraft has to fly faster at higher altitudes to obtain the same dynamic pressure compared to lower altitudes. For a given CAS, TAS thus increases with increasing altitude.

For subsonic, inviscid, compressible flow, TAS is calculated as [45]:

$$V_{TAS} = aM = \sqrt{\gamma R T_s} \sqrt{\frac{2}{\gamma - 1} \left( \left( \frac{q}{p_s} + 1 \right)^{\frac{\gamma - 1}{\gamma}} - 1 \right)} \tag{5.3}$$

It is clear that for TAS, the atmospheric conditions at altitude are used. Both the temperature $T_s$ and static pressure $p_s$ at altitude are required.

Converting EAS to TAS is quite straightforward. The relation between EAS and TAS can be derived by combining Equation 5.2 and Equation 5.3. Dividing Equation 5.3 over Equation 5.2 gives:

$$\frac{V_{TAS}}{V_{EAS}} = \frac{aM}{a_0 M \sqrt{\frac{p_s}{p_0}}} = \frac{\sqrt{\gamma R T_s}}{\sqrt{\gamma R T_0} \sqrt{\frac{p_s}{p_0}}} = \sqrt{\frac{T_s p_0}{T_0 p_s}} \tag{5.4}$$

From the ideal gas law, $p_s = \rho R T_s \Rightarrow \rho R = \frac{p_s}{T_s}$, this ratio can be expressed as:

$$\frac{\rho_0}{\rho} = \frac{p_0 T_s}{p_s T_0} \tag{5.5}$$

Therefore:

$$\frac{V_{TAS}}{V_{EAS}} = \sqrt{\frac{T_s p_0}{T_0 p_s}} = \sqrt{\frac{\rho_0}{\rho}} \tag{5.6}$$

This shows that EAS and TAS are linked through a correction for air density, with $\rho$ the air density at altitude and $\rho_0$ the air density at sea level, being $1.225\,\mathrm{kg/m^3}$. It should be noted that this relation also follows from Bernoulli's equation for incompressible flow.

Ground speed (GS) is defined as the actual speed of the aircraft relative to the ground [46]. It is TAS adjusted for wind. When the aircraft experiences a tailwind, GS is bigger than TAS. The equation relating GS to TAS is given later, when the equations of motion are derived.

### 5.1.2. Derivation of FPA Expressions

Before elaborating on idle and fixed-FPA descents, it is important to be familiar with the physics behind an aircraft in descent. Several assumptions are made for the derivations of the equations of motion:

- The Earth is spherical and non-rotating.
- The aircraft is rigid and symmetric.
- The forces act in the centre of gravity (point-mass model).
- The thrust vector is parallel to the aerodynamic velocity, i.e. $\alpha_T = 0$.
- The flight path angle (FPA) $\gamma$ is negative for descent and positive for climb.
- The winds considered are steady horizontal winds that depend only on altitude.
- Small angle approximations for $\gamma$ are appropriate.

In Figure 5.1, a general force diagram of an aircraft in descent is shown. The body-fixed reference frame $\mathcal{F}_b$ and the aerodynamic reference frame $\mathcal{F}_a$ are provided. Since no pitch, roll, and yaw are considered in this diagram, the body-fixed reference frame coincides with the normal Earth reference frame $\mathcal{F}_E$. The aircraft weight $W = mg$ acts along the $Z_E$-axis, so in this case also along the $Z_b$-axis. The lift $L$, drag $D$ and true airspeed $V_T$ are all acting in $\mathcal{F}_a$. Since $\alpha_T = 0$ is assumed, the thrust also acts along the $X_a$-axis. The aerodynamic FPA $\gamma_a$ is the angle between the $X_E$- (here also $X_b$-) and $X_a$-axis.

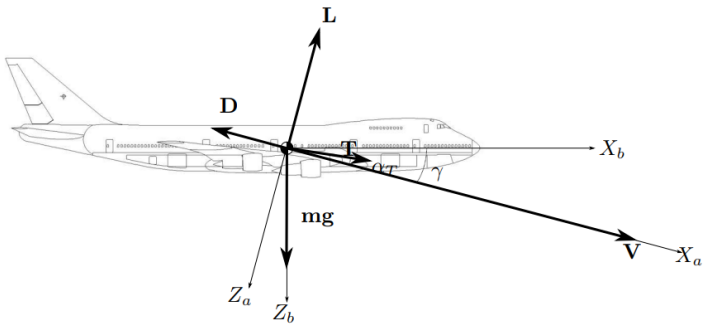


**Figure 5.1:** General force diagram of an aircraft in descent [7].

For descent, the longitudinal equations of motion are important. These are expressed in $\mathcal{F}_a$, both parallel and perpendicular to the flight path. When no wind is considered, these equations are [7]:

$$m\frac{dV_T}{dt} = T - D - mg\sin\gamma_a \tag{5.7}$$

$$mV_T\frac{d\gamma_a}{dt} = L - mg\cos\gamma_a \tag{5.8}$$

In [7], $\gamma$ is assumed to be positive downwards. Therefore, the equations above are not exactly the equations found in [7]. When a steady horizontal wind is considered, extra terms taking into account the wind dependency on altitude are added to the equations, so these then become [47]:

$$m\frac{dV_T}{dt} = T - D - mg\sin\gamma_a - mV_T\frac{dV_w}{dh}\sin\gamma_a\cos\gamma_a \tag{5.9}$$

$$mV_T\frac{d\gamma_a}{dt} = L - mg\cos\gamma_a + mV_T\frac{dV_w}{dh}\sin^2\gamma_a \tag{5.10}$$

Here, $V_w$ is the horizontal wind velocity in the longitudinal direction. Since the equations are the longitudinal equations of motion, lateral wind is not considered. The true airspeed $V_T$, the wind speed $V_w$ and the ground speed $V_{GS}$ are related as follows:

$$\vec{V_{GS}} = \vec{V_T} + \vec{V_w} \tag{5.11}$$

In scalar form, longitudinally, $V_w$ is positive for a tailwind and negative for a headwind.

The objective is to derive an expression for the geometric FPA $\gamma_g$, based on the equations of motion. Using small angle approximations, $\gamma_a$ and $\gamma_g$ are linked as follows [4]:

$$\begin{aligned}
\gamma_a &= \arcsin\frac{\frac{dh}{dt}}{V_T} \approx \frac{\frac{dh}{dt}}{V_T} \\
\gamma_g &= \arcsin\frac{\frac{dh}{dt}}{V_{GS}} \approx \frac{\frac{dh}{dt}}{V_{GS}} \\
\Rightarrow\quad & \gamma_a V_T = \gamma_g V_{GS} \\
\Rightarrow\quad & \gamma_a = \gamma_g\left(\frac{V_T + V_w}{V_T}\right) = \gamma_g\left(1 + \frac{V_w}{V_T}\right)
\end{aligned} \tag{5.12}$$

Rewriting Equation 5.9 using small angle approximations ($\sin\gamma_a \approx \gamma_a$ and $\cos\gamma_a \approx 1$) and substituting $\frac{dV_T}{dt} = \frac{dV_T}{dh}\frac{dh}{dt}$, as well as $\frac{dh}{dt} = \gamma_a V_T$ as defined in Equation 5.12 gives:

$$\gamma_a = \frac{T - D}{mg + mV_T\left(\frac{dV_w}{d_h} + \frac{dV_T}{dh}\right)} \tag{5.13}$$

An expression for $\gamma_g$ is obtained by substituting the final expression of Equation 5.12 for $\gamma_a$ into Equation 5.13 and rearranging:

$$\gamma_g = \frac{T - D}{\left(1 + \frac{V_w}{V_T}\right)\left[mg + mV_T\left(\frac{dV_w}{d_h} + \frac{dV_T}{dh}\right)\right]} \tag{5.14}$$

From Equation 5.14, the thrust required to stay on the desired $\gamma_g$ in known conditions can be calculated directly.

In [7], another equation useful for idle descent is derived. In Equation 5.15, the maximum FPA for which the aircraft will glide without accelerating in IAS is given. It must be noted that this derivation assumes no wind. In addition, here $\gamma$ is defined as positive downwards, which is different from the equations above. Furthermore, it assumes that Calibrated Airspeed (CAS) is equal to Equivalent Airspeed (EAS). Furthermore, instrument errors are neglected, meaning that it is assumed CAS is equal to IAS. This assumption is valid, as the difference between the two is generally small. Even though the expression is expressed in terms of EAS and strictly speaking determines the maximum FPA for gliding without accelerating in EAS, it is used in [7] as if EAS is equal to IAS, as stated above. To make the equation useful for high subsonic speeds and altitudes, the desired IAS should be converted to EAS properly before using the

value in the equation. The conversion from IAS to EAS is explained in section 5.1.1. In reality, IAS might accelerate slightly when EAS is constant, but this acceleration is assumed to be small. So the equation is a reasonable approximation for the maximum FPA without acceleration in IAS. For an idle descent, the thrust $T$ must be set to $T_{idle}$.

The equation for the maximum FPA for which the aircraft will glide without accelerating in EAS is [7]:

$$\gamma_{max} = \arcsin\left(\frac{-\sqrt{\frac{\rho}{\rho_0}}g\left(\frac{T-D}{W}\right)}{\sqrt{\frac{\rho}{\rho_0}}g + \left(\frac{g_0}{R\lambda}+1\right)\left(1+\frac{H\lambda}{T_0}\right)^{-\left(\frac{g_0}{R\lambda}+2\right)} V_{EAS}^2 \left(\frac{\rho_0}{\rho}\right)^{\frac{3}{2}} \frac{\lambda}{2T_0}}\right) \tag{5.15}$$

The derivation of this equation starts with the time derivative of the relationship between TAS and EAS and used the ISA relations to express the time derivative of air density. In addition, the longitudinal equation of motion without wind parallel to the flight path is used. Lastly, it should be noted that here, $\gamma$ is the aerodynamic FPA $\gamma_a$. However, without wind, $\gamma_a = \gamma_g$, as can be seen from Equation 5.12 with $V_w = 0$. The derivation becomes considerably more complex when wind is considered. However, the maximum FPA obtained from Equation 5.15 should be viewed as an indication for situations involving wind.

## 5.2. Idle Descents

This section presents an overview of the research done on idle descents as found in literature. Since idle descents are central in this thesis research, a thorough understanding of this is of high importance. In an idle descent, the throttle is set to the idle position. This is the lowest power setting possible without shutting down the engines. A small amount of thrust is still produced. During the idle descent, a constant Mach is maintained until the crossover altitude. From this point onward, a constant calibrated airspeed (CAS) is maintained. This is stopped only at a speed change point, such as the IAF, or when ATC instructs a new speed. In Figure 5.2, a schematic overview of the vertical profile of an idle descent is provided. It shows that constant Mach and later constant CAS are maintained until deceleration is required to adhere to the speed constraint at the IAF.

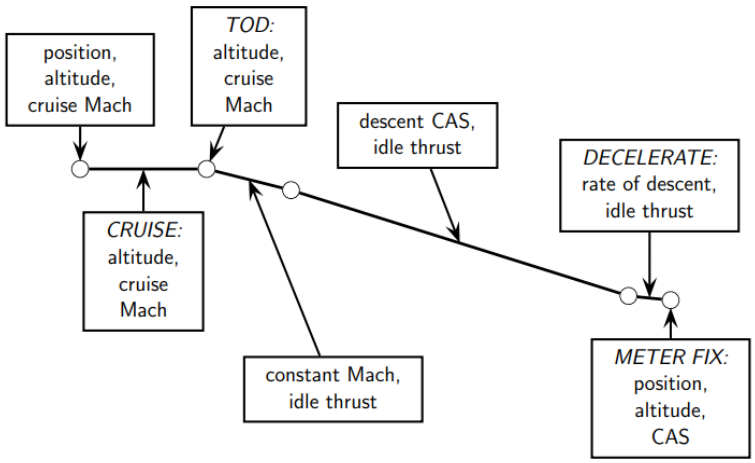


**Figure 5.2:** Schematic overview of an idle descent [48].

The idle descent is very efficient in terms of fuel usage, noise, and emissions, but it comes with increased uncertainty, thereby requiring larger spacing [4]. The vertical profile of an idle descent is highly sensitive to the descent speed profile, wind, and aircraft weight. The descent path becomes shallower with a decrease in descent speed, an increase in tailwind, or an increase in aircraft weight. Typically, large separation buffers are applied by ATC to ensure sufficient distance from an aircraft performing an idle descent. Due to the rapidly increasing uncertainty in an idle descent, level segments are often imposed by ATC to reduce the vertical uncertainty back to zero.

When examining historical flight data, it is not always straightforward to determine whether an idle descent was actually flown. In [49], a method to identify an idle descent with is given. The target Mach before the crossover altitude and the target CAS after the crossover altitude until the IAF are derived from the flight-specific Cost Index (CI). The CI is calculated such that minimum trip cost is achieved, using a trade-off between operating costs and incremental fuel burn. For a selected CI, the FMS manages the corresponding idle-thrust descent path. An idle descent can be identified easily when data on the thrust or fuel burn is available. Unfortunately, this information is usually only available on the aircraft, and is not downlinked to the ground. Therefore, Air Navigation Service Providers (ANSPs) have no insight into these parameters. Instead, [49] shows that an idle descent can be identified by comparing the actual speed profile to a typical Mach/CAS target speed profile. A benefit is that the actual flown speed is not important. Since idle descents are executed on a constant Mach/CAS speed profile, the only analysis required is whether the speed profile is constant. This makes the method robust for varying CI values between different flights. Logically, this method does not give insight in whether the preferred CI was adhered to during the descent. Important to note is that for this method, it is assumed that above the crossover altitude, CAS increases linearly with decreasing altitude for a constant Mach. Below the crossover altitude, CAS is constant. This creates a regression problem with two segments. This model is used to determine the Root Mean Square Deviation (RMSD) with the available airspeed data. The descent is found to be an idle descent when the RMSD and the absolute maximum deviation are below a predefined threshold. In reality, it is possible to fly a constant Mach/CAS speed profile without flying an idle descent. For example, a fixed-FPA descent discussed later can be flown with a constant Mach/CAS speed profile. Therefore, this method is not entirely robust for identifying idle descents.

The shape of the descent path determines the TOD. This is the location where the descent is initiated. Naturally, steeper descents require a TOD closer to the IAF than shallower descents. In [48], the TOD location is estimated as a linear function of several predictive factors, including aircraft type, aircraft weight, wind, cruise altitude and Mach, descent CAS, and IAF constraints. Multiple regression was used for this estimation. Flight and radar data of many flights were used to extract the flown flight paths and the values of the predictive factors. It was found that the quality of the regression fit improves with more accurate data on the predictive factors, especially on wind, speed, and altitude. Furthermore, the accuracy of predicted TOD location was within $5$ nm. Since this approach uses historical flight data to find regressions for specific aircraft types, many models are needed for this to be useful in a high-density traffic scenario. The approach could be used to derive relations between the mentioned predictive factors and the TOD locations when simulating aircraft trajectories with uncertainty using the models described in chapter 4.

In 2006, a trial was conducted in which aircraft flew CDAs from cruise until the final approach at Schiphol Airport (EHAM) during nighttime operations [15]. An idle descent path was flown to the first vertical constraint. This constraint was beyond the TMA boundary and thus beyond the IAF. The test was conducted in low traffic densities only, to ensure safe circumstances and sufficient spacing. Optimal CDAs flown during the trial used minimal altitude stabilisation, minimal thrust increase from idle, and no excessive use of speed brakes. The findings of this test support the statement in section 4.2 that accurate wind information should improve trajectory predictability and thus reduce trajectory uncertainty. Therefore, nighttime CDAs should include uplinking weather forecasts prior to TOD. Most aircraft have the ability to receive automated uplinks. Since this research involves a 24-hour operation, the uplinks would also be required during the day.

Currently, CDAs are still only flown during nighttime operations at Schiphol Airport, mainly due to the need for an increased landing interval [7]. Many types of CDA have been designed and elaborated on in [7], but these are focused on the approach from the IAF to the FAF (Final Approach Fix), where the ILS is intercepted. However, the newly proposed CDA type in this paper can potentially be used in the earlier descent segment from the cruise TOD to IAF as well. This CDA type uses variable FPA. Furthermore, the aircraft flies at $250$ KIAS on autothrottle until a thrust-cutback point is reached, at which point the throttle is set to the idle position. Thrust is reapplied only when the approach speed is reached. The approach was flown with two segments of different constant FPA, using idle thrust as much as possible. With this variation in FPA, the ETA could be adapted such that the RTA was met as close as possible.

Another CDO concept, planning a full idle descent from cruise TOD till the stabilisation point at $1000$ ft above ground, is named Time and Energy Managed Operations (TEMO) [50]. The algorithm uses the law of conservation of energy to exchange kinetic and potential energy, to correct for deviations without using thrust or speed brakes, thereby keeping the total energy constant. In practice, altitude is exchanged for

speed and vice versa. A trajectory consists of a nominal airspeed profile. As stated earlier, a constant Mach is flown until the crossover altitude. From here onwards, a constant CAS is flown until a rapid deceleration to the IAF speed constraint is required. It can be assumed that CAS increases linearly with a decreasing altitude for a constant Mach. Speed-on-elevator (SOE) control is used to fly the speed profile. As the name suggests, only the elevator is used to control the aircraft speed. Thrust was set to idle, and speed brakes were omitted. When large deviations are detected, the algorithm minimises the use of thrust and speed brakes to return to the nominal trajectory. By using a tactical speed controller, the effects of wind estimation errors were effectively minimised. This is the case because a tactical controller corrects for deviations immediately, using a closed-loop control system.

## 5.3. Fixed-FPA Descents

This section presents an overview of the research done on fixed-FPA descents as found in the literature. Since the fixed-FPA descent is an important factor in this thesis research, a thorough understanding of this is required. In a fixed-FPA descent, the aircraft follows a predefined, constant geometric FPA ($\gamma_g$). A great advantage of this descent type is that the vertical profile of the aircraft is explicitly defined. Because of this, fixed-FPA descents have an increased predictability and thus decreased uncertainty compared to idle descents [4], [5]. Therefore, fixed-FPA descents are more suitable in higher traffic densities. However, in order to adhere to the fixed $\gamma_g$, non-idle thrust is required. Instead of a constant $\gamma_g$ throughout the entire descent, the descent can be split into segments. In each segment, a different $\gamma_g$ can be used. Using this can make a descent more efficient, as the optimal $\gamma_g$ varies with altitude.

Another option would be to follow a predefined, constant aerodynamic FPA ($\gamma_a$). Due to varying wind conditions, this would result in various $\gamma_g$ being achieved throughout the descent. With this, predictability is decreased and uncertainty is increased, as the optimal $\gamma_a$ is different between aircraft types and weights.

In a fixed-FPA descent, a constant CAS is maintained for each segment, similar to an idle descent. Also, a deceleration segment before the IAF is introduced to adhere to the speed restrictions there [4], [5]. The thrust required is calculated based on the predefined $\gamma_g$ and CAS, and on the other aircraft- and weather-specific variables. In Figure 5.3, a schematic overview of a fixed-FPA descent is provided.

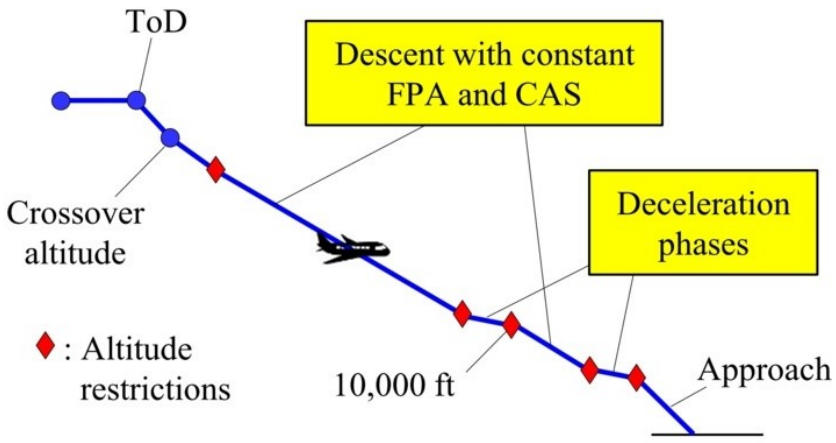


**Figure 5.3:** Schematic overview of a fixed-FPA descent (adjusted from [51]).

Various aircraft types contain an autopilot mode through which a fixed-FPA descent can be flown [7]. This FPA mode can be selected via the Mode Control Panel (MCP). The pilot can select the desired $\gamma_g$ using a knob on the MCP. The autopilot controls the aircraft along this $\gamma_g$, independent of wind conditions. This FPA mode is available on the A320, A330, A340, and A380 Airbus types. For Boeing aircraft, this mode has been introduced on the B777, B787, and B747-800. Even though the fixed-FPA descent profile is independent of wind conditions, accurate wind information is still important to determine ground speed and subsequently arrival time at waypoints. Because of this, consistency between wind information available on the ground and wind information loaded into the FMS is desired [5]. Generally, if no specific FPA mode is available, a fixed-FPA descent is flown in the VNAV PATH autopilot mode [52]. While the autopilot guides

the aircraft, pilots only monitor the vertical profile to make sure the aircraft is following the path along the predefined FPA. Pilots may use speed brakes when instructed, in case the aircraft tends to deviate from the desired path, to correct the VNAV PATH mode. Another possibility for flying a fixed-FPA descent, is to have the pilot manually create a waypoint after the TOD, and input an altitude for all necessary waypoints along the route in the FMC [52], [53]. By adhering to the input altitudes, the desired FPA is flown.

One of the first flight tests demonstrating a fixed-FPA descent, was in 2002, at Louisville International Airport [17]. During this test, fixed-FPA descents were flown inside the TMA. Even though the descent segment from cruise TOD until IAF is of interest, the flight test inside the TMA provides useful insights. The test confirmed noise reduction and fuel saving compared to a conventional step-down approach. In addition, it was confirmed that accurate trajectory predictions are needed when this descent is to be implemented in high-density traffic, as it requires a different spacing strategy from ATC. In [53], the importance of accurate wind estimations to achieve more accurate time-spacing is underlined.

In recent years, flight tests and simulator tests have been conducted in various research projects. Full-flight simulator trials and field tests at Moses Lake Grant County International Airport, under Boeing's ecoDemonstrator 2018 program, have shown that the fixed-FPA descent trajectory can be predicted with great accuracy [52]. Furthermore, simulator trials in full-flight B777-200 and B787-800 simulators, with descents to Kansai International Airport and Tokyo International Airport, have demonstrated that the fixed-FPA descent is feasible for wide-body aircraft using the current FMS and pilot intervention [51], [53], [54]. The descent is operationally feasible for FPA under $2.5°$, and acceptable in operations in terms of tracking performance. The fixed-FPA descent therefore has the capabilities required for procedure integration into congested airspace. The vertical path can be predicted by ATC, and the arrival time is controllable. Because of this, the combination of a fixed-FPA descent with speed control has the potential to result in significant improvements in fuel and time management efficiency in future operations, compared to conventional arrival operations.

Various studies have investigated the fuel usage of a fixed-FPA descent and compared it to other descent types. In [55], real flight data of conventional descents were compared to simulated fixed-FPA descents of $3°$. This showed that the $3°$ fixed-FPA descent generally has considerably less fuel usage and increased time saving. The most optimal FPA for the highest fuel saving relative to $1°$ is investigated in [56], for five similar aircraft types (B737, B738, A319, A320, and A321). Here, real flight data of flights containing constant FPA descent segments of at least $200\,$s were used to investigate the fuel usage during these fixed-FPA segments. The results suggest a U-shaped pattern for total fuel burn with an increase in the FPA. The highest fuel saving relative to a $1°$-FPA was found to be 14.0% (191 kg) for an FPA of $2.5°$. This result is convenient, as [54] has shown the fixed-FPA descent is operationally feasible for FPA under $2.5°$ for wide-body aircraft, as stated earlier.

While idle-thrust descents are generally seen as fuel-optimal descents, it has been shown that an idle descent does not necessarily result in the most fuel-optimal trajectory [57]. Monte Carlo simulations were performed to compare fixed-FPA descents to idle descents. It was found that the fixed-FPA descent divided into multiple segments, with each unique FPAs, is the most fuel-efficient fixed-FPA descent. However, this descent requires explicit communication between the pilot and ATC regarding FPA intent prior to the TOD. The fixed-FPA descent with constant FPA throughout the entire descent was found to be more sensitive to speed brake conditions, which reduces the efficiency. The comparison to idle descents showed that, on average of the test conditions sampled, idle-thrust descents burned $41\,$lbs ($\approx 18.6\,$kg) more fuel than the fuel-optimal fixed-FPA descents. The reason for this is that in some situations, fuel can be saved by having the TOD for the fixed-FPA earlier than the TOD of an idle descent. The reduced fuel burn in the cruise segment is then greater than the extra fuel burn in the descent segment.

In December 2022 and February 2023, for the first time ever, the fixed-FPA descent was demonstrated on scheduled commercial flights to Kansai International Airport [6]. The aircraft types used were the A320neo and A320ceo aircraft. The aim of this demonstration was to expand the time frame for possible implementation of CDO in Japan. The Profile Descent (PD) is the most fuel-efficient descent as it is optimised by the FMS for the specific aircraft. However, trajectory predictability is lower due to the uncertainties from specific aircraft performance and weather conditions. Due to the low trajectory predictability of PD, its implementation in Japan is currently limited to three airports, one of which is Kansai International Airport. Here, PDs can be performed on flights with scheduled arrival times between 23:00 and 07:00 JST (Japan Standard Time). By taking advantage of the fact that the fixed-FPA descent has higher vertical

trajectory predictability than PD and thus facilitates ATC operations, the CDO implementation window can be extended by allowing fixed-FPA descents outside the current CDO hours. The flight test showed that, compared to conventional step-down descents, the reduction in fuel consumption for the $2.5°$-FPA descent was 9%, while it was 6.7% for the $2.0°$-FPA descent. From flight simulator tests using the PD under conditions similar to those in the demonstration flights, a 6.2% reduction in fuel consumption was observed. This indicates that the PD and the fixed-FPA descent achieve nearly the same fuel consumption reduction. Furthermore, [51] demonstrated that the fixed-FPA descent could potentially reduce the fuel consumption in congested airspace compared to the PD. This is the case especially when arrival time delays of more than approximately $120$ s are present.

## 5.4. Knowledge Gap

In the chapters and sections above, a detailed overview is provided of the research conducted regarding trajectory uncertainties, CDOs, and particularly idle and fixed-FPA descents. In this section, the knowledge gap, linking the previous research found in the literature to the research topic of this thesis, is formulated clearly.

Currently, CDOs are restricted to low traffic densities due to the high unpredictability [6]. Also at Schiphol, it is restricted to only nighttime operations [7]. Potential lies in investigating when idle and fixed-FPA descents can be flown throughout a 24-hour operation, as this information is currently unavailable. The feasibility of flying idle and fixed-FPA descents has been demonstrated [6], [15], [48], [51], [53], [54]. However, no clear criteria have been developed for when these descents can be executed safely in the presence of other traffic. Using accurate trajectory uncertainty modelling to determine criteria for the execution of these descents is novel. Therefore, this research will focus on developing criteria for the execution of idle and fixed-FPA descents, taking into account the associated trajectory uncertainties. Executing idle and fixed-FPA descents in higher traffic densities enables the possibility of further reducing noise, emissions, and fuel burn.

# References


[1] SESAR Joint Undertaking, *European ATM Master Plan, 2025 Edition*, https://www.sesarju.eu/MasterPlan2025_SupportingDocuments, Accessed: 22-04-2025.

[2] M. Tielrooij, R. Kok, T. de Jong, F. Dijkstra, T. Dufourmont, E. Lap, A. Okina, and R. Vos, "Transition to Trajectory Based Operations (TBO)," *KDC/2021/0062*, 2022.

[3] ICAO, *Continuous Descent Operations (CDO) Manual (Doc 9931)*, International Civil Aviation Organization, Montreal, Quebec, Canada, 2010.

[4] P. Pradeep and P. Wei, "Predictability, Variability and Operational Feasibility Aspect of CDA," in *2017 IEEE Aerospace Conference*, 2017, pp. 1–14. DOI: 10.1109/AERO.2017.7943728.

[5] K.-O. Tong, E. G. Schoemig, D. A. Boyle, J. Scharl, and A. Haraldsdottir, "Descent Profile Options for Continuous Descent Arrival Procedures within 3D Path Concept," in *2007 IEEE/AIAA 26th Digital Avionics Systems Conference*, 2007, 3.A.3-1-3.A.3–11. DOI: 10.1109/DASC.2007.4391872.

[6] D. Iwata, Y. Nonaka, Y. Funai, T. Shindo, S. Tanaka, M. Sato, and E. Itoh, "Demonstration of Fixed Flight-Path Angle Descent via Scheduled Commercial Flights," *Journal of Air Transportation*, pp. 1–16, 2024. DOI: 10.2514/1.d0400.

[7] R. Sopjes, P. d. Jong, C. Borst, M. M. v. Paassen, and M. Mulder, "Continuous Descent Approaches with Variable Flight-Path Angles under Time Constraints," *AIAA Guidance, Navigation, and Control Conference*, 2011. DOI: 10.2514/6.2011-6219.

[8] J. Hoekstra and J. Ellerbroek, *AE4321-15 Air Traffic Management: Lecture Slides ATS & Airspaces*, https://brightspace.tudelft.nl/d2l/le/content/593465/viewContent/3328509/View, Accessed: 22-04-2025.

[9] EUROCONTROL, *LSSIP 2018 THE NETHERLANDS, Local Single Sky Implementation, Level 1 - Implementation Overview*, https://www.eurocontrol.int/sites/default/files/2019-06/lssip2018_netherlands_release.pdf, Accessed: 22-04-2025.

[10] Ministry of Infrastructure & Water Management and Ministry of Defence, *Startnota Luchtruimvisie*, https://zoek.officielebekendmakingen.nl/blg-107129.pdf, Accessed: 22-04-2025.

[11] LVNL, *Integrated Aeronautical Information Package (eAIP): EHAM Standard Arrival Chart*, https://eaip.lvnl.nl/web/2025-04-03-AIRAC/html/index-en-GB.html, Accessed: 22-04-2025.

[12] M. Sergeeva, D. Delahaye, C. Mancel, and A. Vidosavljevic, "Dynamic airspace configuration by genetic algorithm," *Journal of Traffic and Transportation Engineering (English Edition)*, vol. 4, no. 3, pp. 300–314, 2017. DOI: https://doi.org/10.1016/j.jtte.2017.05.002. [Online]. Available: https://www.sciencedirect.com/science/article/pii/S2095756417301927.

[13] A. Warren, "Trajectory Prediction Concepts for Next Generation Air Traffic Management," in *3rd USA/Europe ATM R&D Seminar*, Citeseer, 2000, p. 171.

[14] ICAO, *Performance-based Navigation (PBN) Manual (Third Edition)*, https://www.icao.int/sam/documents/2009/samig3/pbn%20manual%20-%20doc%209613%20final%205%2010%2008%20with%20bookmarks1.pdf, Accessed: 22-04-2025.

[15] J. Wat, J. Follet, R. Mead, J. Brown, R. Kok, F. Dijkstra, and J. Vermeij, "In Service Demonstration of Advanced Arrival Techniques at Schiphol Airport," *6th AIAA Aviation Technology, Integration and Operations Conference (ATIO)*, 2006. DOI: 10.2514/6.2006-7753.

[16] F. Wubben and J. Busink, "Environmental benefits of continuous descent approaches at Schiphol Airport compared with conventional approach procedures," *NLR-TP-2000-275*, 2000.

[17] J.-P. Clarke, J. Brown, K. Elmer, N. Ho, L. Ren, K.-O. Tong, and J. Wat, “Continuous Descent Approach: Design and Flight Test for Louisville International Airport,” *Journal of Aircraft*, vol. 41, pp. 1054–1066, 2004. DOI: 10.2514/1.5572.

[18] S. Mondoloni, S. Swierstra, and M. Paglione, “Assessing Trajectory Prediction Performance - Metrics Definition,” in *24th Digital Avionics Systems Conference*, vol. 1, 2005, pp. 3.C.1–31. DOI: 10.1109/DASC.2005.1563347.

[19] P. Weitz, “Determination and Visualization of Uncertainties in 4D-Trajectory Prediction,” in *2013 Integrated Communications, Navigation and Surveillance Conference (ICNS)*, 2013, pp. 1–9. DOI: 10.1109/ICNSurv.2013.6548525.

[20] S. Torres, “Trajectory Accuracy Sensitivity to Modeling Factors,” *15th AIAA Aviation Technology, Integration, and Operations Conference*, 2015. DOI: 10.2514/6.2015-2599.

[21] E. J. Casado Magaña, “Trajectory prediction uncertainty modelling for Air Traffic Management,” Ph.D. dissertation, University of Glasgow, 2016.

[22] S. Mondoloni and I. Bayraktutar, “Impact of Factors, Conditions and Metrics on Trajectory Prediction Accuracy,” *Proceedings of the 6th USA/Europe Air Traffic Management Research and Development Seminar, ATM 2005*, pp. 305–314, 2005.

[23] S. Sankararaman and M. Daigle, “Uncertainty Quantification in Trajectory Prediction for Aircraft Operations,” *AIAA Guidance, Navigation, and Control Conference*, 2017. DOI: 10.2514/6.2017-1724.

[24] J. Bronsvoort, G. McDonald, R. Potts, and E. Gutt, “Enhanced Descent Wind Forecast for Aircraft,” *Proceedings of the Ninth USA/Europe Air Traffic Management Research and Development Seminar (ATM2011)*, 2011.

[25] ICAO, *TBO Concept: version Appendix A to WP-652 - TBOCD 3.0*, https://www.sesarju.eu/sites/default/files/documents/reports/Appendix_A_to_WP652_TBOCD_3.0.pdf, Accessed: 01-04-2025.

[26] J. V. Martinez, *Network 4D Trajectory CONOPS*, https://www.eurocontrol.int/sites/default/files/2023-09/eurocontrol-network-4dt-conops-v1-0.pdf, Accessed: 01-04-2025.

[27] M. Prandini, J. Hu, J. Lygeros, and S. Sastry, “A Probabilistic Approach to Aircraft Conflict Detection,” *IEEE Transactions on intelligent transportation systems*, vol. 1, no. 4, pp. 199–220, 2000. DOI: 10.1109/6979.898224.

[28] L. C. Yang and J. K. Kuchar, “Using Intent Information in Probabilistic Conflict Analysis,” *Guidance, Navigation, and Control Conference and Exhibit*, pp. 797–806, 1998. DOI: 10.2514/6.1998-4237.

[29] A. Lecchini Visintini, W. Glover, J. Lygeros, and J. Maciejowski, “Monte Carlo Optimization for Conflict Resolution in Air Traffic Control,” *IEEE Transactions on Intelligent Transportation Systems*, vol. 7, no. 4, pp. 470–482, 2006. DOI: 10.1109/TITS.2006.883108.

[30] E. Casado, M. L. Civita, M. Vilaplana, and E. W. McGookin, “Quantification of Aircraft Trajectory Prediction Uncertainty Using Polynomial Chaos Expansions,” in *2017 IEEE/AIAA 36th Digital Avionics Systems Conference (DASC)*, 2017, pp. 1–11. DOI: 10.1109/DASC.2017.8102052.

[31] Y. Matsuno and T. Tsuchiya, “Probabilistic Conflict Detection in the Presence of Uncertainty,” *2014, Lecture Notes in Electrical Engineering Air Traffic Management and Systems*, pp. 17–33, 2014. DOI: 10.1007/978-4-431-54475-3_2.

[32] Y. Wang, Y. Pang, O. Chen, H. N. Iyer, P. Dutta, P. Menon, and Y. Liu, “Uncertainty quantification and reduction in aircraft trajectory prediction using Bayesian-Entropy information fusion,” *Reliability Engineering & System Safety*, vol. 212, p. 107 650, 2021. DOI: 10.1016/j.ress.2021.107650.

[33] A. Lee, S. Weygandt, B. E. Schwartz, and J. R. Murphy, “Performance of Trajectory Models with Wind Uncertainty,” *AIAA Modeling and Simulation Technologies Conference*, 2009. DOI: 10.2514/6.2009-5834.

[34] Q. Zheng and Y. Zhao, “Modeling Wind Uncertainties for Stochastic Trajectory Synthesis,” *11th AIAA Aviation Technology, Integration, and Operations (ATIO) Conference*, 2011. DOI: 10.2514/6.2011-6858.

[35] E. Hernández-Romero, A. Valenzuela, and D. Rivas, “Probabilistic multi-aircraft conflict detection and resolution considering wind forecast uncertainty,” *Aerospace Science and Technology*, vol. 105, p. 105 973, 2020. DOI: 10.1016/j.ast.2020.105973.

[36] B. Schwartz, S. Benjamin, S. Green, and M. Jardin, “Accuracy of RUC-1 and RUC-2 Wind and Aircraft Trajectory Forecasts by Comparison with ACARS Observations,” *Weather and Forecasting*, vol. 15, pp. 313–326, 2000. DOI: 10.1175/1520-0434(2000)015<0313:AORARW>2.0.CO;2.

[37] G. Chaloulos and J. Lygeros, “Effect of Wind Correlation on Aircraft Conflict Probability,” *Journal of Guidance, Control, and Dynamics*, vol. 30, no. 6, pp. 1742–1752, 2007. DOI: 10.2514/1.28858.

[38] S. Seyedipour, H. Nobahari, and M. Prandini, “A probabilistic approach to mid-term conflict detection with accuracy estimate,” *Journal of the Franklin Institute*, vol. 359, no. 16, pp. 9193–9219, 2022. DOI: 10.1016/j.jfranklin.2022.08.055.

[39] J. Hu, M. Prandini, and S. Sastry, “Aircraft Conflict Prediction in the Presence of a Spatially Correlated Wind Field,” *IEEE Transactions on Intelligent Transportation Systems*, vol. 6, no. 3, pp. 326–340, 2005. DOI: 10.1109/TITS.2005.853699.

[40] J. Hu, M. Prandini, and S. Sastry, “Aircraft Conflict Detection in Presence of Spatially Correlated Wind Perturbations,” *AIAA Guidance, Navigation, and Control Conference and Exhibit*, 2003. DOI: 10.2514/6.2003-5339.

[41] J. M. Hoekstra and J. Ellerbroek, “Aerial Robotics: State-based Conflict Detection and Resolution (Detect and Avoid) in High Traffic Densities and Complexities,” *Current Robotics Reports*, vol. 2, no. 3, pp. 297–307, 2021. DOI: 10.1007/s43154-021-00061-6.

[42] G. Li, S. Zhai, and Q. Jia, “Conflict Detection and Resolution Based on Four-Dimensional Trajectory,” in *Civil Airliner Flight Guidance Technology for Four-Dimensional Trajectory-Based Operation*. Springer Nature Singapore, 2024, pp. 149–188. DOI: 10.1007/978-981-97-5300-0_6.

[43] EUROCONTROL, *Automatic Dependent Surveillance Contract (ATS-B2)*, https://www.eurocontrol.int/service/automatic-dependent-surveillance-contract-ats-b2, Accessed: 02-04-2025.

[44] J. Bronsvoort, G. McDonald, S. Torres, M. Paglione, C. Young, J. Hochwarth, J. Boucquey, and M. Vilaplana, “Use of the Extended Projected Profile (EPP) in Trajectory Management,” in *16th American Institute of Aeronautics and Astronautics (AIAA) Aviation Technology, Integration, and Operations Conference*, 2016.

[45] J. John D. Anderson, *Fundamentals of Aerodynamics*, 6th ed. New York: McGraw-Hill Education, 2017.

[46] Federal Aviation Administration, “Flight Instruments,” in *Pilot’s Handbook of Aeronautical Knowledge*. Washington, D.C.: U.S. Department of Transportation, Federal Aviation Administration, 2023, ch. 8. [Online]. Available: https://www.faa.gov/sites/faa.gov/files/regulations_policies/handbooks_manuals/aviation/phak/10_phak_ch8.pdf.

[47] D. Rivas, A. Valenzuela, and J. L. de Augusto, “Computation of global trajectories of commercial transport aircraft,” *Proceedings of the Institution of Mechanical Engineers, Part G*, vol. 227, no. 1, pp. 142–158, 2013. DOI: 10.1177/0954410011427107.

[48] L. Stell, “Predictability of Top of Descent Location for Operational Idle-Thrust Descents,” *10th AIAA Aviation Technology, Integration, and Operations (ATIO) Conference*, 2010. DOI: 10.2514/6.2010-9116.

[49] J. Bronsvoort, T. Huynh, and G. Enea, “An Operator-Focussed Metric for Measuring Predictability and Efficiency of Descent Operations,” *16th AIAA Aviation Technology, Integration, and Operations Conference*, 2016. DOI: 10.2514/6.2016-4219.

[50] P. M. A. de Jong, N. de Gelder, R. P. M. Verhoeven, F. J. L. Bussink, R. Kohrs, M. M. van Paassen, and M. Mulder, “Time and Energy Management During Descent and Approach: Batch Simulation Study,” *Journal of Aircraft*, vol. 52, no. 1, pp. 190–203, 2015. DOI: 10.2514/1.c032668.

[51] D. Toratani, N. K. Wickramasinghe, J. Westphal, and T. Feuerle, “Feasibility study on applying continuous descent operations in congested airspace with speed control functionality: Fixed flight-path angle descent,” *Aerospace Science and Technology*, vol. 107, p. 106 236, 2020. DOI: 10.1016/j.ast.2020.106236.

[52] N. K. Wickramasinghe, D. Toratani, E. Itoh, J. Westphal, H. Schoniger, T. Feuerle, and M. Stanisak, “Experimental Approach for Efficient Arrival Procedures with Fixed-Flight Path Angle Descent,” in *2019 Integrated Communications, Navigation and Surveillance Conference (ICNS)*, 2019, pp. 1–14. DOI: 10.1109/ICNSURV.2019.8735118.

[53] E. Itoh, N. K. Wickramasinghe, H. Hirabayashi, K. Uejima, and S. Fukushima, “Analyzing Feasibility of Continuous Descent Operation Following Fixed-Flight Path Angle from Oceanic Route to Tokyo International Airport,” *AIAA Modeling and Simulation Technologies Conference*, 2016. DOI: 10.2514/6.2016-0168.

[54] E. Itoh, N. K. Wickramasinghe, H. Hirabayashi, and S. Fukushima, “Feasibility study on fixed flight-path angle descent for wide-body passenger aircraft,” *CEAS Aeronautical Journal*, vol. 10, no. 2, pp. 589–612, 2018. DOI: 10.1007/s13272-018-0337-9.

[55] H. Aksoy, E. T. Turgut, and Ö. Usanmaz, “The design and analysis of optimal descent profiles using real flight data,” *Transportation Research Part D: Transport and Environment*, vol. 100, p. 103 028, 2021. DOI: 10.1016/j.trd.2021.103028.

[56] E. T. Turgut, O. Usanmaz, M. Cavcar, T. Dogeroglu, and K. Armutlu, “Effects of Descent Flight-Path Angle on Fuel Consumption of Commercial Aircraft,” *Journal of Aircraft*, vol. 56, no. 1, pp. 313–323, 2019. DOI: 10.2514/1.c033911.

[57] M. G. Wu and M. Green, “Analysis of Fixed Flight Path Angle Descents for the Efficient Descent Advisor,” *NASA/TM–2011–215992*, 2011.